Characterization, Modeling, and Control of Ionic Polymer Transducers

by

Kenneth Newbury

Dissertation submitted to the Faculty of the
Virginia Polytechnic Institute and State University
in partial fulfillment of the requirements for the degree of

Doctor of Philosophy

in

Mechanical Engineering

D. J. Leo, Chair
D. J. Inman
H. H. Robertshaw
A. H. Nayfeh
W. R. Saunders

September 2002
Blacksburg, Virginia

Keywords: Ionic Polymer, Transducer Modeling, Permanent Strain, Ionic Polymer Sensor

Characterization, Modeling, and Control of Ionic Polymer Transducers

Kenneth Newbury, Ph.D.
Virginia Polytechnic Institute and State University, 2002
Advisor: Donald J. Leo

Abstract

Ionic polymers are a recently discovered class of active materials that exhibit bidirectional electromechanical coupling. They are 'soft' transducers that perform best when the mechanical deformation involves bending of the transducer. Ionic polymers are low voltage actuators – they only require inputs on the order of 1V and cannot tolerate voltages above approximately 10V. The mechanisms responsible for the electromechanical coupling are not yet fully understood, and reports of the capabilities and limitations of ionic polymer transducers vary widely. In addition, suitable engineering models have not been developed.

This document presents a dynamic model for ionic polymer transducers that is based on a pair of symmetric, linearly coupled equations with frequency dependent coefficients. The model is presented in the form of an equivalent circuit, employing an ideal transformer with a frequency dependent turns ratio to represent the electromechanical coupling. The circuit elements have clear physical interpretations, and expressions relating them to transducer dimensions and material properties are derived herein.

The material parameters required for the model: modulus, density, electrical properties, and electromechanical coupling term are determined experimentally. The model is then validated by comparing simulated and experimental responses, and the agreement is good. Further validation is presented in the form of extensive experiments that confirm the predicted changes in transducer performance as transducer dimensions are varied. In addition, reciprocity between mechanical and electrical domains is demonstrated. This reciprocity is predicted by the model, and is a direct result of the symmetry in the equations

on which the model is based.

The capabilities of ionic polymer sensors and actuators, when used in the cantilevered bender configuration, are discussed and compared to piezoceramic and piezo polymer cantilevered benders. The energy density of all three actuators are within an order of magnitude of one another, with peak values of approximately 10 J/m^3 and 4mJ/kg for ionic polymer actuators actuated with a 1.2V signal. Ionic polymer sensors compare favorably to piezoelectric sensors. Their charge sensitivity is approximately $320\mu C/m$ for a 0.2 x 5 x 17mm cantilevered bender, two orders of magnitude greater than a piezo polymer sensor with identical dimensions.

This work is concluded with a demonstration of feedback control of a device powered by ionic polymer actuators. An ionic polymer sensor was used to provide the displacement feedback signal. This experiment is the first demonstration of feedback control using an ionic polymer sensor. Compensator design was performed using the model developed in the first chapter of this document, and experiments confirmed that implementation of the control scheme improved, in a narrow frequency range, the system's ability to track sinusoidal inputs.

To my wife,

Ann Marie

Acknowledgments

I would like to thank Dr. Donald Leo, my advisor, for the many productive discussions as well as for providing financial support throughout my graduate studies. Also, I thank the other four members of my advisory committee.

Special thanks are extended to two people, without whom I most likely would not have returned to school. First is Dr. G. Naganathan of the University of Toledo, an exceptionally enthusiastic and caring individual who always goes out of his way to encourage students to explore their potential. I am also immensely grateful to my wife Ann Marie, who, within a year of getting married, agreed to support my return to school as a full time student – a significant departure from our original plans.

This work was supported by the Division of Civil and Mechanical Systems of the National Science Foundation, program director Dr. Alison Flatau. The sample materials used in the experiments described in this work were graciously provided by Dr. Mohsen Shahinpoor at the University of New Mexico and Dr. Kwang Kim at University of Nevada-Reno.

Contents

List of Tables

List of Figures

Chapter 1

Introduction

Ionic polymers are a recently discovered class of active materials that exhibit electromechanical coupling. They can be used as 'soft' transducers and possess a combination of characteristics that several researchers feel makes them well suited to applications not addressed by the growing list of active materials already readily available. Before the engineering community will consider ionic polymers a viable transducer technology, their capabilities and limitations must be well understood and documented. Also, to facilitate the design process, simple but accurate models must be developed. The primary goals of this work are to characterize and model the behavior of ionic polymer transducers at a macroscopic level. A secondary objective is to demonstrate feedback control of a system that employs ionic polymer transducers for both sensing and actuation.

1.1 History

Ionic polymers are a subset of a group of materials known as Electro-Active Polymers (EAPs), polymers that respond to an electrical stimulus. EAP response can take one or more of several forms, such as physical deformation, a change in optical properties, or a change in magnetic properties (Bar-Cohen et al., 2001b). EAPs that response mechanically (exert force, deform, and/or change stiffness) can be subdivided into two categories, electronic EAPs and ionic EAPs, based on the physics believed to be responsible for the EAP response. In electronic EAPs, the coupling is dominated by electrostatic forces. Relative to ionic EAPs, electronic EAPs respond rapidly (milliseconds) and require high fields (on the order of 1MV/m) for actuation. Examples of electronic EAPs are electrostrictive paper, ferroelectric

polymers, and dielectric EAPs. The electromechanical coupling in ionic EAPs involves ion motion and/or chemical reactions. In some ionic EAPs, electrostatic forces are also believed to be significant. The speed of ionic EAPs response varies widely. Some ionic EAPs can take several seconds to respond to an electrical stimulus while others respond in milliseconds. Relative to electronic EAPs, ionic EAPs operate with lower electric fields (on the order of 1kV/m), exert lower forces, but produce higher deflections. Examples of ionic EAPs are carbon nanotubes, conductive polymers, and ionic polymers, the subject of this work.

EAPs are not a recent discovery – reports of experiments using EAPs date back to 1880 (Bar-Cohen et al., 2001b). However, the first reported experiments involving ionic polymer transducers were not published until 1992. These first transducers, as well as those considered in this work, were based on Nafion, a commercial polymer manufactured by DuPont. Oguro et al. (1992) and Segalman et al. (1992) showed that mechanical deformation is produced when an electric field is applied across the thickness of a Nafion based transducer, thus demonstrating an ionic polymer actuator. In the same time period, Sadeghipour et al. (1992) presented experimental test data for a Nafion based accelerometer. They demonstrated that a voltage output could be obtained when a load was applied to a cell in which Pt plated Nafion was sandwiched between two metal plates. Note that earlier experimental results illustrating similar phenomena were published. For example, Grodzinsky and Melcher (1974) demonstrated electromechanical transduction using collagen membranes. They later expanded their work to include other polyelectrolyte membranes, and they experimentally demonstrated both mechanical to electrical and electrical to mechanical transduction (Grodzinsky and Melcher, 1976). However, because of the nature of the base materials and the fact that they were not plated, these early transducer examples are not considered ionic polymer transducers.

1.2 Description

Ionic polymer transducers are fabricated by plating both surfaces of a thin sheet of an ionic polymer such as Nafion, typically with gold or platinum, then cutting a transducer of the desired geometry from the plated sheet. An illustration of a typical ionic polymer transducer cross section is shown in Figure 1.1. The metallic layer acts as a flexible electrode, facilitating the application of an electric field across the ionic polymer's thickness (for actu-

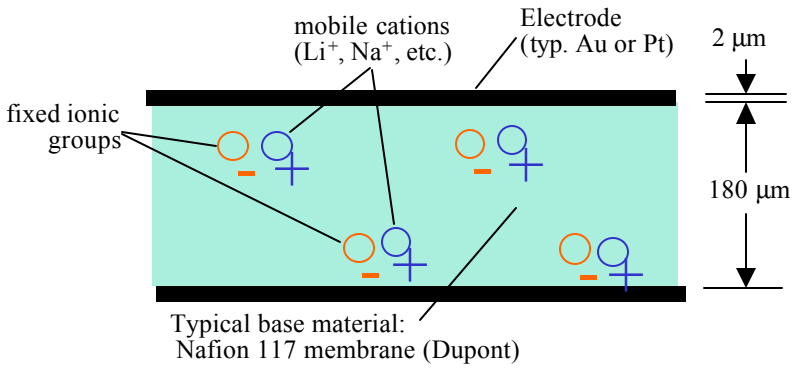

Figure 1.1: Cross section of a typical ionic polymer transducer.

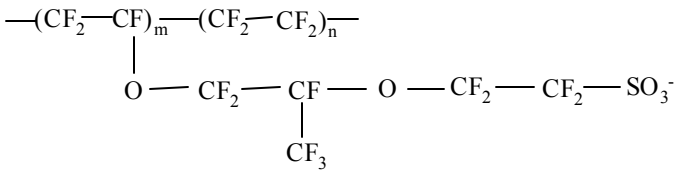

Figure 1.2: Chemical structure of DuPont Nafion

ation) or charge collection (for sensing). An ionic polymer, due to its molecular structure, is permeable exclusively to positively charged ions or to negatively charged ions, depending on the material. DuPont's Nafion, the most common base material for ionic polymer transducers, is permeable to cations (positively charged ions) but not to anions. Because of its ion selectivity, as well as other desirable material properties, Nafion is used in applications such as water desalinization, gas generation, and fuel cells. The chemical structure of Nafion is shown in Figure 1.2 (Nemat-Nasser and Li, 2000). The selective permeability results from the sulfonic acid (SO_3^-) groups that are bound to the sidechains of the polymer backbone. When the polymer is hydrated, the positively charged ions associated with the SO_3^- groups become mobile, allowing the polymer to conduct cations. This ion mobility is believed to be directly responsible for the electromechanical transduction in ionic polymer transducers. Shahinpoor and Kim (2000) have demonstrated that ionic polymer actuator performance even depends on the choice of cation. The details of the role of the mobile cations in electromechanical transduction, however, are not fully understood.

The process of plating the ionic polymer base material is not trivial. Because of Nafion's chemical composition (similar to Teflon in many respects), most conventional plating methods will not produce a durable, flexible electrode. The most popular plating method is an impregnation/reduction process in which the mobile cations in the hydrated ionic polymer are replaced with cationic groups containing the metal of which the electrode is to be made. Next the polymer is placed in a reducing agent. The cations near the polymer surface are reduced, resulting in a network of metal particles that interpenetrates the membrane near its surface. This process is repeated until a metallic surface with suitable conductivity is formed. Because some of the metal particles are formed within the polymer, the adhesion issues that plague other plating methods are overcome. For a more detailed description of the impregnation/reduction process and a thorough review of the various plating methods employed in the manufacture of ionic polymer transducers, the reader is referred to the work of Bennett (2002).

Several of the characteristics of ionic polymer transducers that differentiate them from other distributed transducers can be considered advantageous. An example is the fact that actuation is possible with low electric fields – typically no more than a few volts are required. These small potentials can be easily managed by simple control circuits. Also the fact that they operate at low voltages makes ionic polymer actuators well suited to battery powered devices. Because the base material and precious metal electrodes are chemically stable, the transducers are considered to be bio-compatible. This feature, coupled with the fact that the transducers can operate in an aqueous environment, has prompted some researchers to conceive biomedical devices based on ionic polymer transducers. For example, Shahinpoor and Kim (2001) proposed a heart-assist device, and Guo et al. (1996) proposed an active catheter that is guided using ionic polymer transducers. Also, Keshavarzi et al. (1999) suggested the idea of using an ionic polymer transducer to measure blood pressure. Another distinguishing feature of ionic polymer transducers is that they are relatively soft. Their modulus is on the order of 0.1GPa. Konyo et al. (2001) attempted to exploit this trait and presented a 'tactile display' intended to convey how various materials feel to the human touch. A review of the majority of the applications proposed over the last several years is presented by Tadokoro et al. (2001). Note that ionic polymer transducers are an emerging technology, and researchers are still seeking a niche for them. The applications mentioned above are laboratory demonstrations of concepts – ionic polymer transducers

have not yet found their way out of the laboratory and into practical applications. One of the barriers to their use in practical applications is the lack of suitable engineering models, an issue addressed in this work.

1.3 Literature Review

1.3.1 Characterization

Since ionic polymer transducers were first presented in 1992, several researchers have begun to investigate their behavior. For example, Mojarrad and Shahinpoor (1997a) presented plots of blocked force versus time for an ionic polymer bender subjected to sinusoidal, triangular, square, and sawtooth waveforms. Shahinpoor et al. (1997) showed displacement versus frequency for a 2V periodic input. A review encompassing many of the earlier efforts is presented in Shahinpoor et al. (1998). Most ionic polymer transducer experiments have been performed on samples based on DuPont's Nafion 117, a readily available commercial polymer that is approximately 180μm thick. After plating, a fully hydrated Nafion 117 based ionic polymer transducer is approximately 200μm thick. The overwhelming majority of experiments have been performed on transducers in a cantilevered bender configuration.. Typical dimensions are 5mm wide and 15mm or more in length. They function best in the fully hydrated state, and their performance as actuators decreases rapidly as they dry out. Ionic polymers are 'soft' transducers – reported values of their modulus vary from approximately 0.1GPa (Bar-Cohen et al., 2001a) to over 0.6GPa (Nemat-Nasser and Li, 2000). Note that this modulus includes the stiffening effect of the electrode, which is significant. Since the electrode thickness and structure depend on the details of the plating process, which has not been standardized and has also been described as difficult to control, a wide range of reported moduli is plausible.

Although the experimental data presented by various researchers correspond to transducers with different dimensions, electrode materials, neutralizing ions, etc, it is still possible to glean the general attributes of ionic polymer transducers from this collection of experimental results. Following is a summary of the actuation and sensing characteristics of ionic polymer transducers, as reported in the literature.

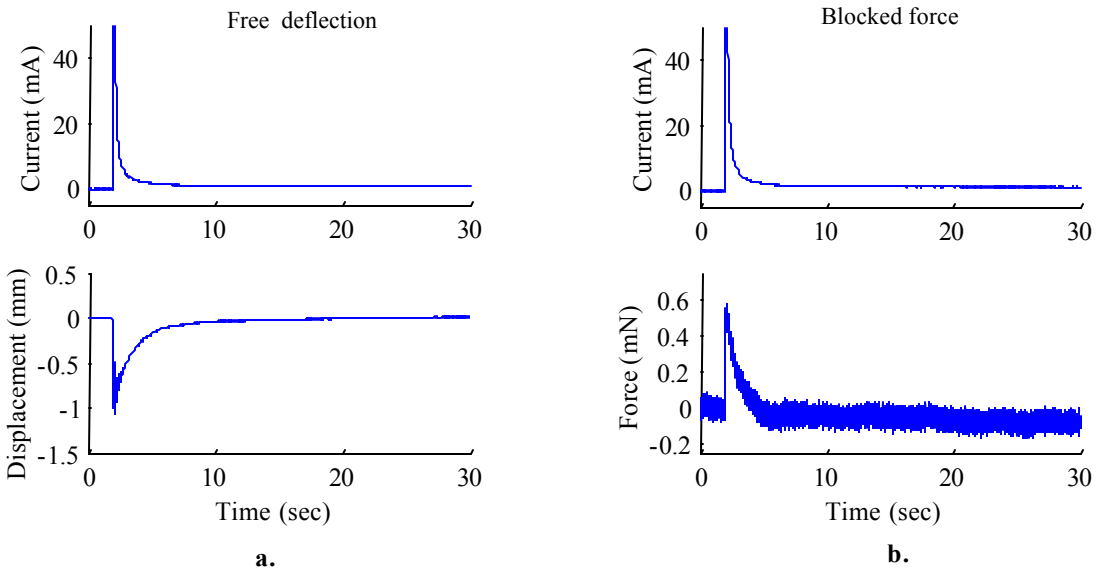

Figure 1.3: Step response of a cantilevered ionic polymer bender.

Actuation

When an electric field is applied to an ionic polymer bender, a significant curvature is induced within milliseconds. If the motion of the actuator is unrestricted, the displacement of the tip is called the free deflection. Figure 1.3a contains free deflection and current response plots for a Nafion based 5mm x 20mm cantilevered ionic polymer transducer to which a 1V step has been applied. If actuator motion is prevented, the force exerted on the object restricting the actuator's motion is called the blocked force. A blocked force response and the corresponding current response with a -1V step is shown in Figure 1.3b. In both plots, the initial mechanical response is rapid; however, a slow relaxation occurs while the voltage is held constant. If one uses the steady-state response to characterize the speed of actuation, the bandwidth of ionic polymer transducers is quite low, on the order of 0.1Hz. The transducers are highly capacitive, indicated by the high initial current and rapid decrease to a low steady-state value. When the transducer electrodes are grounded, much of the charge that was delivered to the actuators is returned. Relative to other solid-state transducers, such as piezoelectric materials, the ionic polymer bender's deflection is very large relative to the applied field. The forces produced by these actuators, however, are quite small. Most researchers have reported blocked force measurements ranging from 0.5 to 5mN for similarly sized actuators.

Ionic polymer actuators cannot tolerate high voltages (greater than approximately

10V) without sustaining permanent damage. Most experiments reported in the literature have been performed with 3V or lower signals – only a few researchers describe experiments in which the applied voltage has exceeded 5V. Another important consideration is that if voltages above 1.23V are applied, electrolysis occurs, converting the hydration water that the polymer has absorbed into hydrogen and oxygen, thereby dehydrating the actuator. Even if the applied voltage is below the threshold for electrolysis, the hydration water will slowly evaporate, hindering actuator performance. To avoid the dehydration issue, some have performed their experiments with the actuators submerged in an aqueous solution.

Interestingly, ionic polymer actuators, which must be hydrated to function, have been shown to work at very low temperatures, down to -100 degrees Centigrade, and at low pressures, 0.4 to 1 Torr (Shahinpoor et al., 1998). In fact, the deflection with a 0.1Hz 3V sine input was observed to increase with decreasing temperature.

One topic on which researchers disagree is whether or not ionic polymer transducers can be used for DC actuation. The degree to which the relaxation occurs appears to vary significantly from experiment to experiment, and the factors responsible for these variations have not been conclusively identified.

Sensing

Less effort has been spent exploring the sensing capabilities of ionic polymer transducers. The first report of ionic polymer transducer sensing was published by Sadeghipour et al. (1992), who created a Nafion based accelerometer. They fabricated a wafer-like cell that applied pressure across the thickness of a piece of Pt plated Nafion, and they measured the voltage output. The cell was approximately 2 inches in diameter, and its sensitivity was on the order of 10mV/g. An interesting feature of their work is that the Nafion was not hydrated. Prior to use, it was saturated with hydrogen under high pressure. Also, the load was applied across the polymer's thickness, while most other ionic polymer transducer research has been performed using cantilevered benders.

Ionic polymer transducers are unsuitable for static displacement sensing. Mojarrad and Shahinpoor (1997b) investigated displacement sensing by measuring output voltage versus applied tip displacement for a cantilevered ionic polymer transducer and observed that the output was dependent on the orientation of the transducer with respect to the electrodes. If the transducer was rotated 180 degrees about its longitudinal axis and placed

back in the fixture, the slope of the voltage versus displacement curve had the opposite sign as the original experiment. Also, the voltage output contained offset voltages that were on the same order or larger than the signal that corresponded to displacement. When the direction of the applied displacement was reversed, there appeared to be no correspondence between the output voltage and the applied displacement.

Motivated by the idea of measuring pressure in the human spine, Ferrara et al. (1999) applied pressure across the thickness of a 4 cm^2 Nafion based ionic polymer transducer while measuring the output voltage. Unlike the work of Sadeghipour et al. (1992), they hydrated the transducer before testing. The applied load was steadily increased from 0 to approximately 500kPa over 20 seconds, then removed at the same rate. The output voltage approached 100mV at its peak, but it did not decay as quickly as the load was reduced – the output voltage did not return to 0V until approximately 40 seconds after the load had been completely removed. The experiment was repeated with a maximum stress of almost 900kPa, and the results were similar.

More recently, Henderson et al. (2001) performed an experimental frequency-domain analysis of the output voltage with a tip displacement input for a cantilevered bender. Their purpose was to evaluate the suitability of ionic polymer transducers for use in near-DC accelerometers. The transducer used in the experiment was allowed to dry, in typical atmospheric conditions, for approximately one month before testing. They observed a sensitivity of approximately 50mV/m for an 11mm x 29mm cantilever and concluded that ionic polymer transducers might be a useful technology for low-frequency accelerometer applications.

1.3.2 Modeling

Most of the models proposed for ionic polymer transducers can be placed in one of three categories, physical models, black box models, and gray box models. For the physical models, researchers selected and modeled the set of underlying mechanisms they believe to be responsible for the electromechanical transduction and subsequent deformation (actuation) or electrical output (sensing). For the black box models, also called empirical models and phenomenological models, the physics are only a minor consideration, and the model parameters are based solely on system identification. The gray box models employ a combination of well-established physical laws and empirically determined parameters that have physical

interpretations.

Physical Models

One of the early physical models is a continuum actuator model proposed by Shahinpoor (1995), in which the electric field induced osmotic pressure is considered the dominant mechanism; however, no solution to the model was proposed. The first complete physical models that were both solved and compared to experimental results were not published until 2000 (Tadokoro et al., 2000; Nemat-Nasser and Li, 2000).

Tadokoro et al. (2000) presented what they termed a 'white-box' model for ionic polymer actuators. They proposed that the application of a step voltage (electric field) causes the mobile cations to quickly migrate across the thickness of the actuator from the anode (positive electrode) to the cathode (negative electrode), dragging water molecules along with them. The resulting change in water concentration, a decrease at the anode and an increase at the cathode, causes contraction and expansion of the respective portions of the base polymer and induces a curvature in the actuator. On a slower time scale, osmotic pressure causes the water to diffuse in such a matter that the concentration is equalized across the thickness, resulting in a relaxation from the large curvature that was initially induced. Electrostatic forces were also considered to be significant, though on a smaller scale than the ion and water migration. Tadokoro et al. proposed that the electrostatic forces between adjacent fixed anionic groups, a result of the charge imbalance caused by the ion migration, induced a small amount of curvature towards the cathode – opposite the direction of the initial curvature. This reverse bending was consistent with their experimental observations. The resulting mathematical model was a system of coupled partial-differential equations with some material parameters that were not well known or directly measurable. After simplifying assumptions were made, the model was solved and the results compared to an experimental voltage step response. Agreement between the experimental and simulated tip displacement was good.

A micromechanics model was presented by Nemat-Nasser and Li (2000). They also proposed a redistribution of the cations under application of an electric field, but their treatment of the electrostatic forces was very different from that of Tadokoro et al. (2000). Central to the micromechanics model is the idea that the sidechains of the polymer form clusters, which are saturated by water when the polymer is hydrated. Under the applica-

tion of an electric field, the cations are redistributed, migrating towards the cathode. A locally imbalanced net charge density results and the associated electrostatic forces produce stresses that act on the polymer backbone, resulting in an electrically induced curvature of the actuator. A simulation was presented and compared to an experiment in which the tip displacement was measured while a low-frequency sinusoidal voltage was applied, and the agreement was good. Nemet-Nasser and Li reported that when operated in air and given a step input, the actuator bent towards the anode and did not relax towards the initial position. They reported that, when operated in water and given the same input, the actuator slowly relaxed towards the initial position. Based on their experimental observations and model, Nemet-Nasser and Li concluded that the electrically induced motion of the ionic polymer actuator was due almost entirely to electrostatic forces. If operated in water, a slow redistribution of water molecules may occur and cause a secondary effect, the relaxation towards the initial position. Note that these conclusions are directly opposite those of Tadokoro et al. (2000), yet both models agree with experimental data. In the white-box model, the electrostatic forces are secondary and cause bending towards the cathode. In the model presented by Nemet-Nasser and Li, the electrostatic forces are dominant and cause bending towards the anode. Nemet-Nasser and Li also considered sensing with ionic polymer transducers. They proposed that the displacement of the polymer causes a differential displacement of the effective charge centers of the anions and cations of each cluster. This differential displacement results in an electric potential across the transducer. Again, the simulated results compared well with an experiment.

In a later paper, Nemat-Nasser (2002) revised the 'cluster model' and focused only on the micro-mechanics he proposed are responsible for actuation. Unlike the previous work (Nemat-Nasser and Li, 2000), he reported observing a slow relaxation towards the cathode after the initial motion towards the anode when a step voltage is applied to an actuator operated in air. The revised model is still based on the cluster morphology and the redistribution of cations under the application of an electric field. However, it also includes the effects of the hydration level and the water migration caused by the cation redistribution, factors not considered in the previous model. Even with these factor considered, Nemet-Nasser still reasoned that ionic polymer actuator motion is due predominantly to electrostatic forces. He also concluded that all of the critical processes responsible for actuation occur within boundary layers that form at the anode and cathode when an electric

field is applied. He credited the relaxation to a slow redistribution of the cations in the cathode boundary layer.

One difficulty with physical modeling of ionic polymer transducers is that the chemical and/or physical mechanisms responsible for the electromechanical transduction have not been conclusively identified. Also, the material parameters that appear in many of the proposed equations are not well known and do not lend themselves to direct measurement. These statements are strongly supported by the fact that the detailed physical models proposed by Tadokoro et al. (2000) and Nemat-Nasser and Li (2000) do not agree on the role of the actuation mechanisms, yet they both compare well to experiments. Another issue with the physical models is that the governing equations are quite complex. These models will most likely prove useful in identifying and understanding the mechanisms responsible for transduction; however, much simpler models are needed for engineering design.

Black Box Models

The first black box model of ionic polymer transducer actuation was presented by Kanno et al. (1994). They modeled the tip displacement Y_t of a cantilevered bender with the expression

$$Y_t = Ae^{-\alpha t} + Be^{-\beta t} + Ce^{-\gamma t} + De^{-\delta t} + E, \tag{1.1}$$

where A through E and α through δ are constants, and t represents time. They used experimental tip displacement data with voltage step inputs in conjunction with a least squares algorithm to determine values for the constants. First, data from a 1.5V step experiment was used to determine values for all of the constants. Then, the experiment was repeated with step inputs ranging from 0.5V to 1.5V, in 0.1V increments, and values were determined for A through E at each voltage level. The reported values of A through E did not vary linearly with input voltage, in fact, two of the constants underwent a sign change as the input level was varied. The lack of a linear relationship suggests that ionic polymer actuator behavior cannot be modeled using a linear, time-invariant system, at least in the input range considered. However, it may also be a result of the inconsistent step response behavior observed by the author and other researchers (Nemat-Nasser, 2002). The nonlinear relationship between the constants and the input level was not discussed by Kanno et al.

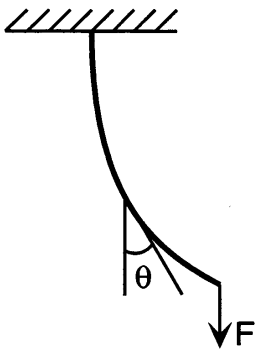

Figure 1.4: Actuator configuration for the Xiao and Bhattacharya (2001) model.

Another black box model for cantilevered ionic polymer benders was put forth by Xiao and Bhattacharya (2001). They used the first-order differential equation

$$\frac{d\mathcal{K}}{dt} = \frac{1}{\tau}(\mathcal{K}_v V - \mathcal{K}) \tag{1.2}$$

to describe the induced curvature $\mathcal{K}$ of a cantilevered bender suspended vertically, as shown in Figure 1.4. In equation (1.2), V is the applied voltage, τ is a time constant, and $\mathcal{K}_v$ represents the maximum induced curvature per unit applied voltage when the applied force F is zero. Both $\mathcal{K}_v$ and τ are considered material parameters and are determined by curve fitting to experimental data. To accommodate a nonzero F, the strain energy was considered. At each time step of a simulation, the deflection θ was determined by assuming that the sum of the strain energy in the actuator and the work done against the load F is equal to the strain energy that would be present in the actuator in the no-load case. The no-load strain energy versus time was based on the solution of equation (1.2). Simulations were compared to experimental results for an actuator with zero load and for an actuator lifting a 25mg mass, and the agreement was good.

While the black box models are relatively easy to understand and use, their scope is limited as they cannot accommodate any changes in actuator dimensions.

Gray Box Models

An alternative to the complicated physical models and the simplistic black box models, which are not scalable, are gray box models. These models incorporate well understood and easily modeled physical laws and use empirically determined parameters to represent the processes that are more complex and/or not well understood. The first and most

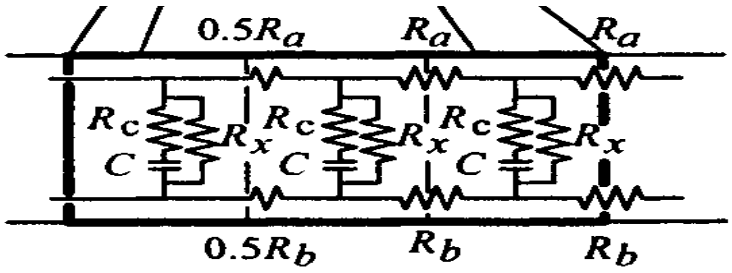

Figure 1.5: Equivalent circuit for the gray box model presented by Kanno et al. (1996)

widely accepted gray box actuator model was presented by Kanno et al. (1996). They represented the ionic polymer actuator using three 'stages' that were connected in series, an electrical stage, a stress-generation stage, and a mechanical stage. For the electrical stage, the actuator was broken into discrete, one mm long elements along its length. For the stress-generation and elastic stages, it was further subdivided into three layers through its thickness. In the electrical stage, each set of elements along the length was modeled using the equivalent circuit shown in Figure 1.5. The input of the electrical stage was the applied voltage and the output was current. This current was used as an input to the stress-generation stage, the behavior of which was governed by the relation

$$\sigma = D\varepsilon - e\{\frac{\omega_n^2}{s^2 + 2\zeta\omega_n s + \omega_n^2}\}I, \tag{1.3}$$

where σ is the stress in the material, D is a mechanical characteristic matrix based on the polymer actuator constitutive properties, and ε is the strain. The induced stress was determined by the product of e, the stress-generation tensor, and the electrical current I, and was assumed to act on the outer two layers only. The second-order terms ω_n and ζ were used to provide dynamics in the relationship between the current and the induced stress. The mechanical stage consisted of a dynamic finite element model with proportional damping. The model was validated by comparing simulated and experimental results of the tip displacement with a step voltage input for a cantilevered bender. No verification of the model's scalability was presented. Note that this approach only accounts for the effect of the electrical response on the mechanical motion – it does not allow the mechanical motion to affect the electrical response. The bidirectional energy conversion must be represented if

a model is to be used for both sensing and actuation.

DeGennes et al. (2000) proposed another linear gray box model for the static case. This model is based on the premise that the water dragged by the migrating ions is responsible for the induced curvature. The transducer behavior was described by the relation

$$\begin{aligned} J &= \sigma E - L_{12}\nabla p \\ Q &= L_{21}E - K\nabla p, \end{aligned} \tag{1.4}$$

where J represents the current density in the transverse direction, Q is the water flux, E is the electric field, p is the water pressure, and K is the Darcy permeability. The cross coefficients L_{12} and L_{21} represent the electromechanical transduction. These equations model the charge transport and the water transport in the material. Although this model has a form that is conducive to developing a coupled actuator model for the material, it was only proposed as a steady-state model and is unable to represent any dynamics due to base polymer of the actuator. In addition, the water transport phenomenon described by the equations has not yet been conclusively linked to ionic polymer behavior. Lastly, no comparison to experimental data was published.

1.3.3 Feedback Control

Since the current research includes a demonstration of feedback control with ionic polymer transducers, a brief account of previous research efforts in this area is given. The first reported use of feedback control to improve the performance of an ionic polymer transducer was presented by Mallavarapu et al. (2001). Their goals were to improve the response time and reduce the large peak typically seen in the step response of a cantilevered ionic polymer bender. A laser vibrometer was used to measure the tip displacement, and the control algorithm was implemented using a DSP. To aid in compensator design, the empirical approach of Kanno et al. (1994) was used, yielding a transfer function with one zero and two poles. Full state feedback was employed, and the gain vector was determined using the Linear Quadratic Regulator optimal control technique. The states were estimated by a linear observer-estimator. They achieved a significant improvement in the actuator's response – settling time was reduced by a factor of approximately 10, and the overshoot seen in the open-loop response was virtually eliminated. Experimental data were compared to simulations for several gain vectors, and the simulated performance was not realized for the more aggressive compensators because of the transducer's resonant frequency, which

was not modeled. In a later work, Mallavarapu (2001) included a resonant term in the empirical model used for compensator design. This change led to further improvements in the closed-loop performance; however, experiments were still hampered by the fact that the resonant frequency of the transducer changes with hydration level.

Kothera and Leo (2002) are investigating integral control for a cantilevered ionic polymer bender. Again, the feedback signal is provided using a laser vibrometer aimed near the tip of the actuator. As with the work by Mallavarapu et al. (2001), the model used for compensator design and simulation is similar to the empirical model that first appeared in Kanno et al. (1994). Simulations indicate that, using integral control, bandwidths of up to 80Hz are attainable. It is also proposed that the integral control will reduce the sensitivity of the closed-loop performance to modeling errors and inconsistencies in the actuator's open-loop response.

1.4 Research Goals and Contributions

The fundamental goal of this research is to enhance the scientific and engineering communities' understanding of the macroscopic behavior of ionic polymer transducers. This objective is accomplished through a combination of modeling and experimental work. Secondary goals include development of a model that facilitates the design of devices utilizing ionic polymer transducers and demonstration of a device that incorporates an ionic polymer sensor.

The model presented in this work is a simple, linearly coupled, scalable, dynamic model that represents the electromechanical coupling with a single, frequency-dependent term. None of the models presented in the literature incorporate all these features. The physical models are extremely complex, and the empirical models are not scalable. Also, with the purely empirical approach, separate models are required to represent sensing and actuation. While it is scalable, the gray-box model put forth by Kanno et al. (1996) is not coupled, so it cannot be used to represent ionic polymer sensors. The gray-box model proposed by DeGennes et al. (2000) is linearly coupled, but was only proposed as a static model. Also, the model's ability to predict ionic polymer transducer behavior was not compared to experimental data.

In this research, actuator and sensor equations are presented for the cantilevered

bender. The equations are written in terms of transducer dimensions and a few key material parameters, permitting the performance of the materials from which the transducers are made to be evaluated independent of transducer dimensions. Conversely, these equations will facilitate the design of systems employing ionic polymer transducers because a designer can predict the effects that varying transducer size will have on performance. To help place ionic polymer transducer performance in perspective, a comparison to piezoelectric transducers is provided. This comparison is presented in terms of blocked force, free deflection, and energy density of identically sized actuators. Also, the sensitivity of polymer sensors is compared to piezoelectric sensors.

The main purpose of the experimental results presented in this work is model validation. However, they also provide a thorough, well documented, experimental account of the manner in which blocked force, free deflection, and sensitivity of Nafion based ionic polymer transducers vary with cantilevered bender dimensions. A study of this nature has not yet been published. In cases where experiments performed in this research overlap the scope of previously published results, the new data will still be useful for the sake of comparison. This statement is based on the fact that the range of published results for some experiments is surprisingly large, for example, the range of blocked force results for actuators with similar dimensions and inputs varies by an order of magnitude.

Another contribution of this work is that reciprocity between actuating and sensing has been both predicted by the model and demonstrated experimentally. It is hoped that this demonstration, along with the reduction of the electromechanical coupling to a single term, will aid the ongoing efforts to explain ionic polymer transducer behavior in terms of physical mechanisms.

This document also describes the first experiments performed to quantify a nonlinear actuation phenomenon that has been labeled the 'electrically induced permanent strain' phenomenon. This phenomenon only occurs with certain inputs and is shown to be related to the amount of electrical charge delivered to the actuator.

The goal of demonstrating an application incorporating an ionic polymer sensor was achieved by applying feedback control to a rotary device that was driven by multiple ionic polymer actuators. The feedback signal was provided by the ionic polymer sensor used to monitor the displacement of the device. This is the first published experiment in which an ionic polymer sensor has been used with a feedback control scheme. The application was

also used to show the utility of the model presented in this work. The model was first used to determine the feasibility of the device from a mechanical standpoint. After the device was designed, the model was utilized to predict open-loop and closed-loop performance for the purpose of control law design.

1.5 Overview

The transducer model is introduced in Chapter 2. It is then solved for equations that can be used to represent sensing and actuation with cantilevered benders. The model parameters are identified experimentally in Chapter 3, and the model is validated by comparing predicted and experimental responses . In addition, the ability of the model to predict changes in performance as transducer dimensions are varied is confirmed. A thorough evaluation of the sensing and actuation capabilities of cantilevered ionic polymer benders follows in Chapter 4, along with a comparison to piezoelectric transducers. The last section of Chapter 4 presents an interesting nonlinear phenomenon not previously investigated. Chapter 5 describes a feedback control experiment in which ionic polymer transducers were employed as both actuators and as the feedback sensor. Lastly, Chapter 6 presents conclusions based on this research, and recommendations for future work are provided.

Chapter 2

Electromechanical Modeling

In this chapter, an equivalent-circuit model is presented for ionic polymer transducers. The coupling between the mechanical and electrical domains is modeled using a pair of linearly coupled equations, and the other circuit parameters are based on well-known physics. The circuit is analyzed to develop input-output relationships for both sensing and actuation using a cantilevered bender. The resulting expressions show the relationships between transducer performance, material parameters, and transducer dimensions. This knowledge permits the model to be used as a design tool. In addition, it provides a means through which material performance (independent of transducer dimensions) can be extracted from experimental data.

2.1 Equivalent-Circuit Model

A convenient and often accurate assumption used in mathematical modeling of electromechanical devices is that the variables in the electrical and mechanical domains are linearly coupled. Energy conversion between the two domains can be produced by a change in the state variables of the system. Ikeda (1996) presents a thermodynamic argument, based on a quadratic expression for the free energy of such a system, showing that the constitutive relations consist of a pair of symmetric, linearly coupled equations

$$\begin{aligned} H &= a_{11}\eta + a_{12}x \\ X &= a_{12}\eta + a_{22}x. \end{aligned} \tag{2.1}$$

Ikeda refers to η and x as extensive variables and calls H and X the generalized forces, or intensive variables. The linear coupling is represented by a_{12}, and the fact that the

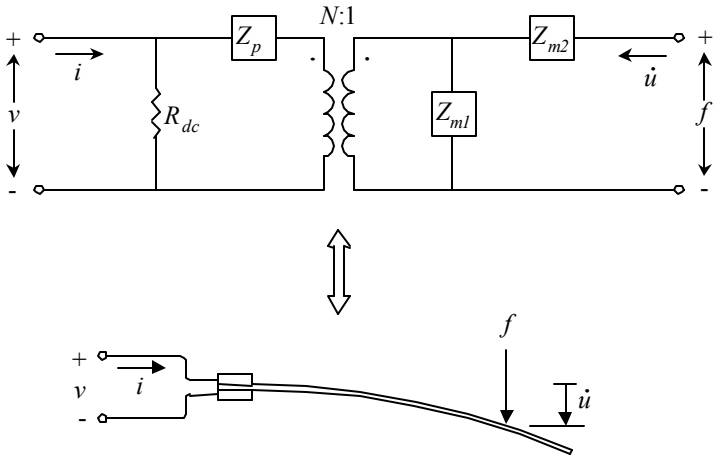

Figure 2.1: Equivalent circuit for ionic polymer transducer

equations are symmetric indicates that reciprocity exists between the two domains. Because of the coupling, a_{11} and a_{22} must be defined for constant (usually zero) x and η, respectively. A similar approach is taken in literature pertaining to the fundamentals of linear piezoelectricity. For example, Tiersten (1969) starts with a conservation of energy statement and derives a pair of piezoelectric constitutive equations whose form is identical to equation (2.1). In this work, the assumption of linear coupling between the mechanical and electrical domains will be applied to ionic polymer transducers; however, unlike the approach used for piezoelectric materials, the coupling term will be frequency dependent.

It is sometimes helpful to model an electromechanical transducer using an equivalent circuit. Equivalent-circuit models are advantageous because they can provide an intuitive, graphical representation of the governing equations of an electromechanical system. Defined properly, the individual circuit elements have clear physical interpretations, and the user can examine the relationships between the various elements without being forced to study the underlying equations. Only linear circuits are considered in this work, and Laplace-domain circuit analysis provides a straightforward means for obtaining the relationships between any set of system variables. The linear coupling between the electrical and mechanical domains can be represented using an ideal, linear transformer, as shown in Figure 2.1. This type of modeling has been used to represent electromagnetic speakers (Beranek, 1954), piezoelectric transducers (Ikeda, 1996; Germano, 1972), as well as electrostatic devices.

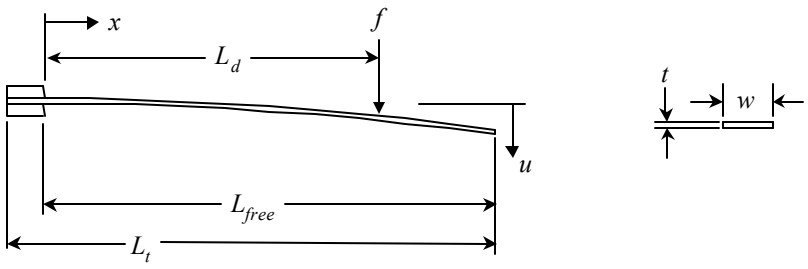

Figure 2.2: Transducer dimensions used for mechanical terms of equivalent circuit

In Figure 2.1, the electrical quantities are shown on the left side of the transformer, and the mechanical quantities are on the right. Transducer voltage and current are denoted by v and i, respectively. The external force applied to the transducer is represented by f, and the velocity of the force application point is $\dot{u}$.

In the following sections, Laplace-domain expressions for each of the circuit elements are developed for a cantilevered bender.

2.1.1 Mechanical Terms

The portion of the mechanical impedance due to the stiffness of the polymer transducer is represented in Figure 2.1 by Z_{m1}. For a cantilevered bender, an expression for the mechanical stiffness can be derived by considering the quasi-static relationship between applied force and deflection for an Euler-Bernoulli beam. The application of a load f at a distance L_d from the supported end, as shown in Figure 2.2, results in a bending moment

$$M = f(L_d - x), \tag{2.2}$$

where x is the distance from the supported end along the length of the bender. For small deflections, the bending moment and the deflection are related through (Shigley and Mischke, 1989)

$$\frac{M}{YI} = \frac{d^2u}{dx^2}, \tag{2.3}$$

where Y is the Young's (elastic) modulus, and I is the area moment of inertia of the bender's cross section. Substituting equation (2.2) into equation (2.3) and integrating twice

with respect to x gives

$$u(x) = \frac{f}{YI}(\frac{L_d x^2}{2} - \frac{x^3}{6} + C_1 x + C_2), \tag{2.4}$$

where C_1 and C_2 are constants of integration. Incorporating the boundary conditions for a cantilevered beam ($u(x=0) = 0$ and $\frac{du}{dx}(x=0) = 0$), writing the area moment of inertia in terms of the transducer's width w and thickness t, and evaluating at $x = L_d$ yields the expression

$$u = f\frac{4L_d^3}{Ywt^3}. \tag{2.5}$$

To obtain a Laplace-domain expression for Z_{m1}, which represents force over velocity (well below resonance), equation (2.5) is multiplied by the Laplace variable s and solved for $\frac{f}{su}$. The result is

$$Z_{m1} = \frac{1}{s}\frac{Ywt^3}{4L_d^3}. \tag{2.6}$$

Unlike linear-elastic materials (e.g. steel, aluminum), polymers typically exhibit viscoelastic behavior, in which the stress-strain relationship has both liquid-like and solid-like features (Ward and Hadley, 1993). If linear-viscoelastic behavior is assumed, the stress in the polymer is linearly related to both the strain and the strain rate, a combination of linear-elastic and viscous behavior. This type of response is often described mathematically using a stress relaxation function $G(\tau)$, which represents the stress response to a unit strain input. The expression for a one-dimensional stress-strain relationship in a linear-viscoelastic material can be written as

$$\sigma(\tau) = G(\tau)e(0) + \int_0^\tau G(\tau - \xi)\frac{d}{d\xi}e(\xi)\, d\xi, \tag{2.7}$$

where e is the strain and σ is the stress. The integral's lower limit of zero (as opposed to $-\infty$) is based on the assumption that, prior to $\tau = 0$, the strain has been at zero several times longer than the slowest time constants in $G(\tau)$. Applying Laplace transform analysis to equation (2.7), the stress-strain relationship can also be represented using a complex modulus

$$Y^*(\omega) = Y_1(\omega) + jY_2(\omega), \tag{2.8}$$

where Y_1 represents the storage modulus, the linear-elastic component of the viscoelastic material's behavior, and Y_2 represents the loss modulus, the viscous (dissipative) component of the behavior. One of the simplest models that accurately represents a linear-viscoelastic

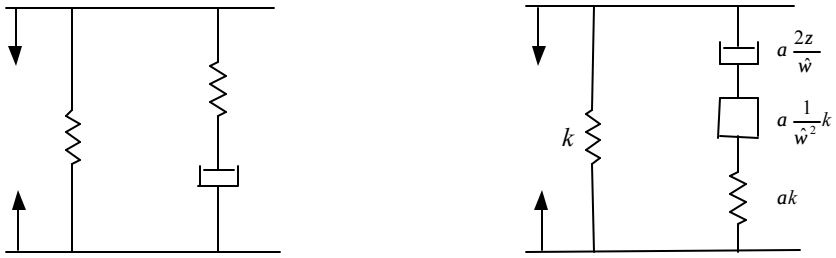

Figure 2.3: Models for linear viscoelasticity: a) Standard linear solid model, b) GHM method.

material is the 'standard linear solid' model (Ward and Hadley, 1993) shown in Figure 2.3a. The equilibrium, or quasi-static modulus is represented by the spring on the left, and the spring and damper connected in series account for the additional (beyond the quasi-static stress) stress levels that will occur at higher frequencies. McTavish and Hughes (1993) presented a similar approach, referred to as the GHM Method. They added a mass in series with the spring and damper, as shown in Figure 2.3b, to create what they termed a 'mini-oscillator.' Like the standard linear solid model, the physical interpretation of the forces generated by the mini-oscillator is that they account for the stress levels beyond the quasi-static values. The GHM Method is well suited to structural analysis because it preserves the desired symmetry and definiteness of the mass, damping, and stiffness matrices that define a typical second order structural model. Because its generality, the GHM method will be employed to represent the viscoelastic behavior of the ionic polymer transducers.

The combined stiffness of the two branches in Figure 2.3b is

$$k\left(1+\alpha\frac{s^2+2\zeta\hat{\omega}s}{s^2+2\zeta\hat{\omega}s+\hat{\omega}^2}\right), \tag{2.9}$$

where α, ζ, and $\hat{\omega}$ are the 'GHM parameters' that determine the frequency dependence of the modulus. The static stiffness is represented by k. To apply the GHM method to ionic polymers, k is replaced by Y_∞, the static modulus, resulting in the expression

$$Y = Y_\infty\left(1+\alpha\frac{s^2+2\zeta\hat{\omega}s}{s^2+2\zeta\hat{\omega}s+\hat{\omega}^2}\right). \tag{2.10}$$

This equation for Y will be used in the mechanical stiffness term Z_{m1} (equation (2.6)).

The useful frequency range of the transducer model can extended by adding an inertial term, represented by Z_{m2} in Figure 2.1. This term will improve the model accuracy

as frequencies approach the first natural frequency of the bender. In general, the mass term is derived using the quasi-static bender stiffness (derived earlier in this section), along with the closed form solution for the bender's natural frequency, to determine an equivalent mass.

The natural frequencies for transverse vibration of a slender beam are given by (Inman, 1994)

$$\omega_n = \frac{\Gamma^2}{L_{free}^2}\sqrt{\frac{Y_\infty I}{\rho_m A}}, \tag{2.11}$$

where Γ is the solution to the characteristic equation, ρ_m is the transducer's density, A is the cross-sectional area, and L_{free} is the unsupported length of the transducer, as shown in Figure 2.2. The value of Γ for the first mode of a clamped-free beam is 1.875 .

The well-known relationship

$$\omega_n^2 = \frac{k}{m} \tag{2.12}$$

between stiffness k, mass m, and natural frequency of a single degree of freedom system can be used in conjunction with equations (2.11) and (2.5) to determine an equivalent mass for the polymer transducer. First, equation (2.5) is solved for the transducer stiffness (force over displacement at the driving point). The result, along with equation (2.11) is substituted into equation (2.12). Solving for the equivalent mass gives

$$m = \frac{3L_{free}^4 \rho_m w t}{L_d^3 \Gamma^4}. \tag{2.13}$$

To convert equation (2.13) to an expression for Z_{m2}, consider Newton's Second Law, written in the Laplace-domain

$$f = s^2 m u. \tag{2.14}$$

Substituting equation (2.13) for the mass and solving for force over velocity ($\frac{f}{su}$) gives

$$Z_{m2} = s\frac{3L_{free}^4 \rho_m w t}{L_d^3 \Gamma^4}. \tag{2.15}$$

It should be noted that the approximations for Z_{m1} and Z_{m2} will result in an accurate natural frequency prediction. However, as the operating frequency approaches the first natural frequency, the accuracy of the polymer transducer mechanical impedance will drop slightly. This inaccuracy is a result of the shape of the bender vibration 'shifting' towards the first mode shape from the quasi-static shape.

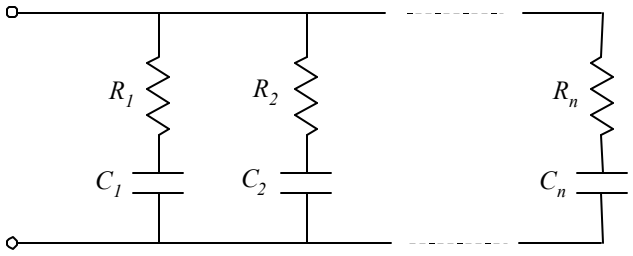

Figure 2.4: Circuit model for Z_p

2.1.2 Electrical Terms

The electrical impedance of the polymer transducer is represented by two terms in the equivalent circuit of Figure 2.1. The DC resistance is represented by R_{dc}, and Z_p models the ability of the transducer to store electrical charge. In order to produce simple expressions for R_{dc} and the circuit elements that will be used to describe Z_p, the polymer transducer will be viewed as a homogeneous material with perfectly conductive electrodes on both surfaces.

The DC resistance of the transducer, expressed in terms of a resistivity ρ_{dc} and the polymer dimensions is (Halliday and Resnick, 1978)

$$R_{dc} = \frac{\rho_{dc} t}{L_t w}, \tag{2.16}$$

where L_t is the total length of the transducer, including the length clamped between the electrodes.

The electrical impedance of the polymer is resistive with high magnitude at DC, resistive with small magnitude at high frequencies, and it has a strong capacitive component at intermediate frequencies. This behavior suggests that Z_p should consist of parallel branches of R-C elements that are connected in series, as shown in Figure 2.4. The number of branches n will determine the number of degrees of freedom available for describing the electrical impedance.

As with R_{dc}, each resistor R_i in Figure 2.4 can be represented by a resistivity ρ_i and the polymer dimensions using

$$R_i = \frac{\rho_i t}{L_t w}. \tag{2.17}$$

Viewing the polymer transducer as a parallel-plate capacitor, the C_i are (Halliday and Resnick, 1978)

$$C_i = \frac{\epsilon_i L_t w}{t}, \tag{2.18}$$

where the ϵ_i are permittivities.

Using Laplace-domain circuit analysis, the impedance Z_p of the circuit in Figure 2.4 is

$$Z_p = \frac{1}{\sum_{i=1}^{n} \frac{sC_i}{1+sC_iR_i}}. \tag{2.19}$$

Substituting equations (2.17) and (2.18) into this result yields

$$Z_p = \frac{t}{sL_t w} \frac{1}{\sum_{i=1}^{n} \frac{\epsilon_i}{1+s\epsilon_i\rho_i}}. \tag{2.20}$$

2.1.3 Electromechanical Coupling

The transformer in Figure 2.1, with turns ratio N, represents the electromechanical coupling. Typically, the transformer turns ratio in electromechanical equivalent-circuit models is a constant. Because of the complex nature of ionic polymer transducer behavior, the turns ratio in this work will be permitted to be frequency dependent. Consider the frequency range below resonance and above DC, where the mass term Z_{m2} is negligible and the DC resistance R_{dc} can be considered very large relative to the magnitude of Z_p. In this frequency range, the turns ratio N represents the relationship between open-circuit voltage and the external force acting on the polymer, specifically

$$\frac{v}{N} = \frac{f}{1} \text{ with } i = 0. \tag{2.21}$$

To develop an expression for N, first consider the constitutive equations for linear piezoelectricity (Ikeda, 1996)

$$\begin{aligned} S &= s^E T + dE \\ D &= dT + \epsilon^T E, \end{aligned} \tag{2.22}$$

where S and D are the mechanical and electrical displacements (strain and charge density), and T and E are the applied stress and the electric field. The variable s^E is the short-circuit (zero electric field) elastic compliance, and ϵ^T is the permittivity with no external loading (zero applied stress). The piezoelectric coupling is represented by d, which relates induced strain to applied electric field (first row of equation (2.22)) and generated charge per unit surface area to applied stress (second row of equation (2.22)). If we assume that

the coupling in ionic polymer transducers can be modeled in a similar fashion, the second row in equation (2.22) can be used to find an expression for the transformer turns ratio N. Towards this end, the permittivity ϵ^T is replaced by a frequency dependent term $\eta^T(s)$. This change is necessary because the electrical impedance of polymer transducers, unlike that of piezoelectric materials, cannot be accurately represented with capacitance alone. The expression for $\eta^T(s)$ can be found by comparing equation (2.20) for Z_p to equation (2.18) for a parallel plate capacitor. The resulting relation is

$$\eta^T(s) = \sum_{i=1}^{n} \frac{\epsilon_i^T}{1 + s\epsilon_i^T \rho_i^T}, \tag{2.23}$$

where the superscript T has been added to the ϵ_i and ρ_i to represent the zero applied stress condition. Also, some of the researchers who have attempted to understand the mechanisms responsible for the electromechanical coupling (Nemat-Nasser and Li, 2000) have suggested that the electromechanical coupling in ionic polymer transducers occurs at the interface between the electrode and the polymer itself. For this reason, T will be interpreted as the applied stress *at the polymer surface*.

To convert the electric displacement term in equation (2.22) to charge, both sides of the equation are integrated over the polymer width w and length L_t. Prior to integrating, the stress at the polymer surface T must be related to the applied force f. These two quantities can be related using the well-known equation for a beam in bending (Shigley and Mischke, 1989)

$$T = \frac{My}{I}, \tag{2.24}$$

where M is the applied moment, y is the distance from the neutral axis, and I is the area moment of inertia. Substituting $t/2$ for y and equation (2.2) for the moment yields

$$T(x) = \frac{f(L_d - x)t}{2I}. \tag{2.25}$$

The second row of equation (2.22) can now be written as

$$Q = \int_0^{L_t} \int_{-w/2}^{w/2} (d\frac{f(L_d - x)t}{2I} + \frac{\eta^T v}{t})\, dz\, dx, \tag{2.26}$$

where z is the coordinate in the direction of the polymer width. Integrating (remember that $f = 0$ for $x \geq L_d$) and substituting $I = wt^3/12$ results in the relation

$$Q = \frac{3dL_d^2}{t^2} f + \frac{\eta^T L_t w}{t} v. \tag{2.27}$$

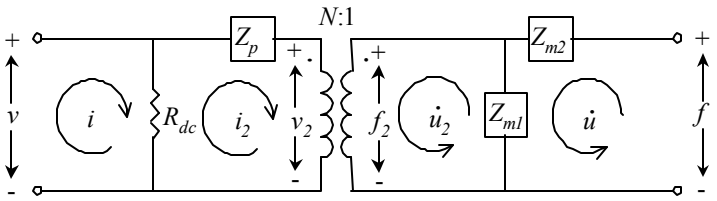

Figure 2.5: equivalent-circuit model with variables used for mesh-current circuit analysis

To obtain an expression for N, set $Q = 0$ (open-circuit condition) and solve for v/f. The resulting expression for the turns ratio N is

$$N = \frac{3dL_d^2}{\eta^T L_t w t}. \tag{2.28}$$

The derivation of the equivalent-circuit parameters is now complete. It is important to note that the above derivation only considers single axis bending and is therefore limited to slender beams. If the transducer becomes wide relative to its length (starts to becomes more like a plate than a beam), then bending about two axes should be considered.

2.2 Circuit Analysis

The equivalent circuit in Figure 2.1 can be analyzed to yield various input-output relationships, such as free deflection or blocked force with either a voltage or a current input. A useful intermediate step is to solve the circuit for a pair of linearly coupled equations that can represent the general behavior of the equivalent circuit. These coupled equations can be found by using the voltage and current relationships for ideal linear transformers and the mesh-current method of circuit analysis (Nilsson, 1983). Figure 2.5 shows the variables used in the mesh-current analysis. The resulting mesh equations, along with the relationships

between voltage and current for an ideal transformer are

$$\begin{aligned} v &= R_{dc}(i - i_2) \\ Z_p i_2 + v_2 + R_{dc}(i_2 - i) &= 0 \\ f_2 + Z_{m1}(\dot{u}_2 - \dot{u}) &= 0 \\ f &= Z_{m2}\dot{u} + Z_{m1}(\dot{u} - \dot{u}_2) \\ \tfrac{v_2}{N} &= \tfrac{f_2}{1} \\ -i_2 N &= \dot{u}_2. \end{aligned} \tag{2.29}$$

To obtain a pair of linearly coupled equations, the variables v_2, i_2, f_2, and $\dot{u}_2$ are eliminated from equation (2.29), resulting in the matrix equation

$$\begin{Bmatrix} v \\ \\ f \end{Bmatrix} = \begin{bmatrix} \frac{R_{dc}(N^2 Z_{m1}+Z_p)}{R_{dc}+N^2 Z_{m1}+Z_p} & \frac{N R_{dc} Z_{m1}}{R_{dc}+N^2 Z_{m1}+Z_p} \\ \\ \frac{N R_{dc} Z_{m1}}{R_{dc}+N^2 Z_{m1}+Z_p} & \frac{(Z_{m1}+Z_{m2})(R_{dc}+Z_p)+N^2 Z_{m1} Z_{m2}}{R_{dc}+N^2 Z_{m1}+Z_p} \end{bmatrix} \begin{Bmatrix} i \\ \\ \dot{u} \end{Bmatrix}. \tag{2.30}$$

This set of equations can also be viewed as a two-port model that describes the behavior of an ionic polymer bender, similar to the model presented by Newbury and Leo (2002). The advantage of the model in this work is that each of the matrix coefficients has been explicitly defined (see section 2.1) in terms of transducer dimensions and a set of basic material parameters. In short, unlike the previous two-port model, the model presented in this work is scalable.

The coefficients in equation (2.30) can be simplified by introducing the assumption that the reflected mechanical impedance is negligible relative to the electrical impedance term Z_p. This assumption takes two forms, depending on whether the blocked or free boundary condition is considered. For the blocked boundary condition, the assumption can be expressed as

$$N^2 Z_{m1} \ll Z_p. \tag{2.31}$$

For the free boundary condition, the assumption is

$$N^2 \frac{Z_{m1} Z_{m2}}{Z_{m1} + Z_{m2}} \ll Z_p. \tag{2.32}$$

Equations (2.31) and (2.32) will be used in section 2.3 to simplify the input-output relationships that are derived from equation (2.30). In Chapter 3, it will be shown experimentally that this assumption is valid for the ionic polymer transducers examined in this work.

2.3 Important Input-Output Relationships

It is useful to solve equation (2.30) for common input-output relationships, such as blocked force and free deflection, apply the assumptions in equations (2.31) and (2.32), then replace each circuit element with its definition in terms of the transducer dimensions and material parameters derived in section 2.1. The resulting expressions elucidate the relationships between the transducer's dimensions, the material parameters, and transducer performance. In solving for the input-output relations presented in the following sections, one of the variables in equation (2.30) is set to zero. Following the convention used by Ikeda (1996), the variable that is set to zero will be denoted using a superscript. For example,

$$(\frac{f}{v})^{\dot{u}} \tag{2.33}$$

will represent output force with a voltage input, when the velocity is held at zero. This relation is called the blocked force.

2.3.1 Actuator Equations

If $\dot{u}$ in equation (2.30) is set to zero, corresponding to the blocked boundary condition, the remaining equations can be solved for force over voltage, resulting in the expression

$$(\frac{f}{v})^{\dot{u}} = \frac{NZ_{m1}}{Z_p} = \frac{3dtwY^E}{4L_d}. \tag{2.34}$$

Note that the circuit element definitions (in terms of transducer material parameters and dimensions) were substituted into the middle expression to yield the expression on the right hand side.

To obtain an equation for blocked force with a current input, $\dot{u}$ is set to zero, and the second row of equation 2.30 is solved for $(\frac{f}{i})^{\dot{u}}$, resulting in

$$(\frac{f}{i})^{\dot{u}} = \frac{NR_{dc}Z_{m1}}{R_{dc}+Z_p} = \frac{3dt^2Y^E\rho_{dc}}{4L_dL_t(1+s\eta^T\rho_{dc})}. \tag{2.35}$$

If the force f in equation (2.30) is set to zero and an s-domain integration performed, the expression

$$(\frac{u}{v})^{f} = \frac{-NZ_{m1}}{sZ_p(Z_{m1}+Z_{m2})} = \frac{-3dL_d^2}{\frac{12\rho_mL_f^4}{\Gamma^4Y^E}s^2+t^2} \tag{2.36}$$

for the free deflection with a voltage input is obtained. The left hand term in the denominator accounts for the actuator inertia and can be ignored at frequencies well below the

first resonance, effectively setting the mass term Z_{m2} equal to zero. Below resonance, the expression for free deflection with a voltage input becomes

$$(\frac{u}{v})^f = \frac{-N}{sZ_p} = \frac{-3dL_d^2}{t^2}. \tag{2.37}$$

To model the actuator working against a load, a circuit element can be added to the mechanical terminals of the Figure 2.1 circuit and the circuit analysis revised accordingly.

2.3.2 Sensor Equations

Equation (2.30) can also be solved for relationships that describe the use of a polymer transducer as a sensor. In this case, either short-circuit charge (or current) or open-circuit voltage would be measured. Setting v in equation (2.30) to zero and solving for current over velocity yields the sensor equation

$$(\frac{i}{\dot{u}})^v = \frac{-NZ_{m1}}{Z_p} = \frac{-3dtwY^E}{4L_d}. \tag{2.38}$$

Integrating (dividing by the Laplace variable s) both the numerator and denominator shows that the same expression also applies to the short-circuit charge with a displacement input.

Another potentially useful sensor equation is found by setting i in equation (2.30) to zero and solving for the open-circuit voltage with a force input. The result is

$$(\frac{v}{f})^i = \frac{NR_{dc}Z_{m1}}{(Z_{m1}+Z_{m2})(R_{dc}+Z_p)}, \tag{2.39}$$

which yields a cumbersome expression once expressed in terms of geometry and the transducer parameters. If we assume operation at a frequency well below the first resonance, the inertial term Z_{m2} can be neglected. Furthermore, if we assume operation at a frequency above which the electrical impedance term Z_p becomes small relative to R_{dc}, the relation simplifies to

$$(\frac{v}{f})^i = N = \frac{3dL_d^2}{\eta^T L_t wt} \tag{2.40}$$

A third sensor relation involves measuring the open-circuit voltage resulting from a displacement input. Setting i in equation (2.30) to zero and solving for s times voltage over velocity yields

$$(\frac{v}{u})^i = \frac{sNR_{dc}Z_{m1}}{R_{dc}+Z_p} = \frac{s3dt^2Y\rho_{dc}}{4L_dL_t(1+s\eta\rho_{dc})} \tag{2.41}$$

To model a sensor driving an electrical load, such as a signal conditioning circuit, elements representing the load can be connected to the electrical terminals of the Figure 2.1 circuit

before performing the circuit analysis. An example of this technique appears in Chapter 5, where an ionic polymer sensor is used in a feedback control loop.

2.3.3 Impedances

Two additional relations that will be used later in this work are the electrical and mechanical impedances of the ionic polymer transducer. The electrical impedance with blocked boundary condition is calculated by setting $\dot{u}$ in equation (2.30) to zero and solving the first row of the equation for v/i, resulting in the expression

$$(\frac{v}{i})^{\dot{u}} = \frac{N^2 R_{dc} Z_{m1} + R_{dc} Z_p}{N^2 Z_{m1} + Z_p + R_{dc}}. \tag{2.42}$$

The electrical impedance with free boundary conditions is calculated by setting f in equation (2.30) to zero and solving the second row for $\dot{u}$. The result is substituted into the first row, and the equation is solved for v/i. The result is

$$(\frac{v}{i})^{f} = \frac{R_{dc}(N^2 Z_{m1} Z_{m2} + Z_p(Z_{m1} + Z_{m2}))}{N^2 Z_{m1} Z_{m2} + (Z_{m1} + Z_{m2})(R_{dc} + Zp)}. \tag{2.43}$$

When the assumptions in equations (2.31) and (2.32) are applied, equations (2.42) and (2.43) both reduce to

$$\frac{v}{i} = \frac{R_{dc} Z_p}{R_{dc} + Z_p}, \tag{2.44}$$

the parallel combination of R_{dc} and Z_p. Later in this work, experimental data that demonstrates that the electrical impedance is independent of the mechanical boundary conditions will be presented, validating the assumptions in equations (2.31) and (2.32).

The mechanical impedance, applied force over velocity, can be calculated with both short-circuit and open-circuit boundary conditions. Setting $i = 0$ in equation (2.30) and solving for $f/\dot{u}$ gives

$$(\frac{f}{\dot{u}})^{i} = \frac{(Z_{m1} + Z_{m2})(R_{dc} + Z_p) + N^2 Z_{m1} Z_{m2}}{N^2 Z_{m1} + R_{dc} + Z_p}, \tag{2.45}$$

the open-circuit mechanical impedance. Setting $v = 0$ in equation (2.30) and solving for $f/\dot{u}$ results in

$$(\frac{f}{\dot{u}})^{v} = \frac{N^2 Z_{m1} Z_{m2} + Z_p(Z_{m1} + Z_{m2})}{N^2 Z_{m1} + Z_p}, \tag{2.46}$$

the short-circuit mechanical impedance. Applying the assumptions in equations (2.31) and (2.32) to equations (2.45) and (2.46) gives

$$\frac{f}{\dot{u}} = Z_{m1} + Z_{m2}, \tag{2.47}$$

which shows that, providing equations (2.31) and (2.32) are valid, the mechanical impedance is independent of the electrical boundary conditions.

2.4 Discussion

The equations presented in this chapter are very similar to those commonly used to represent piezoelectric bimorphs. This similarity is expected, since both the equivalent circuit in Figure 2.1 and equation (2.22) appear in literature on piezoelectric materials. Some notable differences are as follows. First, the basic piezo-transducer parameters d_{ij} and ϵ^T are considered to be constant, real numbers (independent of frequency). Because of the complex nature of ionic polymer transducer response, the equivalent ionic polymer transducer parameters d and η^T are permitted to be frequency dependent. Also, the piezoelectric parameters are typically given subscripts that correspond to the direction of stress, strain, electric field, etc. relative to the poling direction of the piezoelectric material. In this work, we consider only bender transducers, so the electric field is always perpendicular to the induced strain, eliminating the need for subscripts. Another difference is that we have applied the second row of equation (2.22) at the surface of a bender transducer only as opposed to allowing it to apply to the entire transducer volume. As a result, T represents the surface stress, and d represents the electromechanical coupling at the bender surface, unlike the more general T and d_{31} applied to piezoelectric transducers. It is emphasized that the similarity between the equations presented in this work and those used to describe piezoelectric benders does not imply any correspondence in the underlying physics. Recall the physical models described in Chapter 1. The energy conversion between mechanical and electrical domains in ionic polymer transducers is believed to result from the redistribution of the free ions in the polymer. In contrast, the piezoelectric effect results from the relationship between electric polarization and mechanical stress in certain crystalline materials (Ikeda, 1996).

Because of the symmetry of the equation (2.30) coefficient matrix, each of the actuator equations has a corresponding sensor equation with the same Laplace-domain expression, except for the sign in certain cases. For example, the relationship between an applied voltage and the resulting free deflection is identical to the relationship between an applied force and the resulting short-circuit current. A sign change occurs when comparing

the equivalent force-voltage and current-velocity equations. The existence of these relationships is analogous to the reciprocity exhibited by linear electric circuits and by linear-elastic structures. In physical terms, they imply that the same mechanism is responsible for the energy conversion between mechanical and electrical domains, regardless of the direction of the conversion. The four related actuator and sensor expressions are

$$\left(\frac{i}{f}\right)^v = \left(\frac{\dot{u}}{v}\right)^f \qquad \left(\frac{v}{\dot{u}}\right)^i = \left(\frac{f}{i}\right)^{\dot{u}}$$
$$\left(\frac{i}{\dot{u}}\right)^v = -\left(\frac{f}{v}\right)^{\dot{u}} \qquad \left(\frac{v}{f}\right)^i = -\left(\frac{\dot{u}}{i}\right)^f \tag{2.48}$$

2.5 Chapter Summary

An equivalent-circuit model for ionic polymer transducers was presented. Unlike previous gray-box, dynamic models, the electromechanical coupling is bidirectional and is represented using a pair of linearly coupled equations. As a result, the model can be used to represent both sensing and actuation, and reciprocity exists between the electrical and mechanical domains. The circuit can be used as both a design tool and for evaluating performance of different ionic polymer transducer materials. It is hoped that the coupling term can eventually be derived from a physical model of the underlying mechanisms. Before the model can be used, material parameters must be identified, and the model must be validated, topics considered in the next chapter.

Chapter 3

Parameter Identification and Model Validation

To obtain quantitative information from the equivalent-circuit model presented in Chapter 2, one must first determine values for several material parameters. The fact that the underlying mechanisms responsible for ionic polymer transducer behavior have not yet been conclusively identified precludes an analytical approach to parameter estimation that is based only on well-understood, fundamental physics and known (or easily measured) material properties. To avoid this issue, an experimental approach is taken.

Significant variations in the performance of different transducers with similar dimensions have been observed. These variations have been attributed to inconsistencies in the manufacture of the base material as well as the plating process. To isolate the model-validation process from these issues, all of the model-parameter identification experiments were performed on the same ionic polymer transducer. Also, the validation experiments that are compared to simulated responses were performed using the same transducer used in the identification process. Until the manufacture of ionic polymer transducers becomes a more tightly controlled process, material parameters from one transducer should only be considered approximate for other transducers.

This chapter is organized in the following manner. First, the experiments used to identify material parameters and to validate the model are described. Next is a detailed description of the identification procedure for each parameter. Results that validate the model follow.

3.1 Experiment Description

A variety of experiments were performed to identify material parameters and to validate the model. This section describes the methods and hardware used to generate the inputs applied to the ionic polymer transducers and to measure electrical and mechanical quantities of interest. These inputs and measurements will be referenced in later sections in this chapter. Unless otherwise specified, the ionic polymer transducers were clamped between a pair of gold electrodes. All experiments were performed in air, and deionized water was brushed on the transducers at approximately one minute intervals – frequently enough to keep the surface of the transducers wet. When not in use, the transducers were stored in deionized water.

Voltage inputs for the time-domain experiments were generated using a dSPACE DS1102 DSP, and random voltage inputs were generated by a Tektronix FFT analyzer with signal generator. Before being applied to the transducer, the voltage inputs were amplified using a Hewlett Packard power amplifier. Current inputs were applied using a transconductance amplifier, whose input signal was produced by either the dSPACE or the Tektronix.

The electrical current applied to the transducer was measured by placing a 0.1- resistor in series with the polymer, between one of the fixture electrodes and ground. The voltage across the resistor was amplified and measured using either the dSPACE or the Tektronix. The electrical current was calculated during post processing by dividing the voltage drop across the resistor by 0.1- . The applied voltage was measured directly using either the dSPACE or the Tektronix.

In an experiment used to verify the model's symmetry, the short-circuit charge was measured while the polymer was excited mechanically. This measurement was accomplished using an op-amp based charge amplifier, which converted short-circuit charge to a voltage signal. During postprocessing, the charge-amp output was divided by the complex gain of the amplifier circuit because the lower end of the frequency range of interest was near the corner frequency of the charge-amp circuit.

Some experiments involved mechanically driving the polymer transducer. Motion was imparted to the polymer using an APS Dynamics APS 113 long stroke shaker. A bracket with a wedge-shaped piece of phenolic (see Figure 3.1) was mounted to the shaker

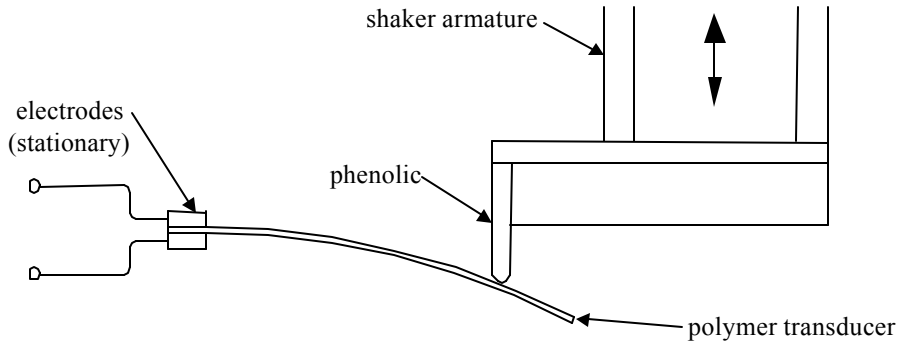

Figure 3.1: Mechanically driven polymer

armature to provide the interface between the transducer and the shaker. The position of the armature was measured using a Novotechnik T25 linear potentiometer and an appropriate signal conditioning circuit. Manufacturer's specifications indicate that the linear potentiometer repeatability is 0.002mm, and the linearity is 0.06mm. To assure that the armature displacement corresponded to the polymer displacement at the point of contact, the polymer was positioned relative to the shaker such that a preload was applied, and constant contact between the polymer transducer and the phenolic was maintained.

All force measurements in this work were made using a Transducer Techniques GSO-10 10 gram load cell with a TMO-1 signal conditioning circuit. The load cell precision, repeatability, and linearity were 0.05mN. The force measurement was also relatively noisy, with a typical noise level of 0.02mNrms. The force between the polymer transducer and the load cell sensing element was transferred through a nylon screw that was screwed into the tapped hole provided in the load cell sensing element. In some experiments, the polymer was positioned relative to the load cell such that there was a slight preload on the polymer. For time-domain analyses, this preload was subtracted out during postprocessing. The purpose of the preload was to allow 'negative' forces to be measured, which was especially important when an AC signal was applied to the transducer.

Two methods were used to obtain non-contact measurements of transducer displacement. For experiments that were analyzed in the frequency domain, a Polytec OFV-303 laser vibrometer head with OFV-3001 controller and OVD-20 demodulator was used, resulting in a position signal with a resolution of 5μm. Because the angle of the bender-transducer

surface changes with displacement, this method was limited to small displacements. Also, the electroded polymer surface was a poor target, and reliable tracking was difficult to achieve. Most observations of the polymer actuator's displacement were made using a Red-Lake PCI 2000 high speed digital video camera. The camera is capable of frame rates up to 2000Hz; however, only 8 sec. of continuous data can be recorded at this rate. A frame rate of 125Hz was used for the experiments reported in this work – a rate fast enough to capture the polymer motion, but slow enough to allow recording of up to 60 sec. of continuous data. A small 'dot' of correction fluid (white-out), placed on the polymer edge, acted as a target for the Image Express MotionTrace image analysis software. During postprocessing, the MotionTrace software was used to create a time history of the target's position. Under ideal conditions, MotionTrace is capable of determining the target position with resolution on the order of tenths of a pixel. In the experiments reported in this work, one pixel corresponded to approximately 0.1 to 0.2mm. The resolution achieved in a particular experiment depends on many factors, such as lighting, target size and shape, and lens quality. Though its resolution was limited compared to the laser vibrometer, the video camera and motion analysis software provided a reliable means by which to measure large transducer displacements.

Diagrams for the circuits mentioned in this section are provided in Appendix A.

3.2 Validation of Impedance Assumptions

This section presents data that validates the assumptions in equations (2.31) and (2.32). Figure 3.2 shows a plot of the measured frequency-domain electrical impedance and time-domain electrical response of a ionic polymer transducer (w=5mm, L_t=20mm, L_{free}=15mm, L_d=13mm) with both free and blocked boundary conditions. The plots corresponding to the two boundary conditions are identical, which matches the analytical result derived in section 2.3.3.

To see that the experimental results in Figure 3.2 show that the equation (2.31) and (2.32) assumptions are true, consider the following argument. Analysis of the Figure 2.1 circuit for both blocked ($\dot{u} = 0$) and free ($f = 0$) mechanical boundary conditions yields the following expressions for the impedance seen at the electrical terminals

$$(\frac{v}{i})^{\dot{u}} = R_{dc} \parallel (Z_p + N^2 Z_{m1}) \text{ and } (\frac{v}{i})^{f} = R_{dc} \parallel (Z_p + N^2 (Z_{m1} \parallel Z_{m2})), \qquad (3.1)$$

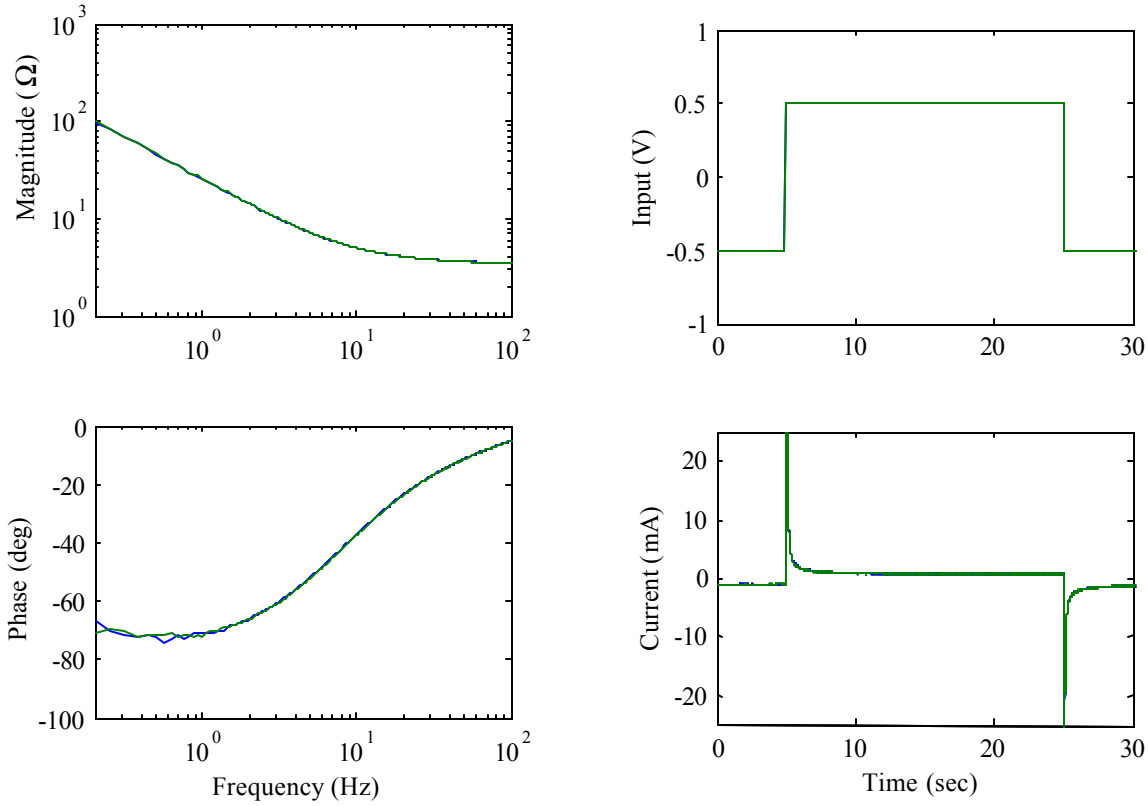

Figure 3.2: Electrical response with free and blocked boundary conditions: a) frequency-domain impedance, b) time-domain current response with a voltage input

where the symbol $\|$ indicates parallel circuit elements, whose equivalent impedance is the inverse of the sum of the inverses of the individual impedances. Providing that the following three conditions are met, the only way the expressions in equation (3.1) can become equivalent to one another is if the assumptions in equations (2.31) and (2.32) are true, resulting in

$$\frac{v}{i} = R_{dc} \parallel Z_p. \tag{3.2}$$

The first condition is that the polymer stiffness term Z_{m1} is non-zero. Second, R_{dc} must be on the same order as or greater than Z_p. If R_{dc} was very small relative to Z_p, both expressions in equation (3.1) would reduce to $\frac{v}{i} = R_{dc}$. The fact that the frequency-domain impedance plot in Figure 3.2 has a non-zero phase at some frequencies indicates that the

impedance is not purely real, as it would be if $\frac{v}{i} = R_{dc}$. Therefore, the second condition is met. The third condition is that the inertial term Z_{m2} must be small relative to the stiffness term over at least part of the frequency range examined. If this condition is not met, then $Z_{m1} \parallel Z_{m2} \simeq Z_{m1}$. This condition will satisfied for all frequencies well below the first resonance of the transducer, which was approximately 56Hz for the transducer used to generate the data for Figure 3.2.

Now that the equation (2.31) and (2.32) assumptions are justified, the simplified expressions developed in section 2.3 can be used with confidence. Also, since the electrical impedance does not depend on the mechanical boundary conditions, and the mechanical impedance is independent of the electrical boundary conditions, the superscripts on the parameters Y^E and η^T will be omitted.

3.3 Identification of Model Parameters

In general, the approach to parameter identification taken in this work was to consider the analytical expressions corresponding to several measurable input-output relationships and identify the expressions that are strongly affected by the term of interest but contain as few additional material parameters as possible. This approach allowed the material parameters to be isolated and then identified.

All the parameter identification experiments were performed on a the same ionic polymer transducer. The transducer dimensions were: t=0.2mm, w=5mm, L_t=33mm, L_{free}=25mm, and the distance L_d between the electrode (the clamped end) and driving point was 20mm.

One issue that hampered the parameter identification process as well as the model-validation process was the relatively inconsistent behavior exhibited by the polymer transducers. Figure 3.3 shows results of identical blocked force with voltage input experiments that were performed only minutes apart, without disturbing any of the hardware used in the experiment. While the current responses overlay very well, there are significant differences in portions of the blocked force. In one experiment, the transducer exerted a steady-state blocked force in the same direction as the initial force. In the other experiment, the opposite was true. With the polymer used in the identification process, the response with steady-state force in the opposite direction from the initial force was seen more frequently.

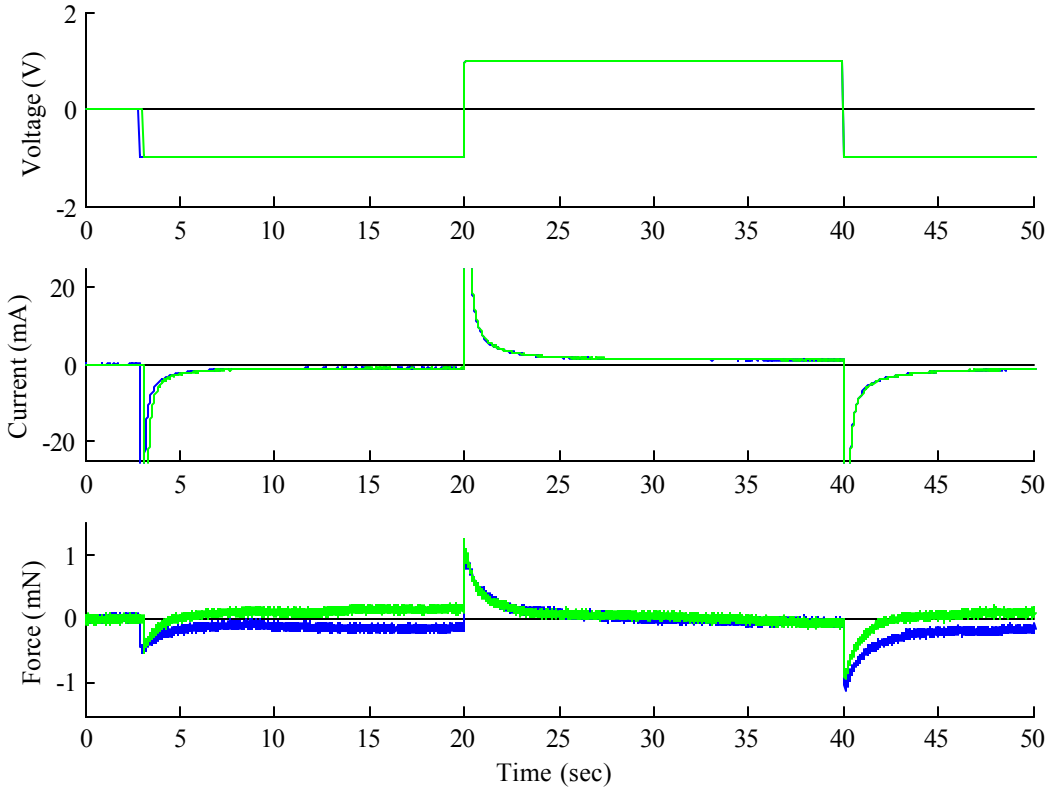

Figure 3.3: Blocked force with voltage input experiments that illustrate inconsistent polymer transducer behavior

Inconsistent behavior was less of an issue for the experiments that were analyzed in the frequency domain. The greater consistency seen in frequency-domain data may be due to the fact that data from a much greater period of time were averaged. Also, it is possible that transducer behavior is more consistent above approximately 1Hz.

3.3.1 Mechanical Terms

The mechanical parameters of the ionic polymer transducer are the static modulus Y_∞, the GHM parameters α, ζ, ω, and the density ρ_m. The density was determined by measuring the mass of the polymer transducer using a Mettler Toledo model AB204 precision balance, then dividing by the volume. Just before placing the transducer on the balance, any excess water present on the electrode surfaces was removed by gently patting the surface with a

paper towel. The mass of the transducer was 85mg, resulting in a density of 2.6E3 kg/m^3. Because the transducer was brushed with water to keep it hydrated during experiments, some water was present on the transducer surface during the experiments. The mass of the transducer, with as much water is it could hold on its surface was 121mg, a 42% increase over the mass with no water on the surface. The effective mass of the polymer during experiments was most likely between these two extreme values; however, unless one is considering an input-output relationship that is strongly affected by the density, any error that is introduced will be small.

The static modulus and the GHM parameters were determined using an experiment in which the load cell was mounted to the shaker armature. The transducer was given a displacement input using the shaker, and the required force was measured. To determine the static value of the elastic modulus Y_∞, a step displacement was imparted to the polymer by moving the shaker armature manually. The stiffness (force divided by deflection) versus time was measured and plotted. For a sample response, see Figure 3.4a. Little variation in the stiffness was seen after the displacement input, so the measured stiffness was assumed to correspond to the static modulus. Equation (2.5), the static relationship between force and deflection of a cantilevered beam, was used to convert the stiffness to a modulus, resulting in Y_∞=0.40GPa (corresponding to a stiffness of 0.5N/m).

To determine the GHM parameters, a random signal was applied to the shaker and the frequency response between the force measured by the load cell and the position was measured and recorded. A small preload was first applied to the transducer, so that it would not lose contact with the load cell during the motion.

It is common practice to mount a load cell between a shaker and the structure being excited in order to measure the force acting on the structure. Typically, the forces exerted on the structure are much higher than the inertial forces acting on the load cell sensing element, and the force measurement accurately represents the force exerted on the structure. This convenient relationship between exerted force and inertial forces acting on the load cell sensing element does not hold true in the experiment used to estimate the modulus and GHM parameters. This fact is illustrated in Figure 3.4b, where plots of the load cell response with no polymer in the fixture and with a polymer in the fixture are shown. Above approximately 2Hz, the 'accelerometer response' of the load cell becomes significant. To compensate for the fact that the load cell used also acts as an accelerometer,

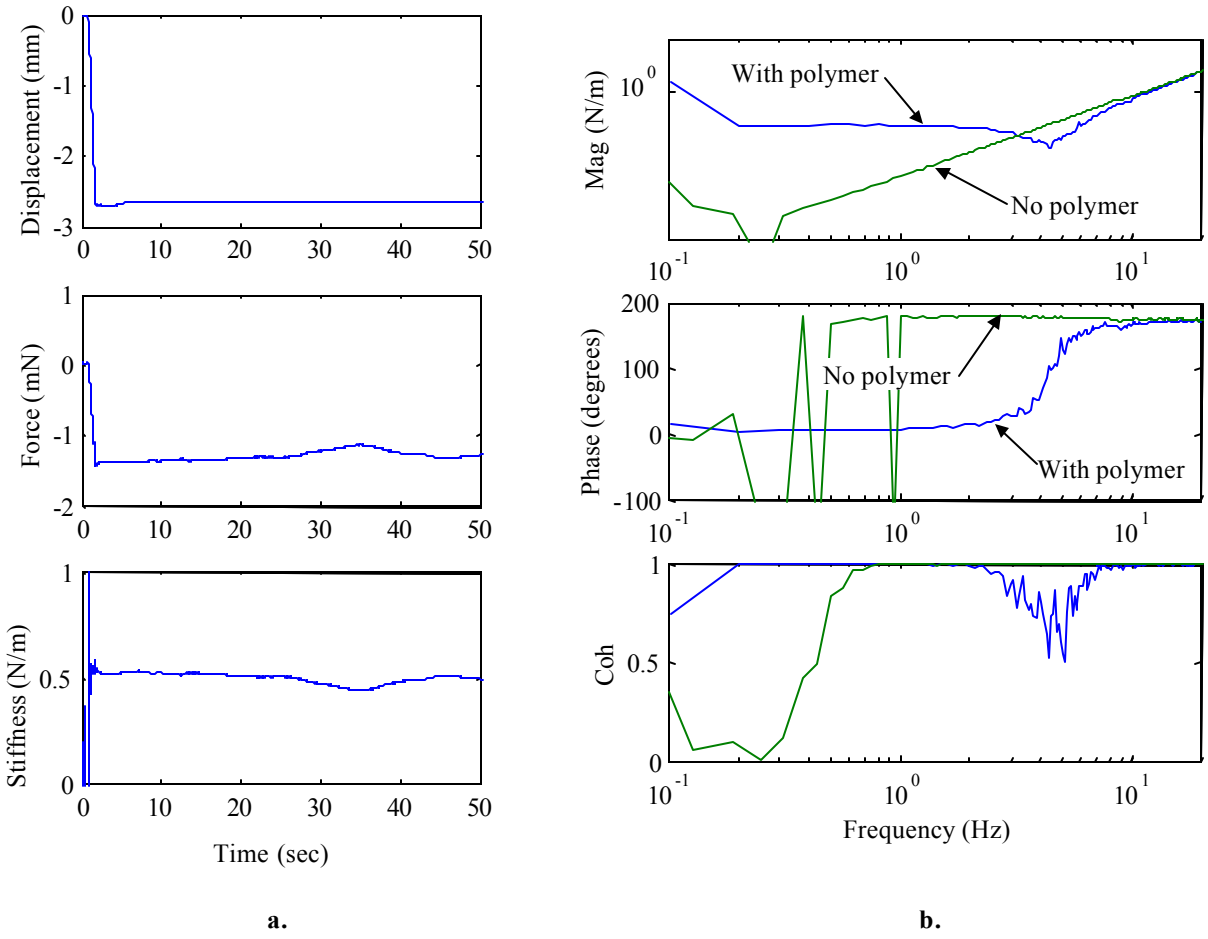

Figure 3.4: Responses from polymer transducer mechanical experiments: a) time-domain measurement with step displacement input, b) frequency-domain load cell response

postprocessing of the data was performed to remove the component of the measured force that did not correspond to the force exerted on the polymer bender.

The MATLAB constrained minimization routine *fmincon* was used to determine the GHM parameters α, ζ, and $\hat{\omega}$ by minimizing the error between the measured frequency-dependent stiffness (experimental data) and the stiffness corresponding to the frequency response of the modulus described by equation (2.10). Specifically, the error function that was minimized, denoted by Υ is

$$\Upsilon = \frac{1}{M}\sum_{i=1}^{M} \|k_{\text{pred}}(f_i) - k_{\text{meas}}(f_i)\|^2, \tag{3.3}$$

where the f_i represent the M discrete frequencies at which the stiffness was measured, and the subscripts 'pred' and 'meas' denote the predicted and measured values of the frequency

response.

The resulting parameters are α=5.2, ζ=0.68, and $\hat{\omega}$=2100. Note that the value of $\hat{\omega}$ is well beyond the frequency range of the experimental data. The measured polymer stiffness showed little frequency dependence, indicating that viscoelasticity is not significant in the 0-20Hz range – the ionic polymer acts predominantly like a linear-elastic material. With so little frequency dependence in the measured stiffness, accurate determination of the GHM parameters from the experiment described above cannot be expected. Once all of the model parameters were identified, a simulated free deflection over voltage frequency response was compared to a measured response. The displacement measurement was performed using the laser vibrometer, and the frequency range of the test included the first resonant frequency of the transducer. The GHM parameters were 'adjusted' to provide a good match between the simulated and measured damping of the first resonance. The resulting values, which are used in the remainder of this work, are α=2.2, ζ=0.6, and $\hat{\omega}$=2100. Because viscoelasticity is not significant in the frequency range considered in this work, the frequency-dependent modulus, modeled using the GHM method, amounts to little more than a convenient means through which to model the small amount of damping present in the transducer response. However, if the frequency range of the model is extended, the viscoelastic terms may become more important.

3.3.2 Electrical Terms

The electrical terms to be identified are the resistivity from equation (2.16) and the n resistivities and permittivities in equation (2.20). A combination of time and frequency-domain data was used to estimate values for these terms.

First, consider the DC response of the electrical side of the circuit shown in Figure 2.1. Because there is a capacitor in series with the resistor in each of the branches of the Z_p circuit, Z_p will not conduct current at DC. This fact can be shown by applying the Final Value Theorem (Franklin et al., 1994) to the inverse of the Laplace domain expression for Z_p in equation (2.19). The result, zero, represents the DC current conducted by Z_p with a constant voltage input. Because Z_p will not conduct DC current, the only circuit element that is related to the DC response of the left-hand side of the equivalent circuit is R_{dc}, whose value is determined by the material parameter ρ_{dc} and the transducer dimensions. To estimate ρ_{dc}, the current was measured while applying a step voltage to the transducer.

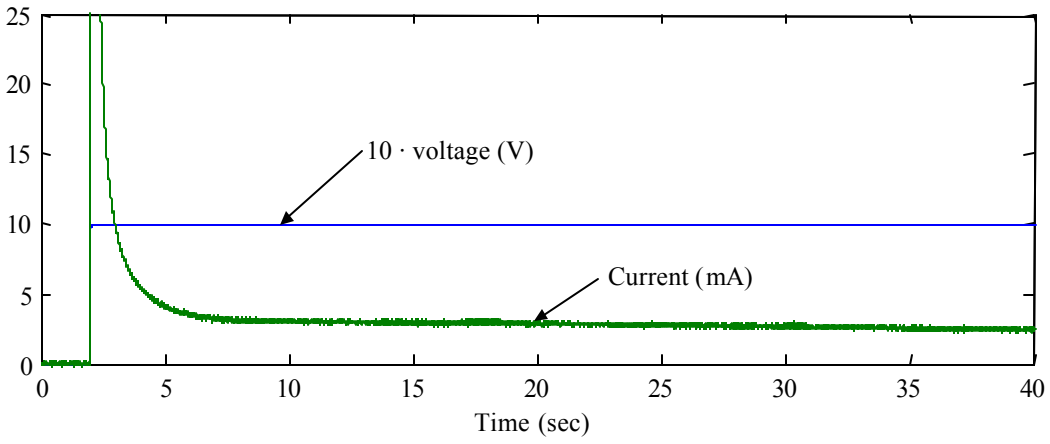

Figure 3.5: Current response with a voltage-step input – used to determine polymer transducer DC resistance.

A sample step response is shown in Figure 3.5. The step magnitude was divided by the steady-state current resulting in a value of 400- for R_{dc}. Using this value for the left-hand side of equation (2.16) and solving for ρ_{dc} gives $\rho_{dc} = 330$- ·m.

The values for the material parameters ρ_i and ϵ_i, which are needed to calculate Z_p were determined using the MATLAB constrained minimization routine *fmincon*. The constraints placed on the minimization were $\rho_i > 0$ and $\epsilon_i > 0$. The errors in the simulated voltage-step response, the simulated current-step response, and the simulated frequency response of the parallel combination of R_{dc} and Z_p were used in the function Υ that was minimized. The step responses were included in the identification process in order to capture the low-frequency dynamics of the transducer response, which are at frequencies below those that are practical to observe with frequency-domain methods. The error in the frequency response was multiplied by a frequency-dependent weighting function, so that the higher frequencies, where the impedance is relatively small, would not be ignored during the minimization. The relative weights of the step-response errors and the frequency response error were also adjusted.

Figure 3.6 contains a plot of the measured electrical impedance, the frequency-dependent weighting function used in the minimization, and the product of the weighting

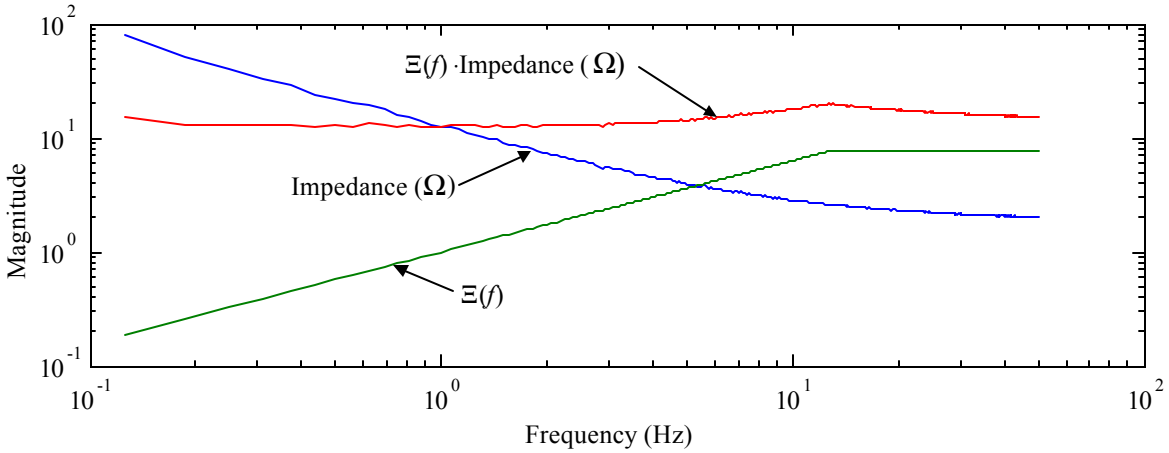

Figure 3.6: Weighting function used in minimization of frequency response prediction error.

function and the impedance. The weighting function is

$$\Xi(f_i) = \begin{cases} f_i^{0.8} \text{ for } f_i < 12.5 \\ \\ 12.5^{0.8} \text{ for } f_i > 12.5 \end{cases} \tag{3.4}$$

The prediction error to a voltage-step input was quantified using

$$e_1 = \sqrt{\frac{1}{M}\sum_{i=1}^{M}(x_{i,\text{pred}} - x_{i,\text{meas}})^2}. \tag{3.5}$$

where the x_i are the values of the current at the M discrete points in the experimental time history, and the subscripts 'pred' and 'meas' denote predicted and measured values. The prediction error to a current step, represented by $e2$, was determined in the same manner. The function that was minimized is

$$\Upsilon = w_1 e_1 + w_2 e_2 + w_3 \frac{1}{P}\sum_{i=1}^{P} \Xi(f_i)|Z_{\text{pred}}(f_i) - Z_{\text{meas}}(f_i)|, \tag{3.6}$$

where $Z(f_i)$ denotes the electrical impedance at frequency f_i, and w_1, w_2, and w_3 are scalars that can be adjusted to bias the fit towards either the step responses or the frequency-domain impedance measurement. Four resistivities and permittivities (to describe η) were required to obtain a reasonable fit to the experimental responses. Figure 3.7 contains plots of the experimental and predicted responses with w_1=100, w_2=0.5, and w_3=2 – the corresponding transducer parameters are given in Table 3.1. The inputs were a 1V voltage step, a 5mA

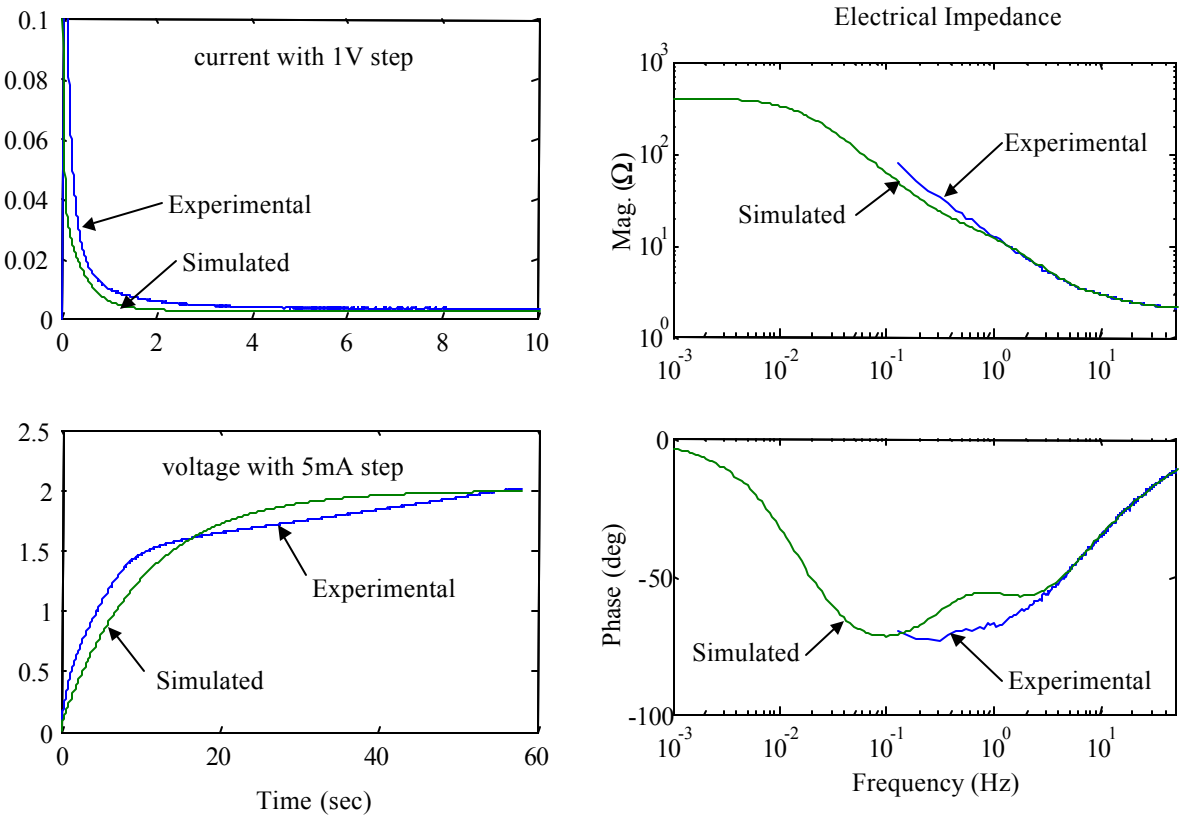

Figure 3.7: Simulated versus experimental electrical response with w_1=100, w_2=0.5, and w_3=2.

current step, and a 0.18Vrms 0-50Hz random input. The experimental frequency response is based on 15 averages of a 2048 point FFT with a sampling rate of 128Hz.

Several combinations of w_1, w_2, and w_3 were tried in attempts to obtain a better fit to the experimental data than that shown in Figure 3.7. It was found that an improvement in the step-response fits and a better fit the to frequency-domain data were mutually exclusive, indicating that the dynamics in the transducer response may be input level dependent. It is unlikely that the difficulty in fitting both the time and frequency-domain data is a result of experimental error, since the same signal conditioning circuits and test fixtures were used for all the experiments.

To validate the assumption that the polymer transducer electrodes are perfectly conductive, consider the frequency range in which the magnitude of the transducer's electrical

Table 3.1: Resistivities and permittivities for w_1=100, w_2=0.5, and w_3=2.

Permittivity (F/m)	ϵ_1	ϵ_2	ϵ_3	ϵ_4
	0.018	0 0084	0.0035	0.00040
Resistivity (- · m)	ρ_1	ρ_2	ρ_3	ρ_4
	32.8	4.24	3.0	11.2

impedance is lowest. It is in this range that the small surface resistance will introduce the greatest error. The electrical impedance frequency response plotted in Figure 3.7 shows that the transducer impedance is lowest at 50Hz, where it is approximately 2- and is almost purely resistive. To consider surface resistance effects, the transducer's electrical impedance, near 50Hz, is represented using the equivalent circuit shown in Figure 3.8, where each element represents 1mm of transducer length. This circuit is similar to the one used by Kanno

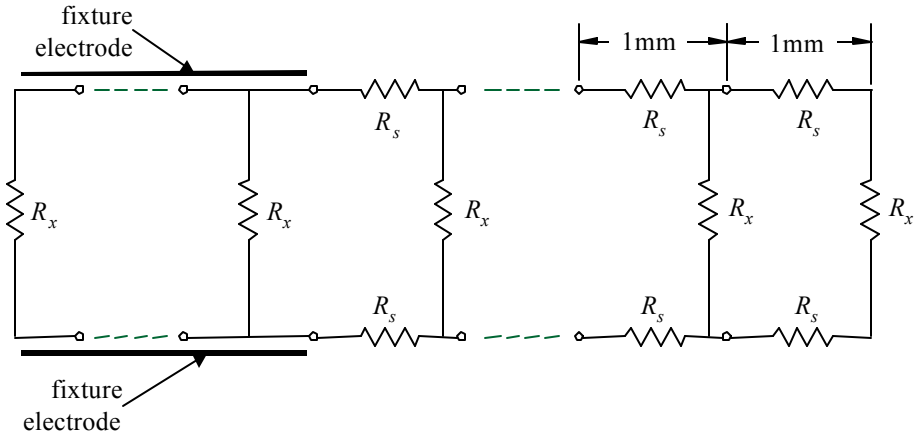

Figure 3.8: Equivalent circuit for anlyzing effects of non-zero surface resistance.

et al. (1996), only with the assumption that the operating frequency is high enough that any capacitors appear as shorts. The value of R_s was determined by placing one lead of a FLUKE multimeter at each end of the transducer and dividing the measured resistance by the total length (in mm), yielding a value of 0.054- . To calculate a value for R_x, the transducer's 2- impedance was multiplied by the total length, resulting in a value of $R_x = 66$- . If surface resistance is neglected ($R_s = 0$), the trasducer resistance is simply $R_x/33 = 2$- , the measured value. If surface resistance is included ($R_s \neq 0$), the transducer resistance is

$$\frac{1}{\sum_{m=1}^{M} \frac{1}{R_x} + \sum_{n=1}^{N} \frac{1}{2nR_s + R_x}}, \tag{3.7}$$

where M is the length (in mm) of the part of the transducer clamped between the electrodes, and N is the free length of the transducer (in mm). With non-zero surface resistance, the transducer resistance is 2.032- . If this value is considered correct, the percent error in the value obtained by ignoring the surface resistance is only 1.6%. At lower frequencies, where the transducer's impedance is higher, the error introduced by ignoring the surface resistance will be even smaller. Therefore, the assumption that the polymer electrodes have negligible resistance is justified.

3.3.3 Electromechanical Coupling Term

In Chapter 2, the transformer turns ratio N, which represents the electromechanical coupling, was interpreted as the relationship between open-circuit voltage and applied force. For this interpretation to apply, the transducer's DC resistance R_{dc} (400-) must be large relative to the impedance Z_p, so that the charge generated by the electromechanical coupling is not 'bled off' through R_{dc}. Inspection of the electrical impedance plot in Figure 3.7 reveals that the parallel combination of Z_p and R_{dc} is at least an order of magnitude less than the value of R_{dc} for approximately 0.1Hz and above. This order of magnitude ratio will not occur unless R_{dc} is very large relative to Z_p. Therefore, the physical interpretation for N, along with the ensuing derivation in terms of dimensions and material parameters, is valid for 0.1Hz and above.

The identification of the strain coefficient d is based on the expression for the blocked force exerted by the polymer transducer when excited by a voltage input. This experiment was chosen because it depends on only two material parameters, the modulus Y and the strain coefficient d. Because the blocked force is independent of the other material parameters, the identification of the d parameter can only be affected by inaccuracies in the identification of the modulus – it will be not be affected by errors in any of the other material parameters.

The blocked force expression, derived in section 2.3.1 is

$$(\frac{f}{v})^{\dot{u}} = \frac{3dtwY}{4L_d}. \tag{3.8}$$

As with the terms responsible for the dynamics of the electrical impedance, a combination of time and frequency-domain data was used in the identification process. Both the force produced by a 1V step input and the force produced by a 0-20Hz 0.61Vrms random input

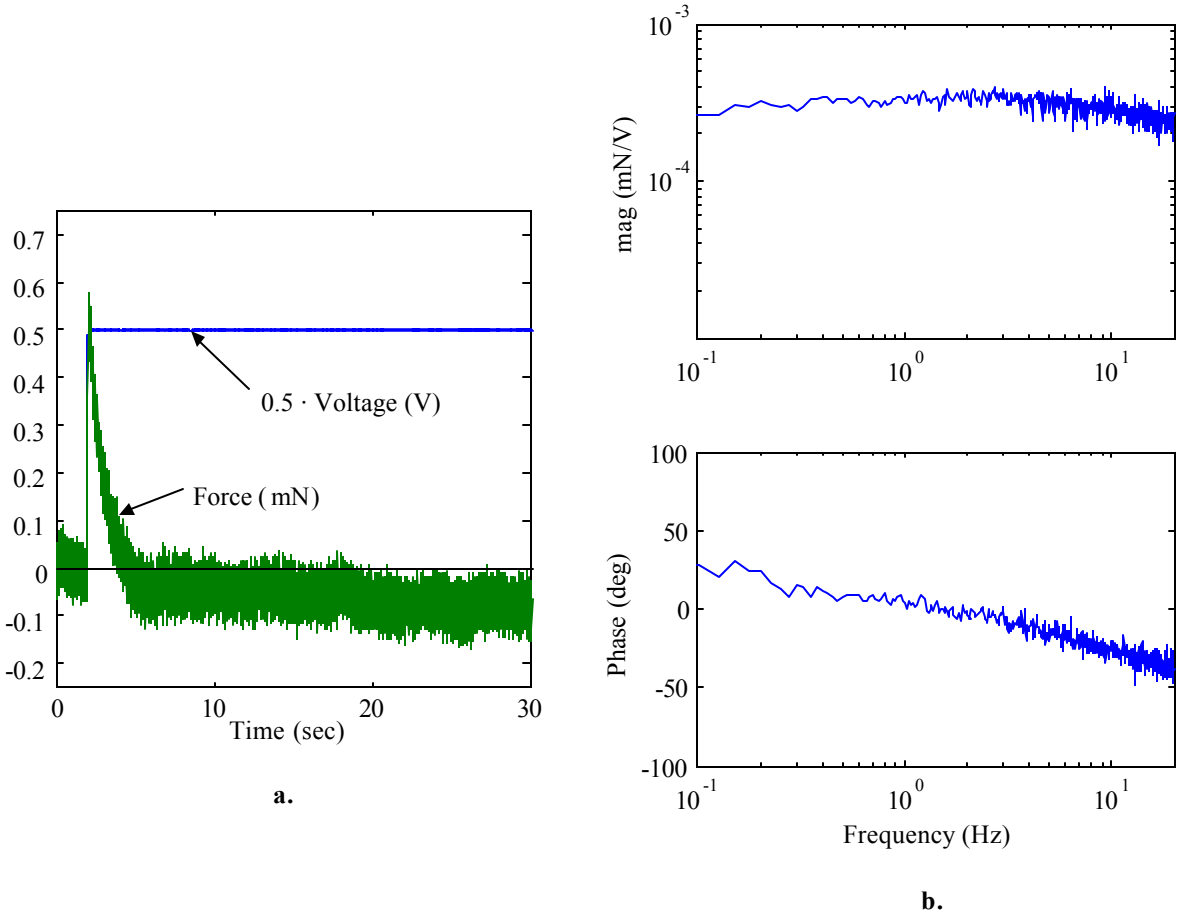

Figure 3.9: Blocked force with voltage input: a) step response, b) frequency response.

were considered. The frequency-domain data is based on 10 averages of a 2048 point FFT performed on data sampled at 51.2Hz.

To help determine the nature of the function used to represent d, the blocked force step response, an example of which is shown in Figure 3.9a, was analyzed. One important response feature is that the initial force and the DC gain have opposite signs. By the following argument, this feature leads to the conclusion that d is nonminimum phase. Consider modeling the response to a step with magnitude V_s using an expression with a single time constant, such as

$$f = V_s(-A + Be^{-b\tau})1(\tau) \text{ with } B > A, \tag{3.9}$$

where A, B, and b are positive scalars, τ represents time, and $1(\tau)$ is the unit step function. This expression will have a positive initial response of $V_s(B-A)$ and a DC value of $-V_sA$.

Transforming equation (3.9) to the Laplace domain and solving for the transfer function f/v gives

$$\frac{f}{v} = \frac{s(B-A) - Ab}{s+b}, \tag{3.10}$$

which has a pole at $-b$ and a zero at $\frac{Ab}{B-A}$. Since $B > A$, the zero is in the right half plane, and the expression in equation (3.10) is nonminimum phase.

Further insight can be gained by also considering the frequency-domain data for the blocked force, shown in Figure 3.9b. Above 2Hz, the phase starts to drop below 0 degrees. The phase of the single pole-zero combination in equation (3.10) will start at 180 degrees and end up at zero degrees, but it cannot produce a net phase change greater than 180 degrees. Therefore, additional terms will be necessary. Note that the additional phase lag cannot be accounted for by the frequency dependence of the modulus because the modulus adds phase lead to the blocked force transfer function.

The DC gain of the transfer function was first determined by examining the blocked force step response shown in Figure 3.9a and solving for the DC gain of d using equation (3.8). The MATLAB constrained minimization routine *fmincon* was used to estimate the poles and zeros of a transfer function for d. The constraints imposed were that one of the zeros is positive and that the remaining poles and zeros are negative. Equation (3.8) was used to predict the blocked force corresponding to d. The prediction error for the step response was quantified using

$$e_1 = \sqrt{\frac{1}{M}\sum_{i=1}^{M}(x_{i,\text{pred}} - x_{i,\text{meas}})^2}, \tag{3.11}$$

where the x_i are the force values at the M discrete points in time, and the subscripts 'pred' and 'meas' denote predicted and measured values. The function that was minimized is

$$\Upsilon = w_1 e_1 + w_2 \sqrt{\frac{1}{P}\sum_{i=1}^{P}|F_{\text{pred}}(f_i) - F_{\text{meas}}(f_i)|^2}, \tag{3.12}$$

where $F(f_i)$ denotes the blocked force per volt at frequency f_i, and w_1 and w_2 are scalars that can be adjusted to bias the fit towards either the step response or the frequency-domain measurement. A transfer function with three zeros and four poles gave a reasonable fit to both the step response and the frequency-domain data. A comparison of the experimental and simulated responses is shown in Figure 3.10 with w_1=5 and w_2=1.

As with the identification process for the electrical parameters, it was not possible to obtain a 'good' fit to both the step response and the frequency-domain data. If the fit was

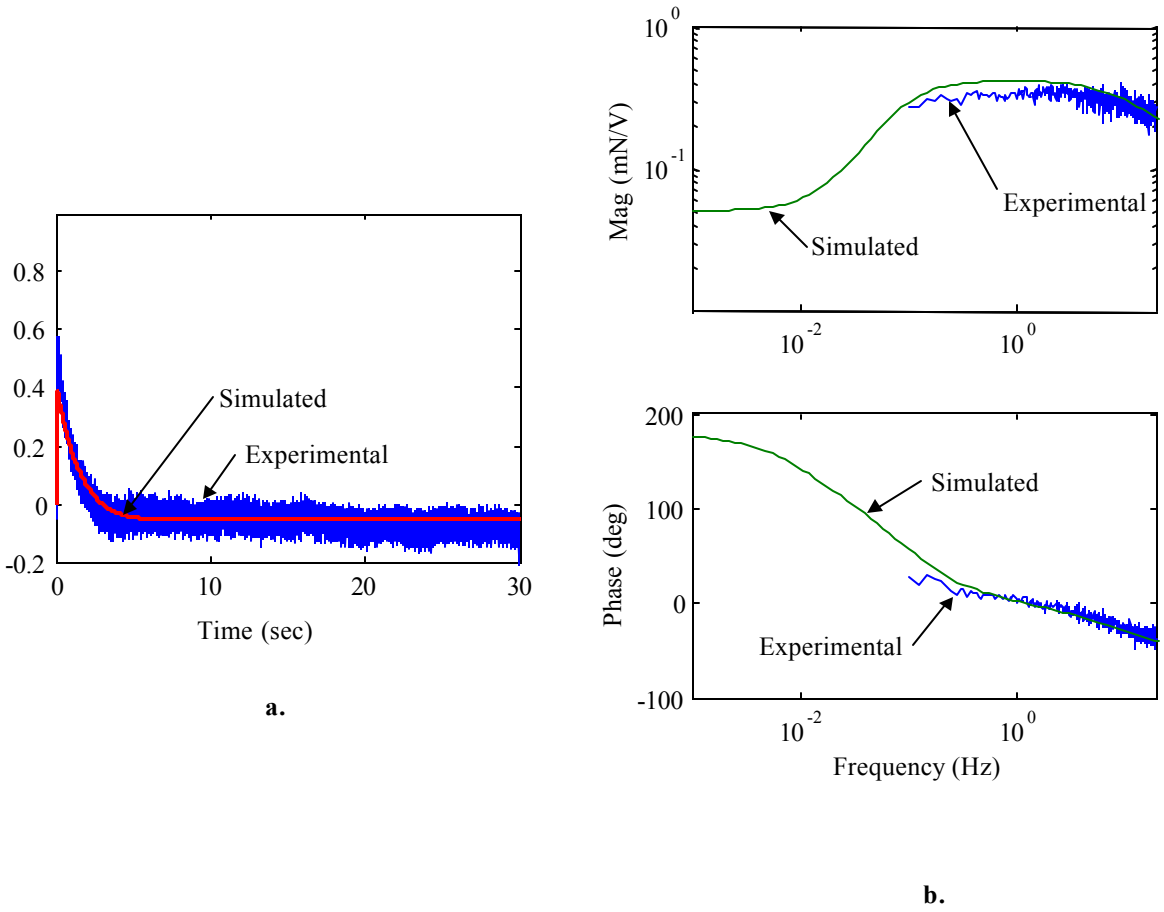

Figure 3.10: Simulated and experimental blocked force with voltage input: a) step response, b) frequency response.

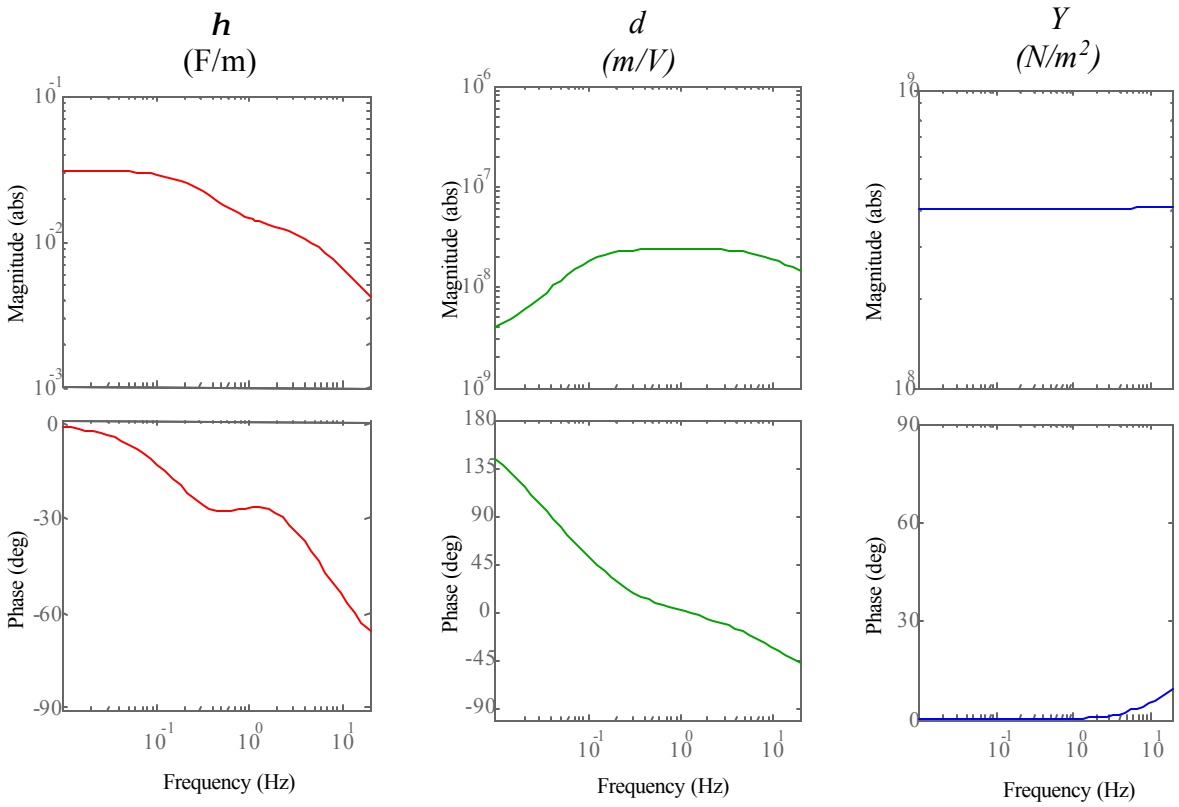

Figure 3.11: frequency-domain plot of the key frequency-dependent material parameters η, d, and Y

biased towards the frequency response, the peak value of the predicted step response was only 50% to 60% of the measured value. In the plot shown in Figure 3.10, the predicted peak of the step response is 72% of the measured value. This discrepancy is another indication that the material parameters may be dependent on excitation level.

Bode plots of the three key frequency-dependent material parameters, η, d, and Y over the frequency range 0.01Hz to 20Hz are shown in Figure 3.11. A brief summary of the more noteworthy features of each follows. The electrical term η, which replaces the permittivity in equation (2.22), represents the relationship between electric displacement and the applied electric field. The highest electric displacements will be achieved at very low frequencies, 0.1Hz and below. Above this range, the value of η starts to decrease (at less than one decade per decade), and the phase approaches -90 degrees, indicating that

the resistive elements in Figure 2.4 start to dominate the relationship between the electric displacement and the applied electric field. The strain coefficient d, plotted in Figure 3.11b, represents the electromechanical coupling in terms of the strain induced at the transducer surface when an electric field is applied perpendicular to the transducer. At very low frequencies, below 0.1Hz, the magnitude of the coupling term decreases with decreasing frequency, indicating that the ionic polymer transducers considered in this work will make poor sensors and actuators for quasi-static applications. The coupling term magnitude also decreases with increasing frequency above approximately 5Hz, though the slope is more gentle than the sub 0.1Hz slope. Also, the term exhibits significant phase lag. The complex modulus shown in Figure 3.11c is relatively flat across the 0.01-20Hz frequency range. The slight increase in magnitude along with a little phase lead reflects the small amount of damping that was observed in the free deflection over voltage frequency response. The fact that the modulus plot is relatively flat indicates that viscoelasticity is not important in the frequency range considered.

3.4 Model Validation

To validate the form of the model introduced in Chapter 2, as well as the material parameters identified in section 3.3, simulated responses will be compared to experimental responses from the same transducer that was used in the parameter identification process. The comparison will be made for input-output relationships that are different than those used for parameter identification. As a result, the comparison will validate the form of the model, as opposed to just confirming the quality of the identification process for a particular parameter. The symmetry in the model, which results from the presence of the transformer, will also be demonstrated experimentally. To confirm that the circuit parameters scale correctly with changes in transducer dimensions, the results of several experiments conducted with different size transducers will be presented. The results are scaled using the relationships in the analytical expressions for the various input-output relationships. These comparisons will also confirm that the material parameters used in this paper are, in fact, independent of transducer dimensions.

3.4.1 Model Form Verification

Figure 3.12 shows a frequency-domain comparison of experimental and simulated blocked force with a current input. The corresponding expression, in terms of transducer dimensions

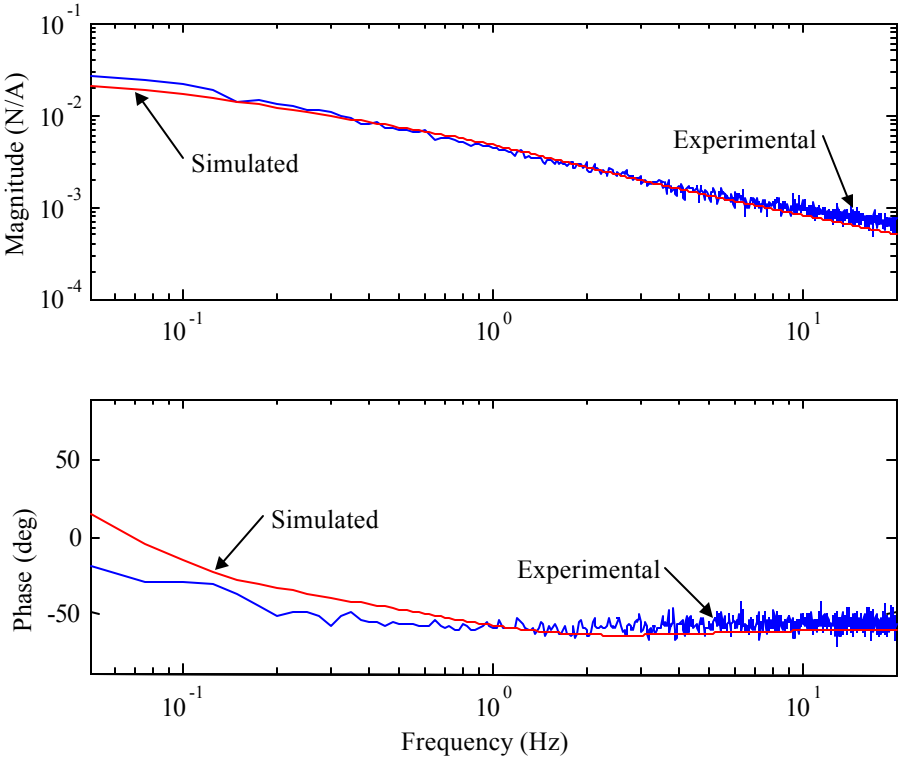

Figure 3.12: Comparison of simulated and experimental blocked force with a current input.

and material parameters (derived in section 2.3.1), is

$$(\frac{f}{i})^{\dot{u}} = \frac{NR_{dc}Z_{m1}}{R_{dc}+Z_p} = \frac{3dt^2Y\rho_{dc}}{4L_dL_t(1+s\eta\rho_{dc})}, \tag{3.13}$$

In this expression, unlike the relation for blocked force over voltage, which was used to identify d, the electrical terms ρ_{dc} and η appear. The plot in Figure 3.12 verifies the magnitudes of the electrical parameters ρ_{dc} and η relative to d. A comparison of experimental and simulated step response was not made for blocked force over current for the following reason. To avoid the changes in the nature of the response that appear to occur with higher

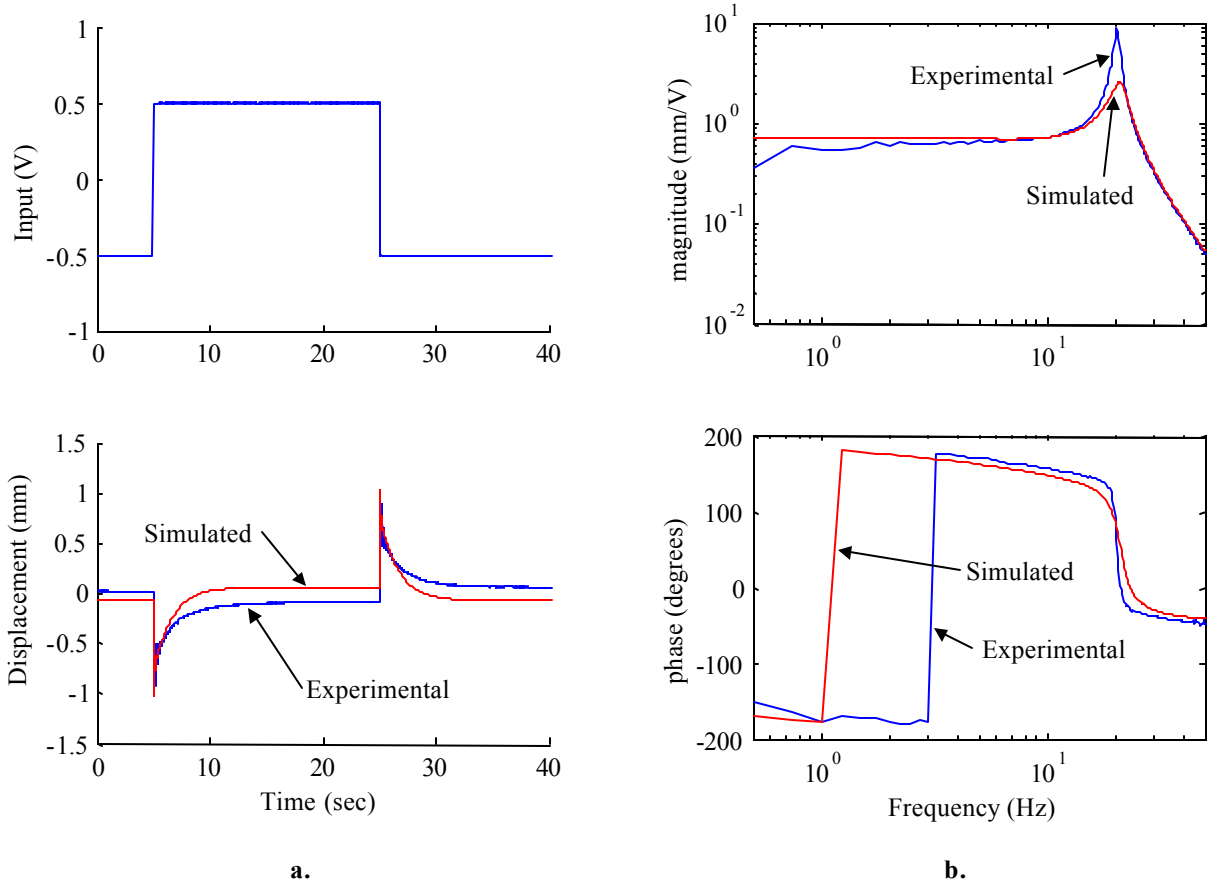

Figure 3.13: Comparison of simulated and experimental free deflection with a voltage input: a) square-wave response, b) frequency response.

input levels (above approximately 1.25V), input voltages were kept to 1V or less. Because of the high DC resistance of the polymer transducer (400-), this input level restriction would require a 2.5mA or smaller step. The peak forces generated by such a small current step (0.04mN predicted using the model) would be too small to measure with the 10g load cell.

To further validate the form of the model, experimental and simulated free deflection are plotted in Figure 3.13. The analytical expression (derived in section 2.3.1) is

$$(\frac{u}{v})^f = \frac{-NZ_{m1}}{sZ_p(Z_{m1}+Z_{m2})} = \frac{-3dL_d^2}{\frac{12\rho_m L_f^4}{\Gamma^4 Y}s^2+t^2}. \tag{3.14}$$

Note that this expression also includes the mass term Z_{m2} and will, therefore, have a resonance. The natural frequency of the transducer is predicted accurately, but the simulated

response is more heavily damped than the experimental response. This is another indication that the model would benefit from a better experiment for determining the mechanical material parameters. Besides the damping, the predicted results compare well to experimental data in the frequency domain. A time-domain comparison is made using a 0.025Hz 0.5V square-wave input. A square wave was used instead of a step input to avoid the permanent deformation (a topic discussed in detail later in this work) that sometimes accompanies a DC input. As long as the frequency of the square wave is low relative to the dynamics in the system response, the shape of the response will be identical to that of repeated step inputs of opposite sign. Therefore, the time-domain response comparison with a low-frequency square-wave input provides a means by which to examine the dynamics that are at frequencies below those included in the frequency-domain data. The model slightly underpredicts the response peak, which corresponds to the overpredicted damping seen in the frequency response. The dominant time constants of the relaxation phase of the response also match. The biggest discrepancy between the simulated and experimental responses is in the DC gain. In this experiment, the steady-state displacement of the transducer was in the same direction as the initial motion, unlike the blocked force with voltage input experiments used in the identification of the d parameter. This discrepancy, however, is not surprising given the inconsistencies sometimes observed in identical experiments (illustrated in Figure 3.3).

Because the electromechanical coupling is modeled using a transformer (in the equivalent circuit in Figure 2.1), some of the actuator and sensor equations are identical, with the exception of the sign in some cases. One pair of these 'reciprocal relations' is blocked force with a current input $(\frac{f}{i})^{\dot{u}}$ and open-circuit voltage with a velocity input $(\frac{v}{\dot{u}})^{i}$. Another pair is blocked force with a voltage input $(\frac{f}{v})^{\dot{u}}$ and short-circuit charge with a displacement input $(\frac{q}{u})^{v}$. Figure 3.14 contains a comparison of experimental data corresponding to $(\frac{f}{v})^{\dot{u}}$ and $(\frac{q}{u})^{v}$ for the same polymer on which the identification experiments were performed (t=0.2mm, w=5mm, L_t=33mm, L_{free}=25mm, L_d=20mm). The match is good, indicating that the bidirectional electromechanical coupling represented by the transformer is exhibited by ionic polymer bender transducers. The slight discrepancy in magnitude may be due to small errors in measuring the distance L_d. Neither the nylon screw through the load cell sensing element nor the phenolic wedge have sharp edges where they contact the transducer. For this reason, it is difficult to determine L_d with greater precision than approximately 1 mm.

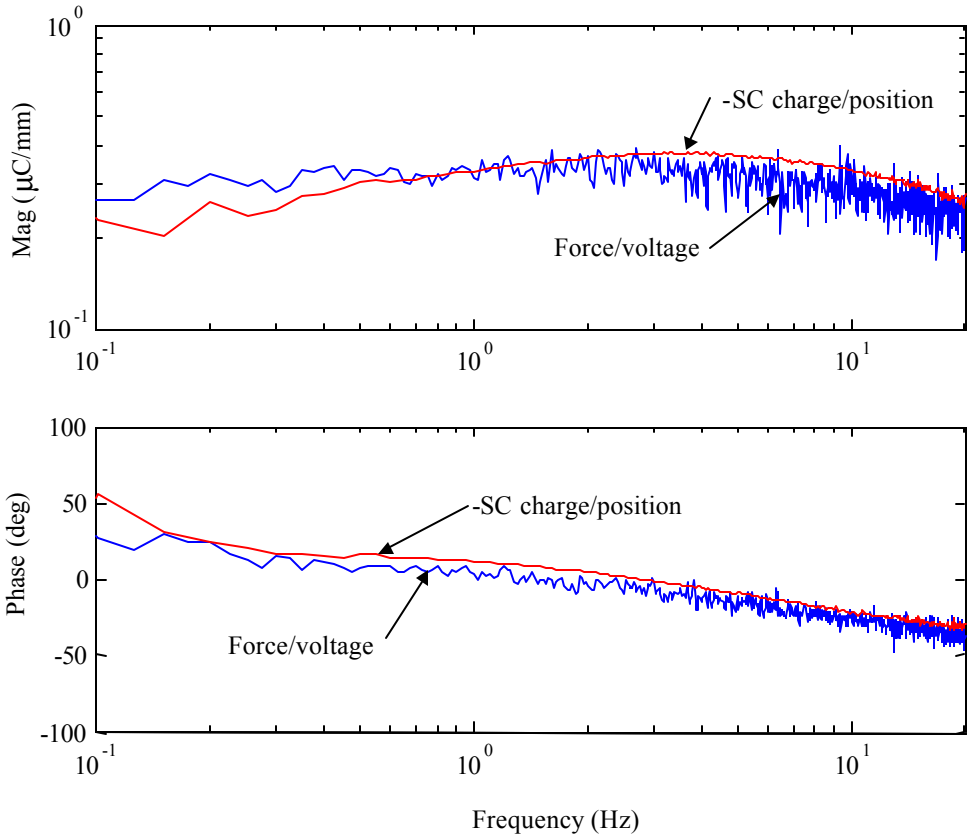

Figure 3.14: Comparison of blocked force with voltage input and open-circuit charge with displacement input.

3.4.2 Scaling Verification

To further verify the form of the model as well as the expressions derived for the circuit elements, several different experiments were repeated as transducer dimensions and/or L_d were varied. Recall that L_d is the distance between the electrodes (the clamped end of the cantilever) and the point at which force or deflection is measured. The results for each set of dimensions were then scaled to correspond to a single set of dimensions by multiplying by a constant. This constant was determined by the dimension(s) varied and the scaling law suggested by the appropriate input-output relation from Chapter 2. Sample transducers with different thicknesses were not available to the author, so no experiments verifying the scaling with respect to thickness are presented in this work.

In the interest of obtaining consistent experimental results, each experiment in a set

was performed on the same transducer with minimal changes to the experimental setup. It was necessary to use different polymers for different experiment sets because varying width w and total length L_t required cutting the transducer. For this reason, similar experiments performed on different transducers may not compare well when scaled to the same set of dimensions because of transducer to transducer variation. In other words, the material parameters sometimes vary from one transducer to another, an observation also made by other researchers.

In Figure 3.15a, plots of the blocked force with a voltage input for L_d=11mm, 13mm,

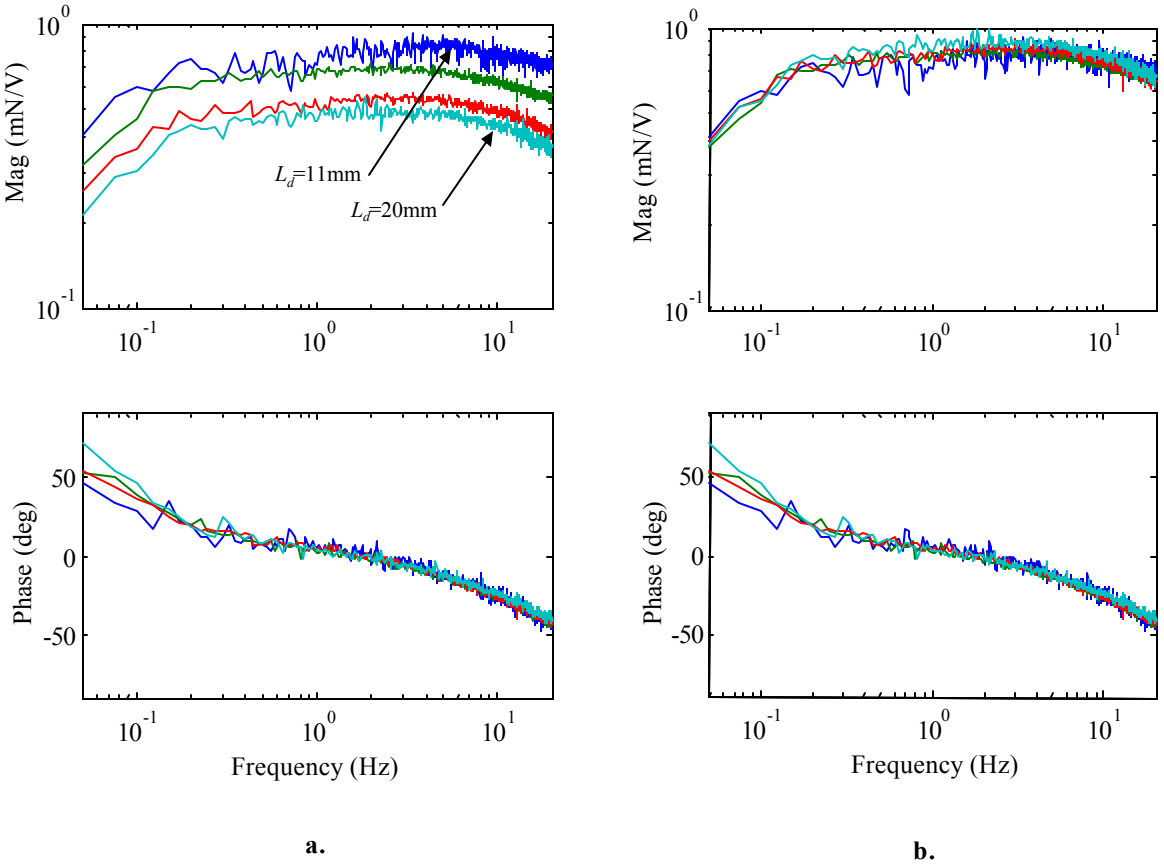

Figure 3.15: Scaling of blocked force with voltage input as L_d is varied from 20mm to 11mm: a)raw data, b)scaled to L_d=11mm

17mm, and 20mm are shown. The other transducer dimensions were w=4.5mm, L_t=33mm, and L_{free}=25mm, and they were not varied. The input was a 0-20Hz 1Vrms random signal, and each frequency response plot is based on five averages and 2048 point FFTs performed

on data sampled at 51.2Hz. Note that all the phase plots in Figure 3.15a match one another. Also, the vertical separation of the magnitude plots is essentially constant across the range of frequencies. This constant separation (with logarithmic horizontal and vertical axes) and the identical phase plots are indications that the plots are related through scalars. The expression for blocked force with a voltage input, derived in section 2.3.1 is

$$(\frac{f}{v})^{\dot{u}} = \frac{3dtwY}{4L_d}, \tag{3.15}$$

which predicts that blocked force with a voltage input is inversely proportional to L_d. Figure 3.15b contains plots of the same data shown in Figure 3.15a, except that each plot has been multiplied by $\frac{L_d}{11mm}$, so it can be directly compared to the data for L_d=11. The magnitude plots overlay quite well, confirming that the blocked force with a voltage input is inversely proportional to L_d, as predicted by equation (3.15).

In Figure 3.16a, the blocked force over voltage input frequency response is plotted for three values of transducer width, w=3mm, w=4.5mm, and w=6mm. The other transducer dimensions were L_t=33mm, L_d=17mm, and L_{free}=25mm, and they were held constant throughout the experiments. A 1Vrms 0-20Hz random input was applied to the transducer, and the frequency responses are based on five averages and 2048 point FFTs performed on data sampled at 51.2Hz. Examination of equation (3.15) indicates that the blocked force with voltage input will be proportional to w, so the Figure 3.16a data was scaled by $\frac{6mm}{w}$ to allow direct comparison to the data for w=6mm. The scaled data are plotted in Figure 3.16b. The phase plots match, and the magnitudes scale well, except that the w=6mm plot is low relative to the other plots for frequencies below 1Hz.

According to equation (3.15), blocked force over voltage is independent of the total polymer length L_t and the free polymer length L_{free}. To confirm this independence, we examine the results from an experiment in which L_t, L_d, and L_{free} were varied. The initial dimensions for the transducer were w=5mm, L_t=35mm, L_{free}=30mm, and L_d=28mm. Between experiments, the length of the polymer was reduced by first cutting a 7mm piece from its free end, then an 8mm piece. The input was a 0-100Hz 0.2Vrms random signal. The frequency responses are based on 10 averages and 4096 point FFTs of data sampled at 256Hz. Figure 3.17a shows the frequency responses prior to scaling. As with the previous data shown in this section, the phase plots match well. The Figure 3.17a data are multiplied by $\frac{L_d}{28mm}$ and replotted in Figure 3.17b for direct comparison. The scaled magnitude plots

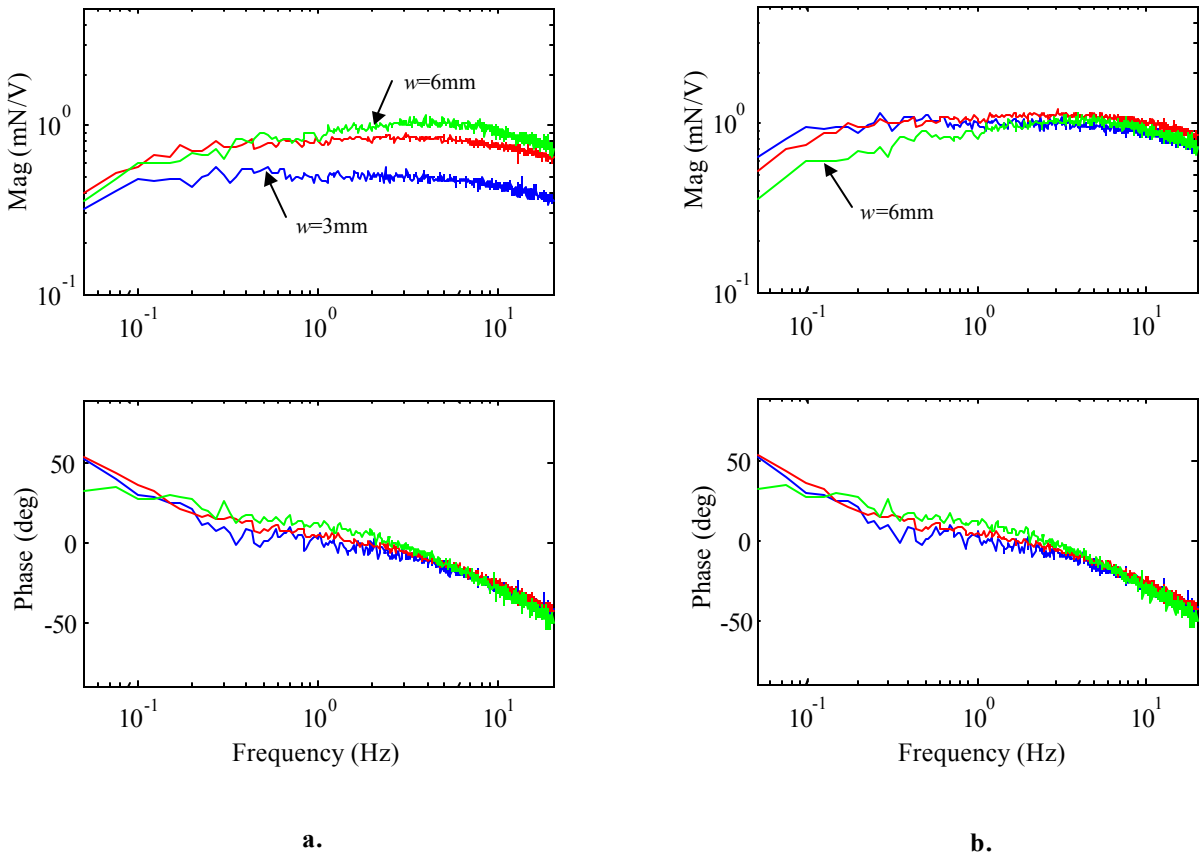

Figure 3.16: Scaling of blocked force with voltage input as w is varied from 6mm to 3mm: a)raw data, b)scaled to w=6mm

are close to one another but do not match as well as the scaled data from the previously described blocked force experiments. The data corresponding to the shortest polymers overlays very well, but the magnitudes for the two longest transducers are a little low.

The analytical expression for blocked force with a current input, based on the Chapter 2 model, is

$$(\frac{f}{i})^{\dot{u}} = \frac{3dt^2 Y^E \rho_{dc}}{4L_d L_t(1 + s\eta^T \rho_{dc})}. \tag{3.16}$$

First, the scaling of blocked force over current with changes in L_d is examined. Figure 3.18a contains plots of the blocked force over current frequency response for a transducer with dimensions w=4.5mm, L_t=33mm ,and L_{free}=25mm. The plots correspond to L_d=11mm, 13mm, 17mm, and 20mm. The input current was a 0-20Hz 28mArms signal, and each frequency response plot is based on five averages and 2048 point FFTs performed on data

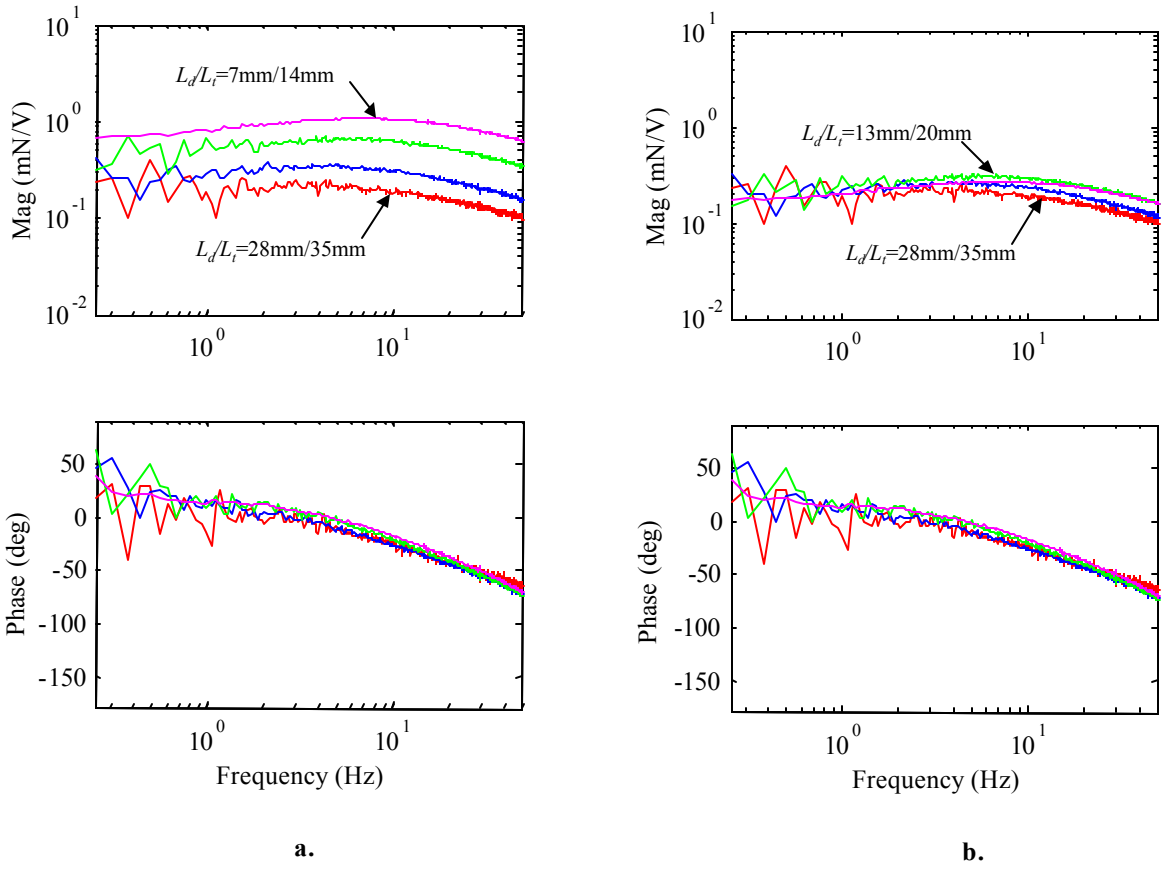

Figure 3.17: Scaling of blocked force with voltage input as L_d/L_t are varied from 28mm/35mm to 7mm/14mm, and : a)raw data, b)scaled to L_d/L_t=28mm/35mm

sampled at 51.2Hz. Figure 3.18b contains the same data, only the plots have each been scaled by $\frac{L_d}{11}$, so that they can be directly compared to the L_d=11 data. Both the magnitude and phase plots in Figure 3.18b match very well, confirming that blocked force with a current input is inversely proportional to the distance L_d.

Equation (3.16) indicates that blocked force over current is independent of transducer width. Figure 3.19 shows frequency response plots for a transducer with dimensions L_t=20mm, L_d=13mm, and L_{free}=15mm and widths w=3mm, w=4.5mm, and w=6mm. The inputs were 27mArms, 27mArms, and 23mArms 0-20Hz random signals. Again, the frequency response plots were based on 5 averages and 2048 point FFTs performed on data sampled at 51.2Hz. Both magnitude and frequency plots match well, with the only exception being that the w=4.5mm magnitude is slightly higher than the others below 1Hz.

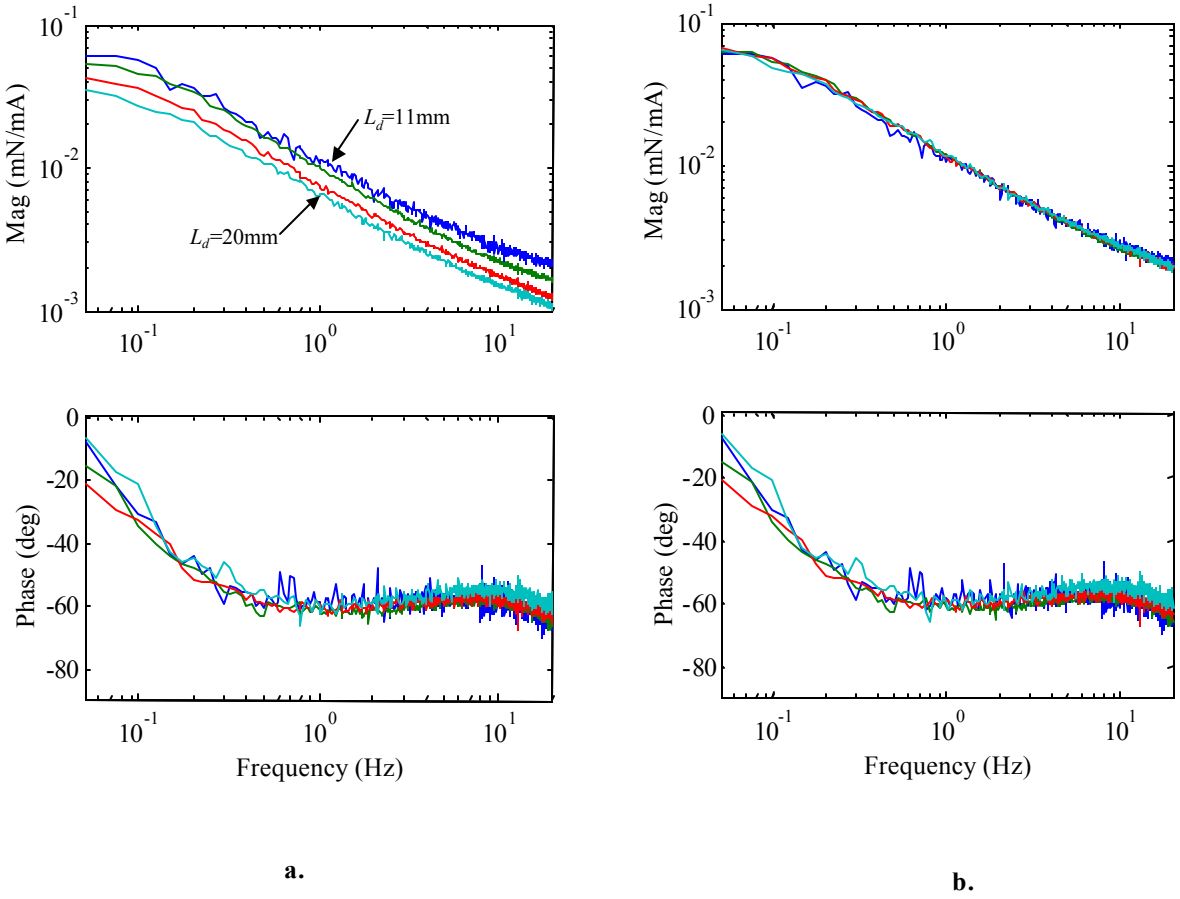

Figure 3.18: Scaling of blocked force with current input as L_d is varied from 20mm to 11mm: a)raw data, b)scaled to L_d=11mm

The good match confirms that blocked force with a current input is independent of the transducer width.

To verify the effect of changes in total polymer length L_t on blocked force over current, another set of measurements from a previously described experiment were used. The measured force and current from the set of experiments in which the length of a w=5mm polymer was reduced were used to calculate blocked force over current frequency responses. Figure 3.20a contains the plots corresponding to $L_t/L_{free}/L_d$=35/30/28mm, 28/23/21mm, 20/15/13mm, and 14/9/7mm. The input for each experiment was a 0-100Hz 0.2Vrms random signal, resulting in currents of 68.7mArms, 66.5mArms, 58.4mArms and 48.0mArms. The frequency responses are based on 10 averages and 4096 point FFTs of data sampled at 256Hz. Each of the plots in Figure 3.20a was multiplied by $\frac{L_t L d}{35mm \cdot 28mm}$

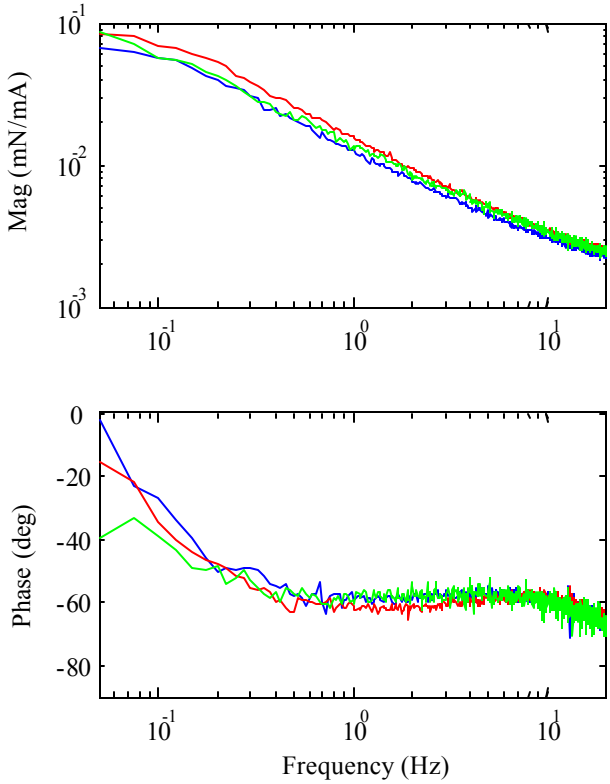

Figure 3.19: Scaling of blocked force with current input as w is varied from 6mm to 3mm.

for comparison to the $L_t/L_{free}/L_d$=35/30/28mm case. The scaled plots are shown in Figure 3.20b, and they overlay one another very closely. It is interesting to note that the plots in Figure 3.20b match more closely than those in Figure 3.17b, even though they are based on the same experiment – the only difference is in the choice of either current or voltage for the denominator in the frequency response calculation.

Now, the scaling of the electrical impedance is examined. An expression for the electrical impedance is obtained by combining equations (2.44), (2.16), and (2.20), resulting in

$$\frac{v}{i} = \frac{t}{L_t w} \frac{\rho_{dc}}{(1 + s\eta\rho_{dc})}, \tag{3.17}$$

which is inversely proportional to both the total transducer length L_t and the width w. Figure 3.21a contains plots of the electrical impedance for a polymer with L_t=33mm,

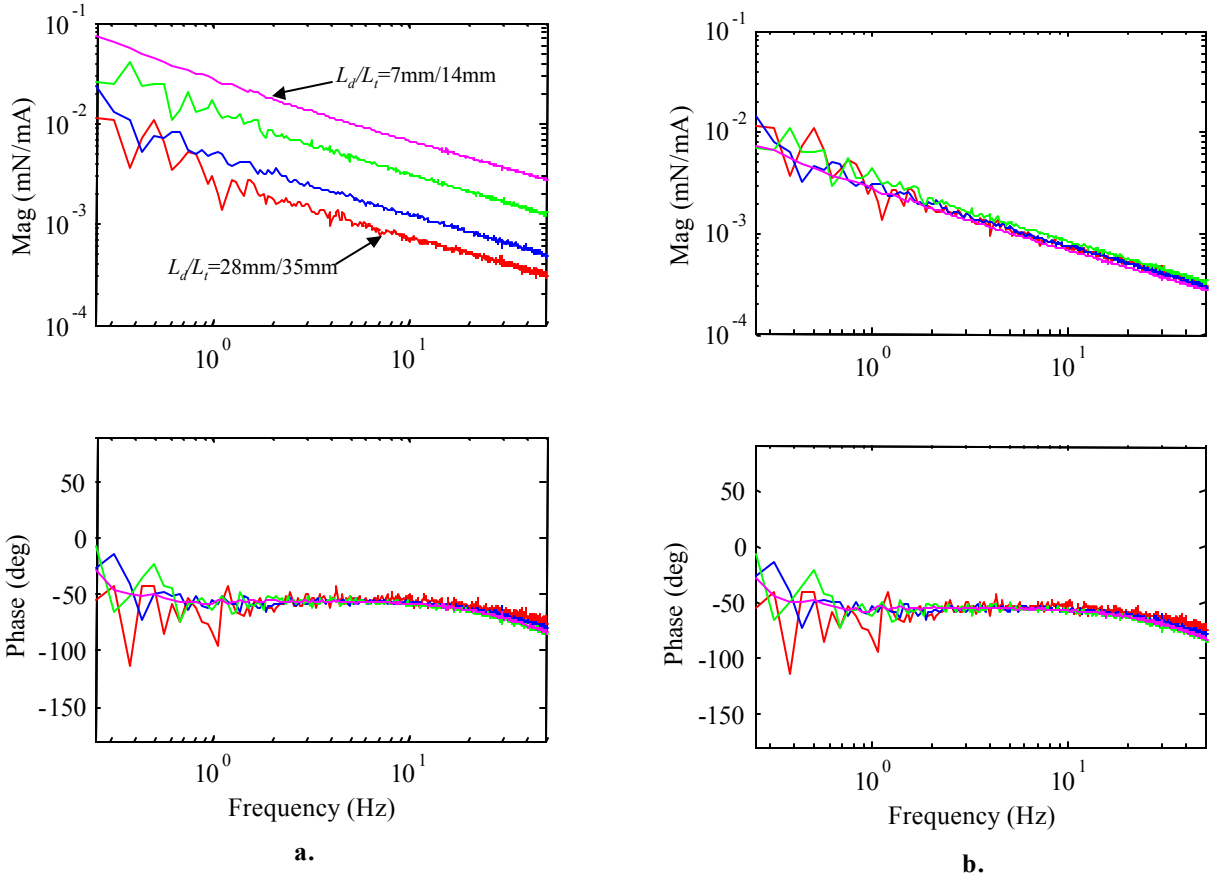

Figure 3.20: Scaling of blocked force with current input as L_d/L_t are varied from 28mm/35mm to 7mm/14mm, and : a)raw data, b)scaled to L_d/L_t=28mm/35mm

L_{free}=25mm, L_d=13mm, and widths w=3mm, 4.5mm, and 6mm. The inputs for this experiment were 0-20Hz 0.68, 0.48, and 0.57Vrms random signals (corresponding to w=3, 4.5, and 6mm). Note that the magnitude plots match quite well at very low frequencies, and the vertical distance between them gradually increases with frequency. This trend indicates that the variation in the relationship between voltage and current with changes in width is *not* a constant, as suggested by equation (3.17). To see whether or not the equation (3.17) scaling holds for any portion of the plotted frequency range , the Figure 3.21a data are replotted in Figure 3.21b after being multiplied by $\frac{w}{6\text{mm}}$. The scaled data match reasonably well at higher frequencies (above approximately 10Hz), suggesting that the relationship between electrical impedance and width described by equation (3.17) does apply to part of the frequency range considered.

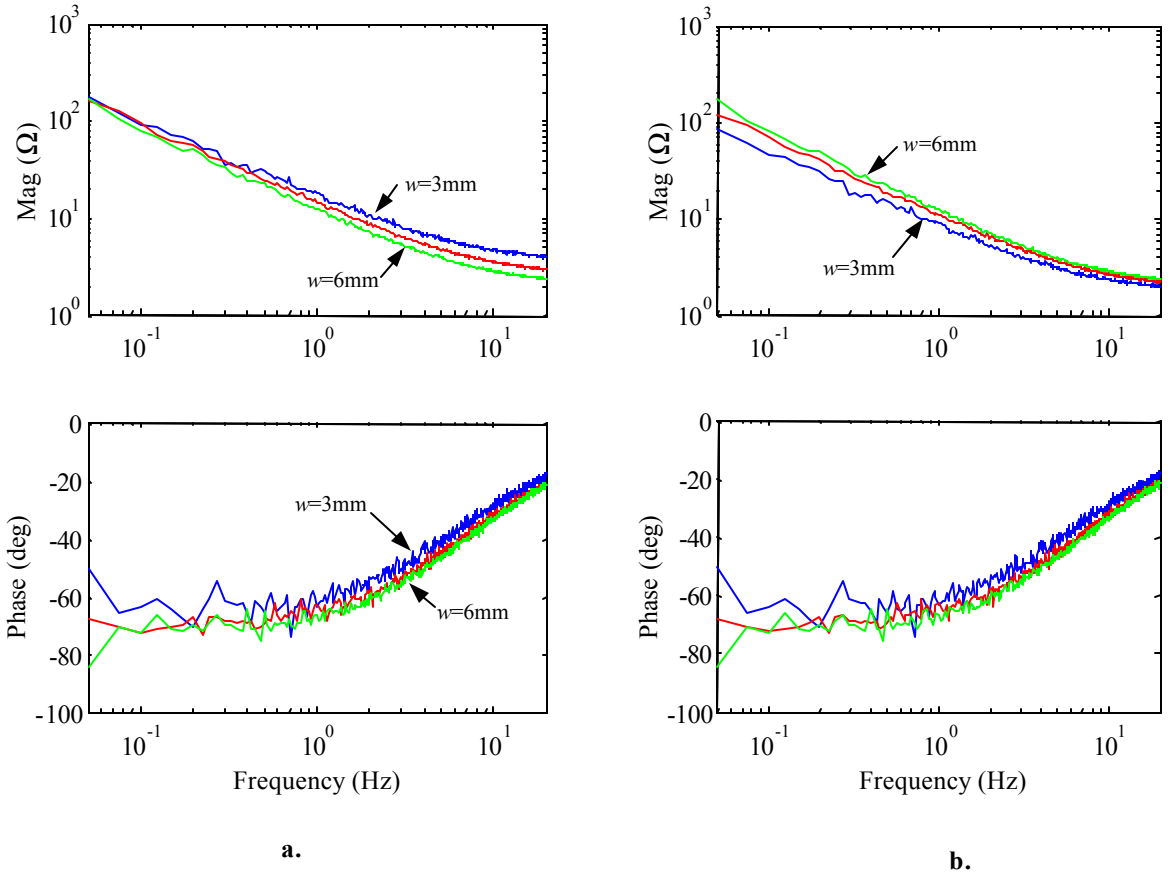

Figure 3.21: Scaling of electrical impedance as w is varied from 6mm to 3mm: a) raw data, b) scaled to w=6mm.

To explore the experimental relationship between electrical impedance and total transducer length L_t, the voltage over current frequency response, from the set of experiments in which the total polymer length was reduced, is examined. The electrical impedance plots corresponding to dimensions $L_t/L_{free}/L_d$=35/30/28mm, 28/23/21mm, 20/15/13mm, and 14/9/7mm are shown in Figure 3.22a. The input was a 0-100Hz 0.2Vrms random signal. As with the electrical impedance data presented in Figure 3.21, the vertical distance between plots varies with frequency. Also, the phase plots do not match for frequencies above 1Hz. The data are multiplied by $\frac{L_t}{35\text{mm}}$ and replotted in Figure 3.22b. At lower frequencies, approximately 2Hz and below, the data scales well – note this is also the frequency range in which the phase plots match.

In general, the results shown in Figures 3.21 and 3.22 indicate that the assumptions

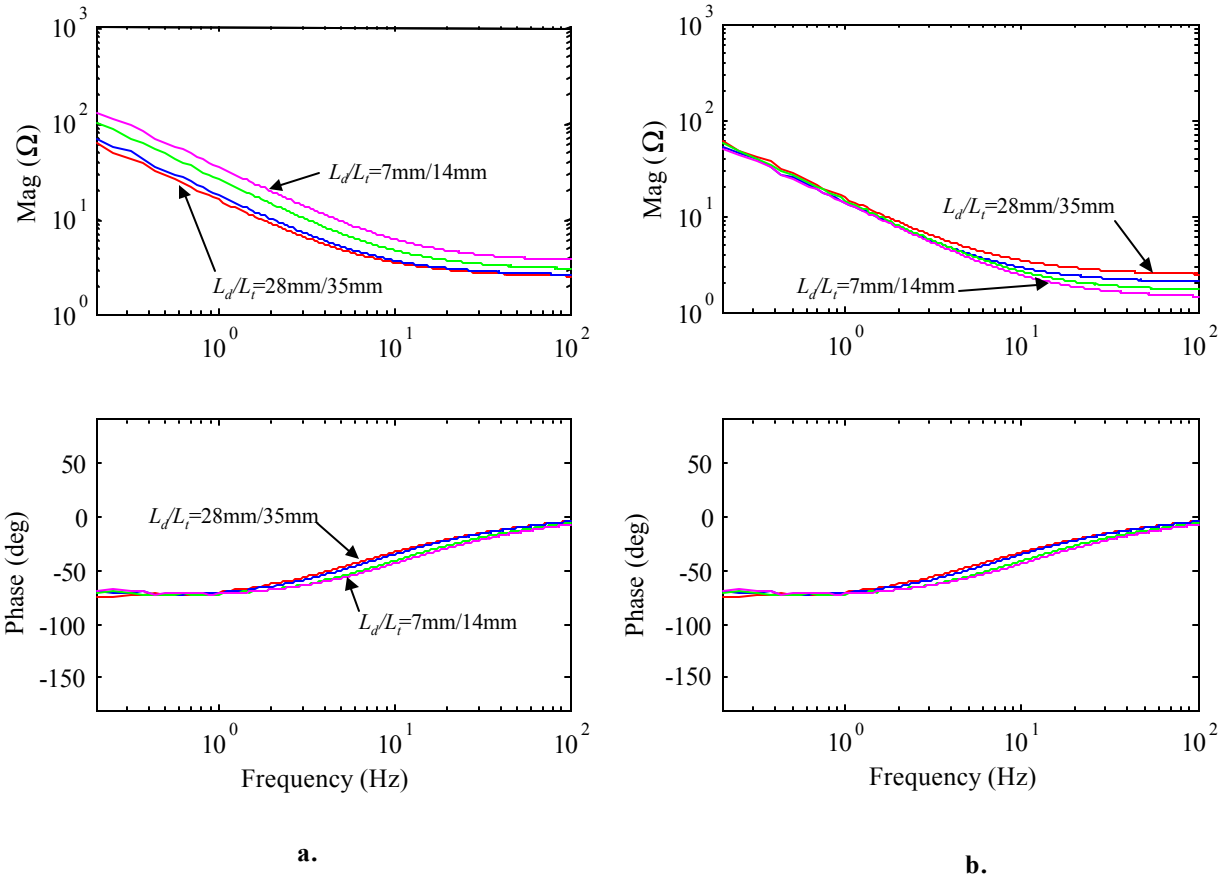

Figure 3.22: Scaling of electrical impedance as L_d/L_t are varied from 28mm/35mm to 7mm/14mm, and : a)raw data, b)scaled to L_d/L_t=28mm/35mm

made in Chapter 2, in the derivation of expressions for the circuit components R_{dc} and Z_p, are too simplistic to model an ionic polymer transducer's electrical impedance with great accuracy. However, the model does capture the basic nature of the electrical impedance, resistive at DC and at high frequencies (above 100Hz) and very capacitive at sub-Hz frequencies. The lack of accuracy in the electrical impedance modeling will not prevent the model presented in this work from being a useful tool for mechanical design and for most aspects of control-system design. For these tasks, accurate modeling of the electromechanical input-output relationships are of primary importance, and the scaling of several of these quantities has been shown to match the model quite well.

An interesting trend emerges if one groups the experimental data already presented in this section by the manner in which the transducer dimensions where altered. First,

consider the plots from the set of experiments in which the polymer transducer was shortened between experiments. Electrical impedance is shown in Figure 3.22, blocked force over voltage in Figure 3.17, and blocked force over current in Figure 3.20. Examination of the plots reveals that blocked force over current scales well, meaning that the scaling matches that predicted by the model, for the entire frequency range considered. However, blocked force over voltage only scales well in the low-frequency range, the same range in which the electrical impedance scales well. Next, examine the plots from the set of experiments in which the polymer width was decreased, Figures 3.21, 3.16, and 3.19. Again, blocked force over current scales well over the entire frequency range, but blocked force over voltage scales well only in the same frequency range in which the electrical impedance scales well, the higher end of the range considered. This trend suggests that the physical mechanism(s) responsible for the electromechanical coupling may be more closely related to current than to voltage.

3.5 Chapter Summary

The material parameters used in the equivalent-circuit model presented in Chapter 2 were experimentally identified. The model was validated by comparing simulated and experimental responses using the same transducer used in the identification experiments. A comparison of experimental blocked force with voltage input and short-circuit charge with displacement input confirmed that the reciprocity predicted by the model is, in fact, exhibited by ionic polymer transducers. In addition, the ability of the model to predict changes in performance as transducer dimensions are varied was experimentally verified.

Chapter 4

Transducer Characterization

The transducer model, which was presented in Chapter 2 and validated in Chapter 3, is used to describe the capabilities of ionic polymer sensors and actuators in quantitative terms. A comparison to piezoelectric transducers, a well known solid-state transducer technology, is provided for perspective. Because signal conditioning issues are sometimes crucial to the realization of predicted transducer sensitivities, they too are discussed. This chapter is concluded with an experimental investigation of an actuation phenomenon called 'electrically induced permanent strain.'

4.1 Ionic Polymer Actuators

To thoroughly evaluate the capabilities of an actuator technology, several performance metrics should be considered. These quantities provide a convenient means through which a designer can assess the suitability of the actuator technologies under consideration for a given application. One such measure is the blocked force that an actuator is able to exert. Another useful quantity is the maximum deflection (stroke) it can produce. For applications where size and mass are important, the volumetric and gravimetric energy densities should also be considered. In this section, the capabilities of ionic polymer actuators will be described in terms of these metrics, and to put the values in perspective, they will be compared to those of other solid-state actuators, namely piezoceramics and piezopolymers. Piezo Systems, Inc. PZT-5H-S4 (Piezo Systems, 1998) is chosen as a representative piezoceramic material, and the material properties of polyvinylidene fluoride (PVDF) published by Measurement Specialties, Inc. (Measurement Specialties, 1999) will be considered typi-

cal for piezopolymers. The ionic polymer actuators considered in this work are Nafion 117 based actuators with Au electrodes and Li as the mobile cation. The samples were provided by Dr. Mohsen Shahinpoor at the University of New Mexico and Dr. Kwang Kim at University of Nevada-Reno.

Before proceeding with a description of ionic polymer actuators in terms of performance metrics, a comparison of some of their general characteristics and behaviors to those of piezoelectric materials is in order. Although they can both be viewed as induced-strain solid-state actuators, piezoelectric actuators are, in many respects, vastly different than ionic polymer actuators. First, the electric field that must be applied to induce significant strain is much higher for piezoelectrics. They can also withstand much higher fields before detrimental effects are observed. For PZT-5H-S4 the maximum electric field (60% of the initial depolarization field) is 0.3MV/m, and for PVDF it is 30MV/m. The maximum excitation for ionic polymer actuators is 1.23V if electrolysis is to be avoided; however, several researchers, including the author, regularly apply slightly higher voltages, usually no more 2V to 3V. In general, higher excitation levels lead to faster dehydration of the polymer actuators (when used in air), and voltages of approximately 10V or more will quickly damage the polymer actuators. The thickness of the polymer transducers considered in this work is approximately 0.2mm, so the maximum voltage of 1.23V corresponds to an electric field of 6.2kV/m – orders of magnitude lower than the maximum field for piezoelectric materials. A second manner in which ionic polymer actuators differ from piezoelectric actuators is that a single layer of piezoelectric material (with no substrate) will strain uniformly when an electric field is applied across its thickness – there is no bending. Two layers of piezoelectric materials must be bonded together to construct a bender. Sometimes a 'shim' or 'vane' is bonded in between the piezo layers. The orientation of the poling and applied electric field in the two layers is arranged such that, when a voltage is applied across the electrodes, one layer extends and the other layer contracts, resulting in a bending motion. An ionic polymer bender consists of a single layer only. Another difference between the two types of actuators is that the electromechanical coupling in piezoelectric materials is considered independent of frequency. For this reason, the blocked force and free deflection of a piezoelectric bender, operated will below the its natural frequency, does not depend on the operating frequency. As the results presented in this section will show, the same cannot be said for ionic polymer actuators.

4.1.1 Actuator Equations

The blocked force exerted by an ionic polymer actuator, in the cantilevered-bender configuration, can be predicted using the equivalent-circuit model developed in Chapter 2 along with the material parameters that were determined experimentally in Chapter 3. The expression for blocked force is

$$(\frac{f}{v})^{\dot{u}} = \frac{3dtwY}{4L_d}, \tag{4.1}$$

where t and w are the transducer thickness and width, L_d is the distance between the clamped end of the bender and the point at which the force is measured. The modulus is represented by Y, and d is the coefficient that represents the electromechanical coupling. One unusual characteristic of ionic polymer actuators is that, even well below the first natural frequency, their ability to generate force is heavily frequency dependent. The voltage-step response of the actuator consists of a relatively quick initial response, in which the peak value is reached in several milliseconds, followed by a slow relaxation over the next several seconds. Figure 4.1a shows the predicted blocked force with a 1V voltage step for an actuator with dimensions t=0.2mm, w=5mm, and L_d=17mm. The predicted blocked force frequency response for the same actuator is shown in Figure 4.1b. The equivalent-circuit model can also be used to predict the free deflection with a voltage input. If we assume operation well below the actuator's first natural frequency, the free deflection can be predicted using the expression

$$(\frac{u}{v})^{f} = \frac{-3dL_d^2}{t^2}. \tag{4.2}$$

Figures 4.1c and 4.1d contain plots of the free deflection with a 1V step input and the free deflection frequency response. As with the blocked force, the free deflection is heavily frequency dependent. It is clear from the both the step response plots that ionic polymer actuators have a very small DC response relative to their peak response when given a voltage-step input. In this work, the peak value of the step response will be quoted, unless frequency dependence is explicitly mentioned. Therefore, these quantities should be interpreted as 'best case,' with the understanding that they will not be achievable at some frequencies.

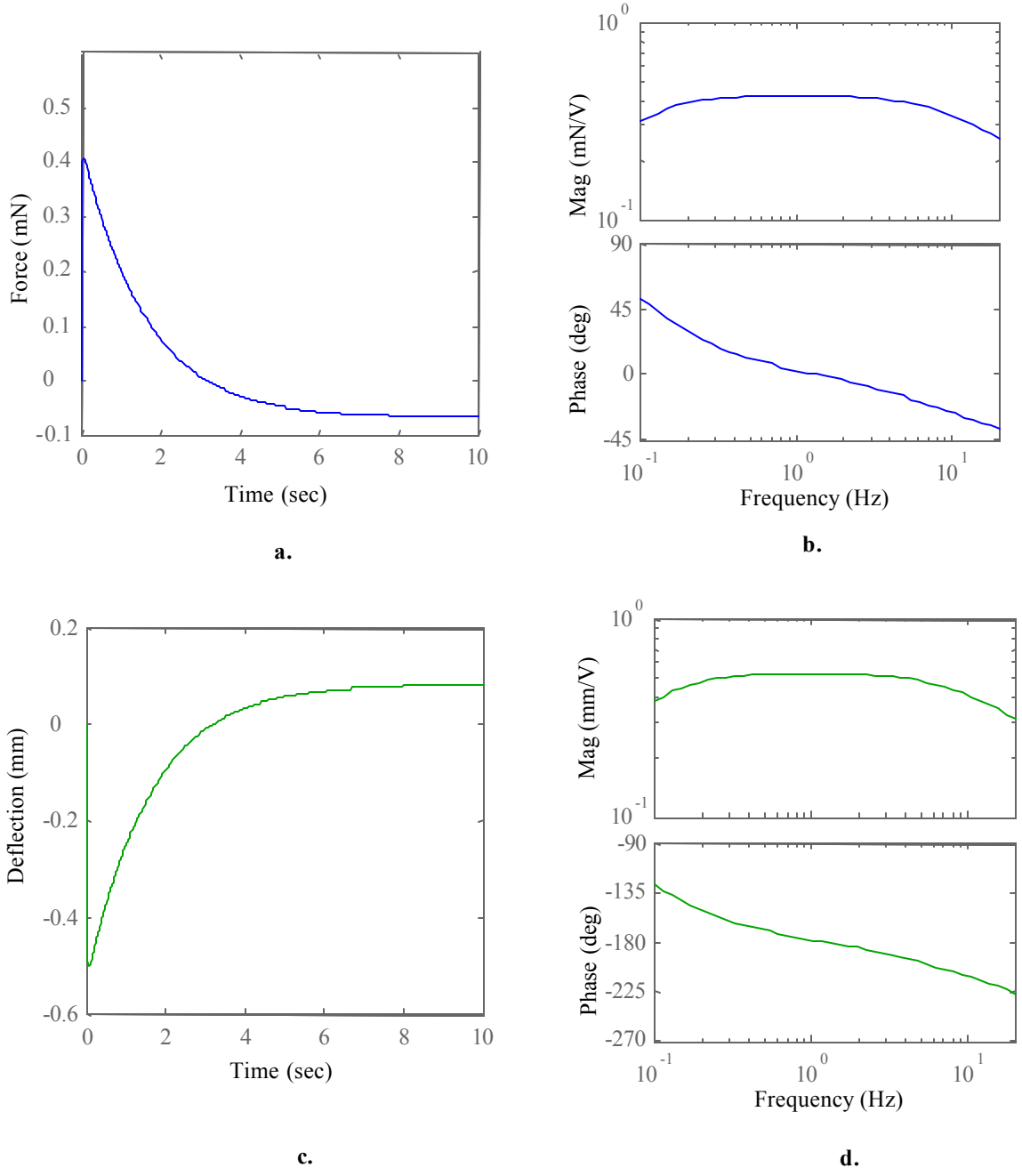

Figure 4.1: Blocked force and free deflection with voltage input for a t=0.2mm, w=5mm, L_d=17mm actuator: a) Blocked force step response (1V step), b) Blocked force frequency response., c) Free deflection step response (1V step), d) Free deflection frequency response

4.1.2 Force versus Deflection

With piezoelectric benders, the ability of the actuator to generate force decreases linearly with deflection – a force versus deflection curve (plotted on linear axes) consists of a straight line between the blocked force and the free deflection. A set of experiments were conducted on an actuator with dimensions t=0.2mm, w=5mm, and L_d=17mm to confirm that a similar relationship holds for ionic polymer benders. The force exerted by the polymer actuators was measured using a Transducer Techniques GSO-10 10gram load cell with TMO-1 signal conditioner/amplifier. To allow precise positioning of the load cell relative to the actuator, the load cell was mounted, as shown in Figure 4.2, to the carriage of a screw-driven precision

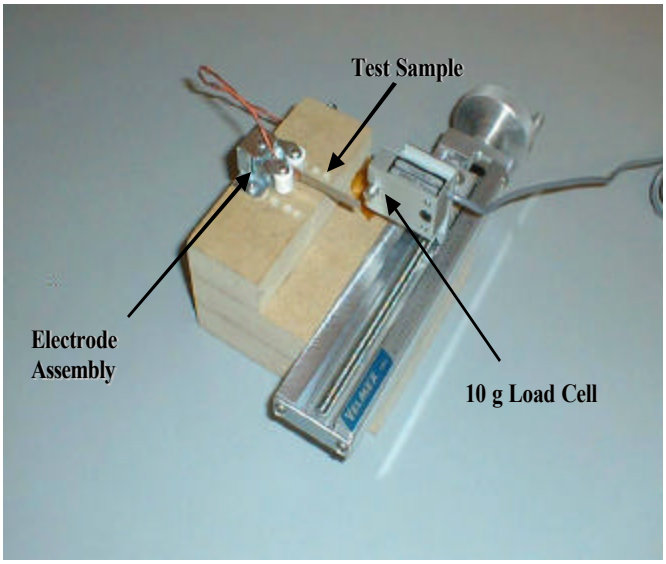

Figure 4.2: Fixture used to generate experimental force versus deflection curve for ionic polymer actuators

slide, and the relative position of the load cell was measured using the slide's scale and graduated dial. A dSPACE DS1102 DSP was used to generate the electrical input, which was amplified using an HP power amplifier, then applied to the actuator through the set of electrodes mounted to the fixture base. The experimental force versus deflection curves were generated in the following manner. The polymer actuator was mounted in the fixture by clamping it between the electrodes, which were both held at electrical ground. The electrodes were positioned such that the point of contact between the actuator and the nylon screw threaded through the load cell sensing element was 1mm to 2mm from the end of the actuator. The neutral position (zero external force with grounded electrodes) of

the actuator tip was measured by moving the load cell towards the polymer sample until a small, non-zero force was measured by the load cell. The load cell was then backed away from the actuator until the measured force dropped back to zero, and the position of the load cell was recorded as the actuator neutral position – the neutral position was recorded between each step response. To measure force with deflection, the load cell was backed the desired distance away from the actuator's neutral position in order to permit the actuator to deflect before coming in contact with the load cell. A step voltage was applied to the actuator, and the peak force was recorded. The permitted deflection at which the actuator was unable to exert a measurable force on the load cell was considered the free deflection. This set of experiments was conducted for three voltage levels, 0.75V, 1.00V. and 1.25V.

Even in its neutral state (grounded electrodes and no external force), the ionic polymer actuator used in the force versus deflection experiment had a noticeable initial curvature. The actuator response varied significantly, depending on whether the direction of the induced curvature was in the same or in the opposite direction as the initial curvature. For this reason the force versus deflection experiments were performed for both orientations, which are denoted as 'prebend-towards' and 'prebend-away' for initial curvature towards the load cell and initial curvature away from the load cell, respectively.

There was noticeable scatter in the measured force exerted by the polymer actuator, especially with the lower input voltages. Much of the scatter at lower voltages is explained by the fact that the measured force is very small, so both noise and force transducer inaccuracies become significant relative to the force signal. The accuracy of the load cell was 0.05mN and the noise level was typically 0.02mN RMS. To reduce the effects of the scatter on any subsequent analyses, a straight line was fit (in a least squares sense) to the force versus deflection data. The measured data points along with the straight lines fit to them are shown for the prebend-away orientation in Figure 4.3a. Notice that the match between the straight line and the data points improves with increasing voltage. The reasonable match between the data points and the straight lines confirms that the relationship between force and deflection can be approximated by a straight line between the blocked force and the free deflection. Figure 4.3b compares the experimental force versus deflection data for the prebend-towards and the prebend-away orientations. With the exception of the 0.75V data, the prebend-away orientation provided higher forces and deflections. Note that the actuator used to identify the model parameters in Chapter 3 was plated in a different

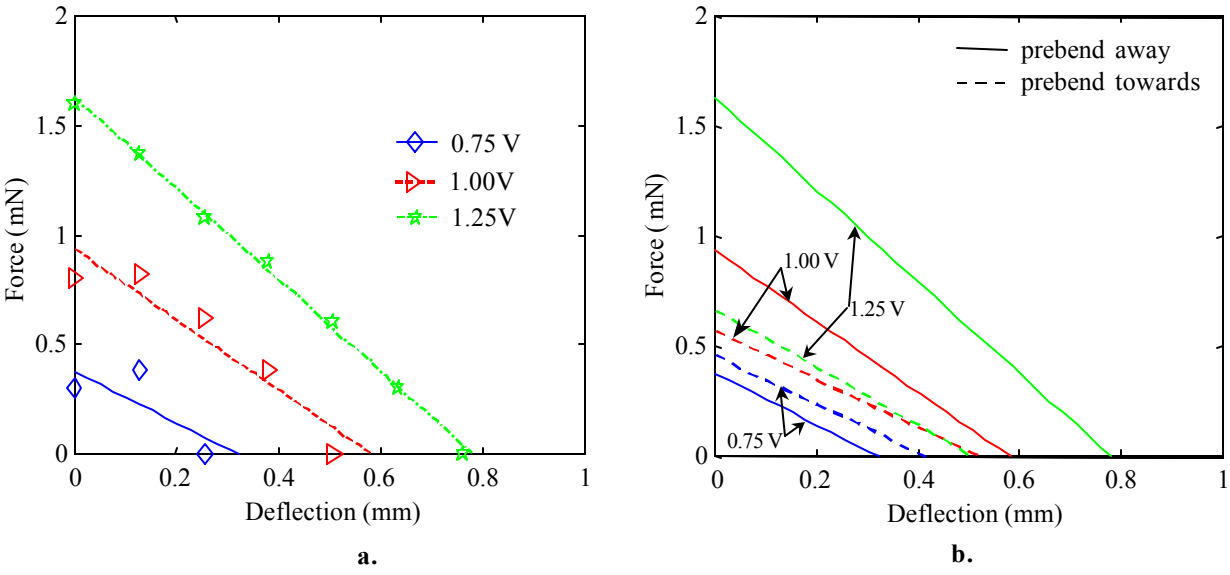

Figure 4.3: Force versus deflection for a 5mm x 17mm actuator: a) initial curvature away from load cell., b) Both orientations

batch than the actuator used for the force versus deflection experiments and did not have any significant initial curvature. Also, its performance did not exhibit any orientation dependence. Whether or not the base material (Nafion) of the two actuators came from the same batch is unknown. Actuator response also depends heavily on the level of hydration. The actuators were stored, fully hydrated, in deionized water. To prevent dehydration during the experiments, which were conducted in air, deionized water was brushed on the actuators at approximately one minute intervals – frequently enough to keep surface of the actuators wet.

As mentioned in Chapter 3, experiments involving step inputs often did not yield consistent results. Significant sample to sample variations were observed – in some cases a factor of two or more in the peak response with a step input. The variations appeared to be greatest between samples that were plated in different batches. For example, compare the peak values of the step responses shown in Figure 4.1 to the peak 1V values shown in Figure 4.3. The figures correspond to actuators that have identical dimensions but are from two different batches. The peak blocked force values are 0.41mN in Figure 4.1 and 0.57mN and 0.93mN in Figure 4.3 for the prebend-towards and prebend-away orientations, respectively. The ratio of the maximum to the minimum value is 2.3. Interestingly, comparing the peak free deflections in the same fashion yields a ratio of only 1.2. A plausible

explanation for the different force and deflection ratios is that the composite (hydrated base material with electrodes) modulus of the transducer material from one batch was significantly higher than the modulus of the material from the other batch, a distinct possibility given the variability in the plating process. Equations (4.1) and (4.2) indicate that a change in modulus will affect the blocked force magnitude but not the free deflection. Inconsistent responses were also observed with repeated experiments performed on the same transducer with no changes in the experimental setup, but these variations were generally smaller. Other researchers (Nemat-Nasser, 2002) have reported similar issues. Because of these inconsistencies, the values reported in this work, as well as those reported in other literature relating to ionic polymer transducers, should be considered approximate. There was less experimental variation at higher frequencies (above 1Hz), at least when comparing the results of repeated experiments on the same sample. Whether this observation is a result of the 'averaging' nature of frequency domain experiments (relative to comparing individual time domain experiments) or the ionic polymers actually behave more consistently above 1Hz was not explored.

4.1.3 Comparison with Piezoelectric Bimorph Actuators

The blocked force and free deflection expressions for piezoelectric bimorphs, presented by Germano (1972), are useful for comparing cantilevered ionic polymer actuators to piezoelectric benders. The relations are

$$(\frac{f}{v})^{\dot{u}} = \frac{3d_{31}Y_1^E w_p t_p}{8L} \text{ and } (\frac{u}{v})^f = \frac{3d_{31}L^2}{2t_p^2}, \tag{4.3}$$

where d_{31} is the tranverse piezoelectric strain coefficient, Y_1^E is the short-circuit Young's modulus in the longitudinal direction, and t_p and w_p are the total thickness and the width of the piezoelectric bender. These equations are for piezoelectric bimorphs with no substrate and with electrodes on the outer surfaces only (commonly referred to as a series bimorph). For PZT-5H-S4, d_{31}=190E-12m/V and Y_1^E=66GPa, and for PVDF, d_{31}=23E-12m/V and Y_1^E=2-4GPa (3GPa will be used in this work). Table 4.1 shows a comparison of the blocked force and free deflection predicted for piezoelectric benders (based on equations (4.3)) with the ionic polymer actuator peak blocked force and peak free deflection predicted using the equivalent-circuit model. The actuator dimensions are t=t_p=0.2mm, w=w_p=5mm, and L_d=L=17mm. Because the voltage corresponding the maximum allowable electric field for

Table 4.1: Comparison of blocked force and free deflection for 0.2 x 5 x 17 mm actuators

	applied field (MV/m)	applied voltage (V)	blocked force (mN)	free deflection (mm)
PZT-5H-S4	0.30	60	17	0.12
PVDF	6.0	1200	1.8	0.30
ionic polymer	0.006	1.2	0.49 (peak)	0.60 (peak)

PVDF would result in an extremely high applied voltage (6000V), only 20% of the maximum field was used in the table 4.1 calculations.

4.1.4 Energy Density

Another useful metric is energy density, the maximum mechanical work an actuator can perform divided by its volume (volumetric energy density e_v) or by its mass (gravimetric energy density e_v). Since the work done over a displacement from x_1 to x_2 is $\int_{x_1}^{x_2} f(x)\,dx$, where f is the applied force, the maximum work that can be done by an actuator is the area under its force deflection curve. In the case of piezoelectric actuators and ionic polymer transducers, this area corresponds to one half of the product of the blocked force and the free deflection (Wang et al., 1999). Note that the portion of an actuator that is clamped between the electrodes is unable to perform mechanical work, and its dimensions can be varied without affecting the actuator's performance. For this reason, the energy densities presented in this work were calculated using the 'active' volume or mass, that is, the portion of the actuator not clamped between the electrodes. As stated, the definitions of the energy densities e_v and e_v do not address the issue of frequency dependence; however, frequency dependence can be incorporated if one views the energy density as the maximum amount of work, normalized by volume or mass, that the actuator can perform per quarter cycle at a particular frequency.

For ionic polymer actuators, the energy densities are one half the magnitude of the product of equations (4.1) and (4.2) and the square of the applied voltage divided by either volume or mass. Expressing the applied voltage in terms of the electric field strength E eliminates the remaining actuator dimensions from the energy density expressions. The

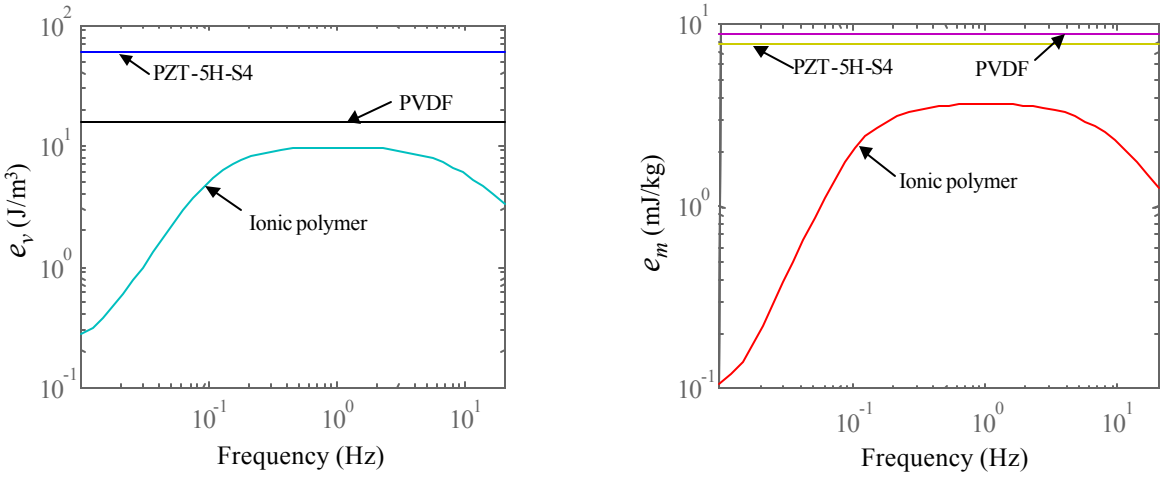

Figure 4.4: Predicted energy density versus frequency for PZT-5H-S4, PVDF, and ionic polymer benders with dimensions $t = t_p$=0.2mm, $w = w_p$=5mm, and L_d=L=17mm: a) volumetric energy density e_v, b) gravimetric energy density e_m

energy densities for ionic polymer actuators are

$$e_{\text{vol}} = \left|\frac{9d^2Y}{8}\right| E^2 \text{ and } e_{\text{m}} = \left|\frac{9d^2Y}{8\rho_m}\right| E^2. \tag{4.4}$$

Note that the independence of d from actuator thickness t has not been confirmed experimentally. As a result, there is a possibility that the energy densities in equation (4.4) are not independent of t, even though t does not appear explicitly in the expression. For piezoelectric actuators, one half the product of the blocked force and the free deflection (equations (4.3)) results in

$$e_{\text{vol,p}} = \frac{9d_{31}^2 Y_1^E}{32} E^2 \text{ and } e_{\text{m,p}} = \frac{9d_{31}^2 Y_1^E}{32\rho_m, p} E^2, \tag{4.5}$$

where $\rho_{m,p}$ is the density of the piezoelectric material.

In Figure 4.4, the predicted volumetric and gravimetric energy densities versus frequency are compared for 0.2mm x 5mm x 17mm PZT-5H-S4, PVDF, and ionic polymer benders. The applied electric fields are those listed in table 4.1. As mentioned previously, the piezoelectric actuator responses are considered independent of frequency, so the corresponding energy density versus frequency plots are simply horizontal lines. The energy densities of the ionic polymer bender are below those corresponding to the PZT and PVDF

bimorphs, but from 0.1Hz to 10Hz they are all within an order of magnitude of one another. Note that ionic polymer actuators are able to withstand greater voltages than the 1.2V input used to create the Figure 4.4 plots. The 1.2V input was chosen to avoid hydrolysis, which leads to faster dehydration of the polymer actuator. The shape of the plots in Figure 4.4 clearly indicates that ionic polymer transducers function poorly below 0.1Hz. Also, their best performance, in terms of energy density, is realized between 0.3Hz and 4Hz.

Shahinpoor (1999) presented a plot of force versus deflection for an Li^+ cation 0.2 x 6.4 x 25mm cantilevered ionic polymer actuator excited by a 2V 0.5Hz signal. The blocked force and free deflection reported by Shahinpoor (1999) were approximately 15mN and 1.6mm, respectively – compared to 0.74mN and 2.2mm predicted using the equivalent-circuit model and the same dimensions. It is interesting to note that the blocked force values differ by more than an order of magnitude, but the free deflections are relatively close. Again, a difference in moduli may account for part of the difference in reported force values, but it is unlikely that the moduli differed by an order of magnitude, leaving a portion of the discrepancy unexplained. Other reported values for the blocked force (for similar actuator dimensions) better match those presented in this work. See, for example, Mojarrad and Shahinpoor (1997a) and Bar-Cohen et al. (2001a). A range of values for the volumetric energy density as a function of voltage was recently presented by Bar-Cohen et al. (2001a). The values were based on a 'phenomenological' model and are approximately three orders of magnitude greater than the energy densities reported in this work. Bar-Cohen et al. (2001a) reported a volumetric energy density ranging from 6E3 to 16E3J/(m^3V), which corresponds to a range of 7.2E3 to 19E3J/m^3 at 1.2V, compared to the value of 9.6J/m^3 presented in this work. One possible explanation for a portion of this difference is that the energy density figures in this work are based directly upon predicted blocked force and free deflection of cantilevered benders. If one calculates the energy density based on maximum longitudinal stress and strain without also considering the bender actuator's geometry, the resulting energy density will be several times greater. Further explanation of the large difference in reported energy densities is not attempted because the calculations behind the energy density presented by Bar-Cohen et al. (2001a) were not given.

4.1.5 Linearity

In the process of characterizing ionic polymer transducers, a brief, experimental exploration of the input level dependence of ionic polymer transducers was performed. Voltage-step inputs with magnitudes 0.75V, 1.00V, 1.25V, and 1.50V were applied to a 0.2mm x 5mm x 10mm free length actuator that did not exhibit any significant initial curvature. Between step inputs, a 1.00V, 0.5Hz sine wave was applied to the transducer for a 30 seconds or more. The blocked force was measured using the 10gram load cell described earlier in this chapter. The electrical current was measured by amplifying and measuring the voltage drop across a 0.1- resistor that was placed between the negative actuator electrode and ground. To allow 'negative' force measurements, the load cell was placed relative to the actuator tip such that there was a slight preload. The preload was subtracted from the force measurement during post processing. Figure 4.5a shows the current and blocked force responses. In Figure 4.5b, the current and blocked force plots from Figure 4.5a are divided by the input magnitude and replotted. If the actuator behaves linearly with respect to excitation level in the 0.50V to 1.50V range, the plots will be identical. The peaks of the normalized blocked force responses overlay reasonably well, but approximately one second after the step, the normalized responses no longer match. In fact, the steady state blocked force with the 1.50V step is in the opposite direction than the initial response. The normalized 1.00V and 0.75V current plots overlay extremely well, but the 1.25V and 1.50V do not match as well. Although these experiments do not constitute an exhaustive study, they support the notion that at or below 1.25V, ionic polymer actuator behavior is approximately linear with respect to input level. This linear approximation appears to be more accurate at higher frequencies, indicated by fact that the match between the normalized responses is best near the peak and grows worse as steady state is approached.

4.2 Ionic Polymer Sensors

Although the vast majority of the literature pertaining to ionic polymer transducers is focused on actuation, the bidirectional electromechanical coupling they exhibit allows them to be used for sensing as well. When given a mechanical input, an ionic polymer transducer generates a measurable electrical signal. For the cantilevered-bender configuration, the logical mechanical inputs are force and deflection (or velocity) of a point at a distance L_d from

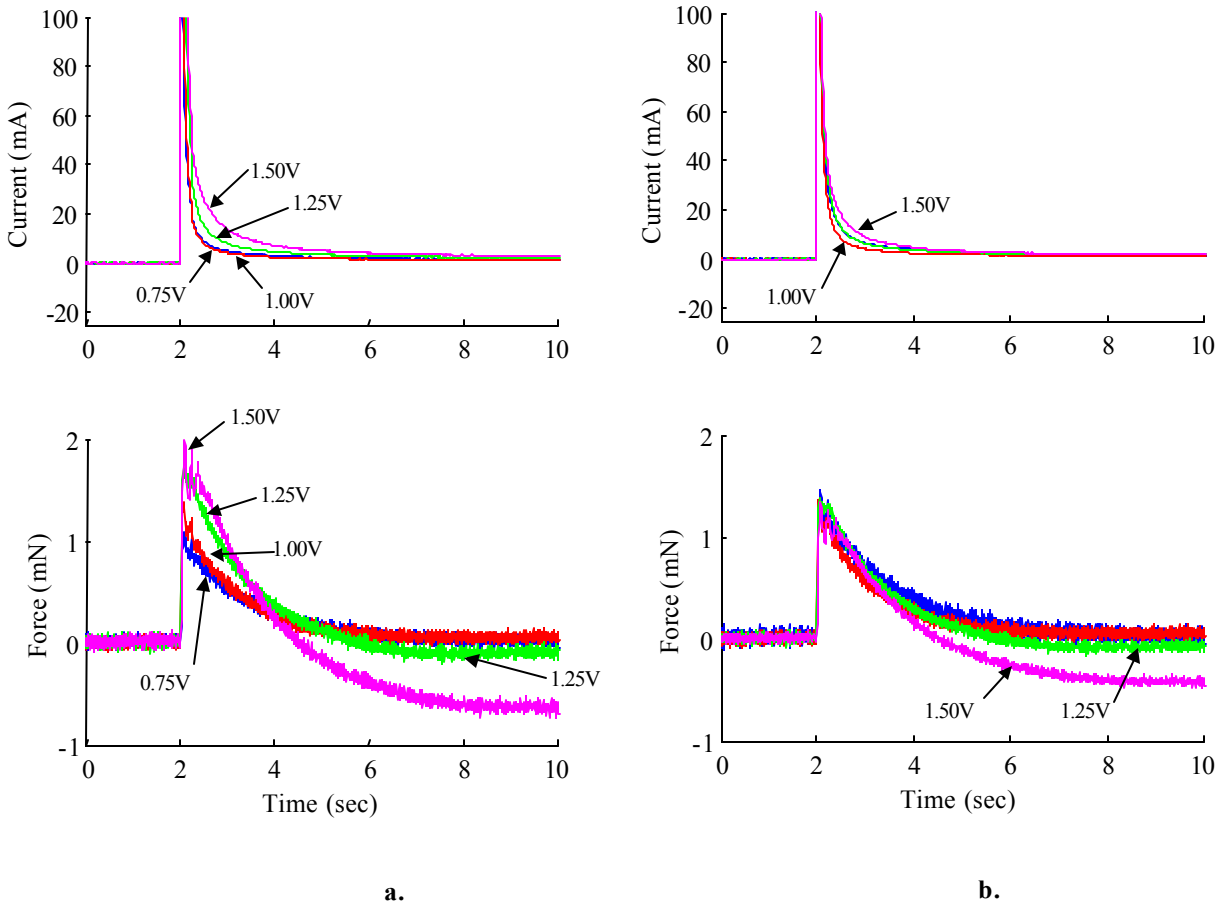

Figure 4.5: Current and blocked force with 0.75V, 1.00V, 1.25V, and 1.50V step inputs: a) raw data, b) normalized to 1.00V.

the supported end. The natural electrical quantities to measure are voltage and charge (or current). With ideal signal conditioning, the polymer electrodes can be considered to be at either a short-circuit condition, for charge measurement, or an open-circuit condition, for voltage measurements. The two mechanical quantities and two electrical quantities result in a total of four possible sensor relationships. For example, one combination is measuring open-circuit voltage while imparting a mechanical displacement. To make the best use of ionic polymer sensors, the most suitable combinations must be identified. These combinations will provide relatively direct relationships between the mechanical and electrical quantities and will exhibit high sensitivity.

4.2.1 Sensor Equations

The four sensor equations can be derived using the equivalent-circuit model derived in Chapter 2. The analysis is straightforward and was discussed earlier in this work, so only the final sensor equations are presented in this chapter. Also, it is assumed that the reader is already familiar with the nomenclature, so only new or particularly important terms will be identified. After all four equations are presented, in terms of equivalent-circuit parameters as well as transducer dimensions and material properties, their frequency responses will be plotted. Then the merits of the various input-output quantities will be discussed. In the equations presented below, a change from displacement to velocity or charge to current can be accomplished by simply multiplying the variable representing displacement or charge by the Laplace variable s.

Open-circuit voltage with a displacement input at a distance L_d from the supported end of the bender is given by

$$(\frac{v}{u})^i = \frac{sNR_{dc}Z_{m1}}{R_{dc}+Z_p} = \frac{s3dt^2Y\rho_{dc}}{4L_dL_t(1+s\eta\rho_{dc})}. \tag{4.6}$$

If instead, a force input is applied at L_d, the open-circuit voltage is described by

$$(\frac{v}{f})^i = \frac{NR_{dc}Z_{m1}}{(Z_{m1}+Z_{m2})(R_{dc}+Z_p)} = \frac{s3dL_d^2\rho_{dc}}{wtL_t(1+s^2\frac{12\rho_mL_{free}^4}{\Gamma^4Yt^2})(1+s\eta\rho_{dc})}. \tag{4.7}$$

The inertial term Z_{m2} can be eliminated from equation (4.7) if the operating frequency is well below the first natural frequency of the bender. The result is the much simpler expression

$$(\frac{v}{f})^i = \frac{NR_{dc}}{R_{dc}+Z_p} = \frac{s3dL_d^2\rho_{dc}}{wtL_t(1+s\eta\rho_{dc})}. \tag{4.8}$$

Measuring short-circuit charge with a displacement input, or short-circuit current with a velocity input will correspond to the expression

$$(\frac{i}{\dot{u}})^v = (\frac{q}{u})^v = \frac{-NZ_{m1}}{Z_p} = \frac{-3dtwY}{4L_d}, \tag{4.9}$$

where q is -1 times the charge that is generated at the positive electrode of the sensor. The -1 is a consequence of the polarities and sign conventions used in the model derivation. The fourth sensor equation, which corresponds to short-circuit charge with a force input, is

$$(\frac{q}{f})^v = \frac{-NZ_{m1}}{s(Z_{m1}+Z_{m2})Z_p} = \frac{-3dL_d^2}{t^2(1+s^2\frac{12\rho_mL_{free}^4}{\Gamma^4Yt^2})}. \tag{4.10}$$

As with open-circuit voltage with a force input, the inertial term can be ignored if the operating frequency is well below the first resonant frequency of the polymer sensor, resulting in the simplified expression.

$$(\frac{q}{f})^v = \frac{-N}{sZ_p} = \frac{-3dL_d^2}{t^2}. \tag{4.11}$$

Figure 4.6 contains frequency-response plots corresponding to the sensor expressions in equations (4.6-4.11) for an ionic polymer sensor with dimensions t =0.2mm, w =5mm, L_t=30mm, L_d=17mm, L_{free}=19mm. For the expressions in which force was the mechanical input, the frequency responses both with and without the inertial terms are shown. The predicted first natural frequency of the polymer is 35Hz.

First, consider the open-circuit (OC) voltage that would be generated with a displacement input at 1Hz, 10Hz, and 20Hz, where the sensitivity is 0.038V/m, 0.067V/m, and 0.083V/m, respectively. A 2mm displacement (just over 10% of the distance L_d=17mm) would result in an OC voltage of only 77μV at 1Hz, increasing to 134μV at 10Hz and 166μV at 20Hz. These voltages are quite low, but with proper signal conditioning they can be measured with reasonable accuracy. At very low frequencies, the OC voltage will be extremely small, indicating that OC voltage sensing should not be considered for measuring displacement in quasi-static applications. Furthermore, the ideal sensor for most applications will have a response magnitude that does not vary with frequency. The OC voltage over displacement magnitude has a slope between zero and one decade (of magnitude) per decade (of frequency). Note that with this slope, simply changing the input from displacement to velocity will not 'flatten out' the response magnitude. Instead, it will decrease with increasing frequency. Inspection of equation (4.6) reveals that the sensitivity is increased by decreasing the distances L_d and L_t. To maximize the sensitivity, one should choose the shortest bender possible for the expected displacement magnitude. Recall that the model for the ionic polymer bender is based on the assumptions associated with small deflections of slender beams. If the deflection at L_d is too great relative to L_d, these assumptions will be violated, and the accuracy of the predicted sensitivity may suffer. Henderson et al. (2001) presented an experimental frequency response of OC voltage over displacement for a 0.32mm x 11mm x 29mm cantilever that had been allowed to dry prior to testing. The reported sensitivity ranged from 0.065V/m to 0.070V/m in the 1-20Hz range, a flatter response than predicted in this work. Also, the magnitude was approximately a factor of two higher than the model in this work predicts for a fully-hydrated sensor with the same

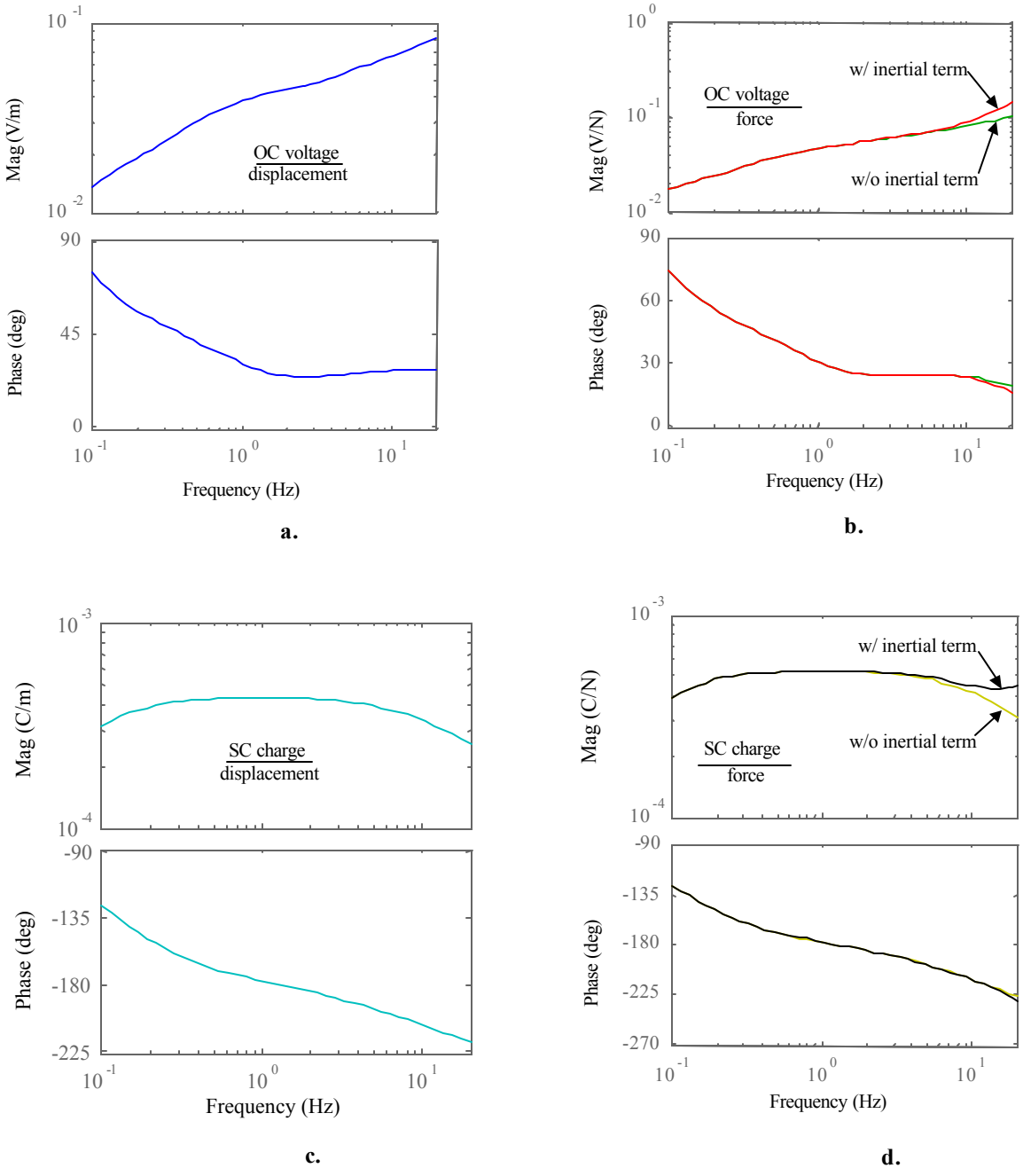

Figure 4.6: Sensor equation frequency responses: a) open-circuit (OC) voltage over displacement, b) OC voltage over force, c) short-circuit (SC) charge over displacement, d) SC charge over force.

dimensions. It is likely that, along with manufacturing variations, the level of hydration is responsible for the differences in the magnitude and the shape of the sensitivity. Both the modulus Y and the electrical impedance, which is proportional to $\frac{\rho_{dc}}{1+s\eta\rho_{dc}}$ increases as the polymer dries. These changes will both increase the sensitivity. The effect of hydration on the parameter d is unknown at this time.

If a force is applied perpendicular to the ionic polymer bender at a distance L_d from the clamped end, the shape of the OC voltage over applied force frequency response will closely resemble the OC voltage over displacement response well below the first natural frequency. This match occurs because, well below resonance, the force-deflection relationship is dominated by the bender stiffness, which has very little frequency dependence. The plots in Figure 4.6b show that, for the polymer considered in this example, the inertial term becomes significant above 10Hz, slightly less than one third the first natural frequency of 35Hz. Equation (4.8) shows that the sensitivity improves as the distance L_d is increased. This trend is not surprising because increasing L_d will reduce the bender's stiffness, resulting in a larger displacement for a given force and, therefore, a larger OC voltage. To achieve maximum sensitivity, one should choose the longest sensor that can withstand the applied force without unacceptably large deflections. Below resonance, a force of 1.6mN will correspond to the 2mm deflection used in the 'OC voltage with displacement input' example and will result in a 77μV output at 1Hz, 140μV at 10Hz, and 230μV at 20Hz (the deflection will be significantly greater than 2mm at 20Hz because of the proximity to the first natural frequency). As with OC voltage over displacement, the output is small but measurable.

With suitable signal conditioning, the short-circuit (SC) charge generated by the polymer sensor can be measured. A potential advantage to measuring SC charge instead of OC voltage is that the SC charge over position transfer function (shown in Figure 4.6c) is relatively flat from 0.2Hz to 5Hz. Note that care must be taken in designing the signal conditioning circuitry to perform SC charge measurements in this range. As with OC voltage over displacement, the magnitude of the SC charge over displacement frequency response drops off rapidly at very low frequencies (below 0.1Hz); therefore, SC charge measurement will not yield a usable signal with quasi-static displacements. Examining equation (4.9) reveals that, as with OC voltage displacement sensing, decreasing the length of the sensor will result in a higher sensitivity. Again, the shortest possible sensor should be used. Unlike

Table 4.2: Comparison of 0.2 x 5 x 17mm ionic polymer sensors to 0.2 x 5 x 17mm piezoelectric bimorph sensors

	piezo-sensor			ionic polymer
	equation	PZT sensitivity	PVDF sensitivity	sensitivity (0.1Hz/10Hz)
$(\frac{v}{u})^i$	$\frac{3d_{31}Y_1^E t^2}{8\epsilon L^2}$	41E3 V/m	33E3 V/m	14E-3 V/m / 67E-3 V/m
$(\frac{v}{f})^i$	$\frac{3d_{31}L}{2ewt}$	300 V/N	5330 V/N	17E-3 V/N / 88E-3 V/N
$(\frac{q}{u})^v$	$\frac{3d_{31}wtY_1^E}{8L}$	280E-6 C/m	1.5E-6 C/m	310E-6 C/m / 340E-6 C/m
$(\frac{q}{f})^v$	$\frac{3d_{31}L^2}{2t^2}$	2.0E-6 C/N	0.25E-6 C/N	390E-6 C/N 450E-6 C/N

OC voltage over displacement sensing, increasing the sensor width w will also increase the sensitivity.

The relationship between SC charge over displacement and SC charge over force is identical to the relationship between OC voltage over displacement and OC voltage over force. For the dimensions chosen, the force-displacement relationship, as the operating frequency approaches resonance, actually helps to flatten the magnitude plot relative to the SC charge over position frequency response. As with OC voltage over force, the longest sensor that is feasible should be used in order to maximize the force input sensitivity.

4.2.2 Comparison with Piezoelectric Bimorph Sensors

The relations given by Germano (1972) will be used to compare ionic polymer sensors to piezoelectric bimorphs with dimensions that are identical to the polymer sensor used in the examples above. As with the actuator comparisons, PZT-5H-S4 and PVDF are used as representative piezoelectric materials. In addition to the material constants listed in the previous section, the permittivities are required for calculating some of the sensitivities. The values used are 16E-9F/m for PZT-5H-S4 and 110E-12F/m for PVDF. Discussions will focus on comparing PVDF and ionic polymer sensors because they are both 'soft' transducers and would be more likely to compete with one another in consideration for practical applications than piezoceramics and ionic polymers. Table 4.2 lists the expressions for the piezoelectric bimorph sensitivities (assuming operation below the first natural frequency). Also, the values of these sensitivities are compared to those predicted for an ionic polymer transducer at 0.1Hz and at 10Hz.

The sensitivity of the ionic polymer sensor for the SC charge over force relationship is over three orders of magnitude greater than that of the PVDF bimorph. Comparing the expression in the last row of Table 4.2 with equation (4.11), it becomes apparent that, because the transducer dimensions are identical, the difference results from d (for the ionic polymer) being approximately three orders of magnitude larger than d_{31} of PVDF. Recall that the physical interpretations of d and d_{31} are slightly different. In the ionic polymer model, d represents the induced strain *at the surface* of the bender for a given electric field. The interpretation of d_{31} (for piezoelectric devices) is more general – it relates strain and electric field, regardless of geometry. For series bimorphs, it is legitimate to compare the values of $d_{31}/2$ with d. The ratio of ionic polymer sensitivity to PZT sensitivity is not as great, due to the fact that d_{31} of PZT is approximately eight times greater than d_{31} for PVDF.

Inspection of equation (4.9) and the piezo-sensor expression in the third row of Table 4.2 reveals that the differences between the sensitivity of ionic polymer sensors and piezo-sensors will be due to the strain coefficient modulus products, $(d_{31}Y_1^E)/2$ for piezo-sensors and dY for ionic polymers. Because the modulus of PVDF is an order of magnitude greater than the hydrated ionic polymer modulus, the ratio of ionic polymer sensitivity to PVDF sensitivity is only two orders of magnitude, instead of the three orders of magnitude seen with the SC charge over force sensitivities. The modulus of PZT is even greater (over 20 times the PVDF modulus), resulting in the PZT and ionic polymer sensitivities that are of the same order of magnitude.

Now compare the sensor equations (without inertial terms) that involve measuring OC voltage, equation (4.6) with the first row of Table 4.2 and equation (4.8) with the second row. As with the SC charge equations, differences in the sensitivities of ionic polymer sensors and piezo-sensor will result from the fact that the strain coefficients and moduli are dissimilar. In addition, these equations each include a term that is proportional to the Laplace variable s times the electrical impedance. For the piezo-sensors the additional term is $\frac{1}{\epsilon}$, and for ionic polymer sensors it is $\frac{s\rho_{dc}}{1+s\eta\rho_{dc}}$. Because, in the frequency range considered in this work, ionic polymer transducers exhibit a very high capacitance relative to PZT and PVDF, their electrical impedance is relatively low. For PZT and PVDF the $\frac{1}{\epsilon}$ values are 62E6m/F and 9.1E9m/F, and for ionic polymer transducers, the value of $\frac{s\rho_{dc}}{1+s\eta\rho_{dc}}$ ranges from 67m/F to 240m/F over the 1Hz to 20Hz frequency range. The ratio of the PVDF

value to the ionic polymer value is roughly eight orders of magnitude, which accounts for the relatively small ionic polymer voltage sensitivities presented in Table 4.2.

4.2.3 Signal Conditioning

To this point, the discussion regarding piezo-sensors and ionic polymer sensors has been based on the assumption that the OC voltage and SC charge can be measured without significantly altering their values. This assumption is not always valid. First, consider voltage measurement. Any real device will have a finite input resistance and will load the sensor electrically, possibly decreasing its output voltage. Figure 4.7a shows an equivalent

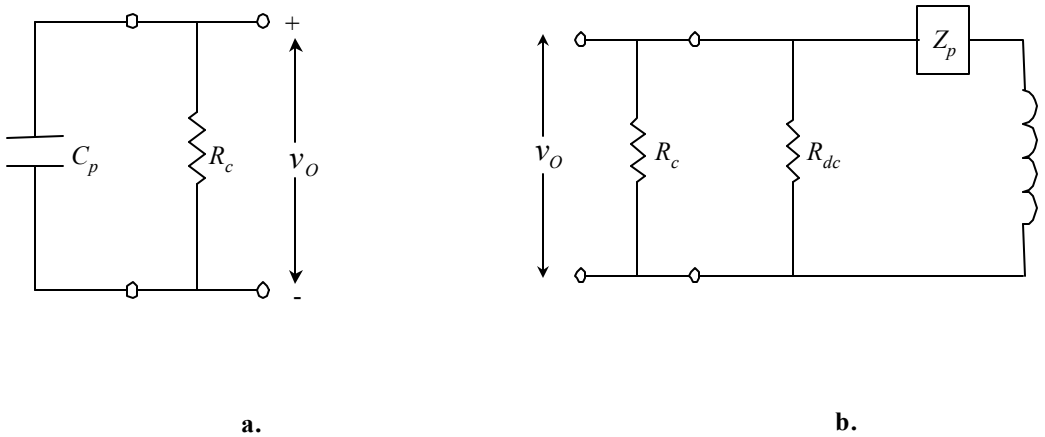

a. **b.**

Figure 4.7: Equivalent circuits for output voltage measurement: a) piezo-sensor, b) ionic polymer sensor

circuit that represents measurement of a piezo-sensor output voltage. For the purpose of this discussion, the piezo-sensor can be represented by an ideal capacitor. The buildup, on the piezoelectric sensor's capacitance C_p, of electrical charge that is generated through the electromagnetic coupling is responsible for the OC voltage. If the input resistance of the voltage measurement device is infinite (the ideal case), the OC voltage v_{oc} and generated charge q_i are related through $v_{oc} = \frac{q_i}{C_p}$. If a finite input resistance R_c is considered, the relationship between the measured voltage v_o and the generated charge becomes

$$\frac{v_o}{q_i} = \frac{sR_c}{1 + sR_cC_p}, \tag{4.12}$$

which acts as a differentiator below the pole at $\omega = 1/(R_c C_p)$ and has a flat response above the pole. Only for frequencies greater than $1/(2\pi R_c C_p)$ will the piezo-sensor sensitivities in Table 4.2 be realized. The capacitances of the piezo-sensors can be estimated using the relation $C_p = L_p w_p \epsilon / t_p$, which gives 47pF for the PVDF sensor and 6.8nF for the PZT bimorph. Combined with an input resistance of 1M- , a realistic value for a high impedance input, the corresponding corner frequencies for equation (4.12) are 3.4KHz for the PVDF sensor and 23Hz for the PZT. Below these frequencies, the voltage over mechanical input sensitivities will decrease with frequency, reaching a value of zero at DC. Also, in this region, the achieved sensitivity will depend directly on the value of the measuring device's input resistance. With R_c=1M- , the voltage over displacement sensitivity of the PVDF sensor is reduced to 9.4V/m at 1Hz – three orders of magnitude below it's OC value of 33E3V/m. While the PVDF bimorph sensitivity has been greatly reduced, it is still higher than the OC voltage over displacement sensitivity of the ionic polymer at 1Hz (14E-3V/m).

In Figure 4.7b, a circuit representing measurement of the output voltage of an ionic polymer sensor is shown. Because they appear in parallel, the DC resistance R_{dc} of the ionic polymer and the input resistance of the voltage measuring device can be combined. Using 1M- for R_c and the predicted value of 440- for R_{dc} results in 439.8- for the combined resistance. Since the presence of the measurement device's input resistance does not significantly alter the value of R_{dc}, the full value of the ionic polymer OC voltage sensitivities presented in Table 4.2 and Figure 4.6 can be achieved.

The short-circuit charge can be measured using the charge amplifier circuit shown in Figure 4.8a. The charge amplifier's transfer function is

$$\frac{v_o}{q_{sc}} = -\frac{sR_f}{sR_f C_f + 1}, \tag{4.13}$$

where q_{sc} is the SC charge generated at the positive electrode of the polymer sensor. Well above the corner frequency of the charge amplifier, which acts as a high pass filter, the gain is $-\frac{1}{C_f}$. The corner frequency of the charge amplifier is at $f_c = \frac{1}{2\pi R_f C_f}$, so the choice of C_f is a compromise between achieving an adequate high frequency gain (requires a small enough C_f) and low enough corner frequency (requires a large enough $R_f C_f$ product). Also, for the circuit to function properly, the values of R_f and C_f must be kept within a range that is considered reasonable for op-amp circuits. To determine a suitable range for the charge amplifier gain, consider the sensitivity of the SC charge over displacement

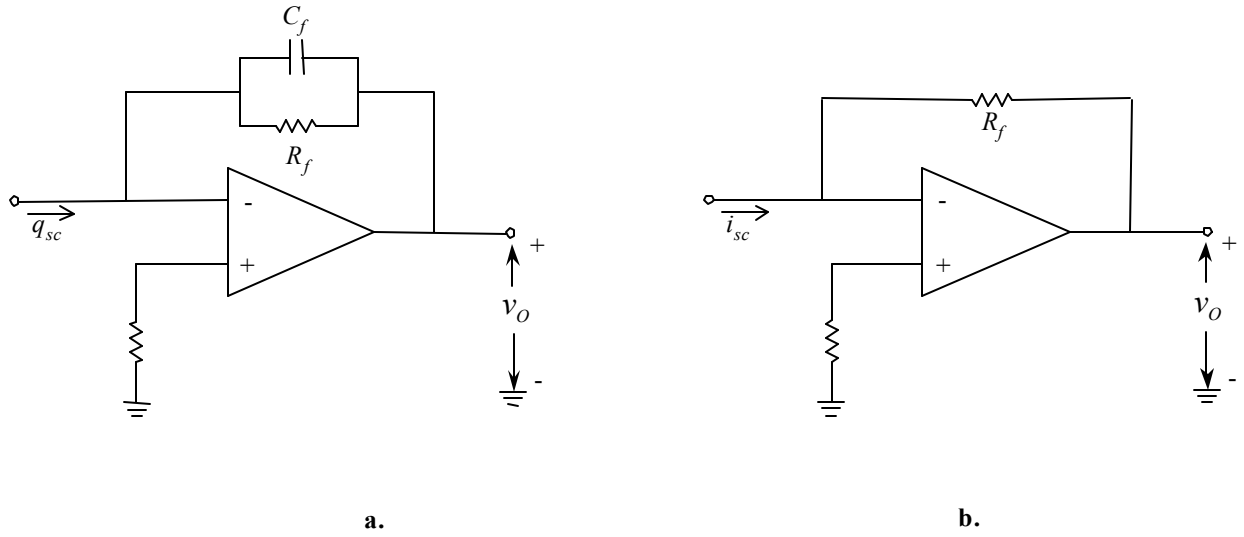

Figure 4.8: Signal conditioning circuits for measurement of short-circuit quantities: a) short-circuit charge measurement circuit, b) short-circuit current measurement circuit

transfer function shown in Figure 4.6c. Using a 2mm max displacement at L_d=17mm, the charge generated will be in the 0.5μC to 1μC range. A choice of C_f=460nF will result in a corresponding charge amplifier output from 1.1V to 2.2V, a range that can be measured readily with common data acquisition hardware. If a value of 465k- is chosen for R_f, the corner frequency will be 0.76Hz. The values of R_f and C_f that are considered optimal will depend on the application – the values presented in this work are chosen only to demonstrate that reasonable component values can be used to achieve a low corner frequency and produce measurable output voltages with realistic sensor inputs.

The circuit in Figure 4.8b will convert short-circuit current a voltage signal, and the output is related to the SC current through the expression

$$\frac{v_o}{i_{sc}} = -R_f. \tag{4.14}$$

Because the SC charge over displacement (SC current over velocity) sensitivities are small (see Table 4.2), a large R_f will be required in order to obtain reasonable output voltages.

4.2.4 Experimental Results

Figure 4.9 contains plots of experimental ionic polymer frequency responses for a sensor with dimensions L_{free}=25mm, L_d=20mm, w=5mm, t=0.2mm, and L_t=33mm. The SC

charge and current data were collected using the signal conditioning circuits described in section 4.2.3. An Analog Devices AD620 instrumentation amplifier, with the gain set at 100, was used to provide a high impedance input for the OC voltage measurement. As in Chapter 3, motion was imparted to the polymer using an APS Dynamics APS 113 long stroke shaker. A bracket with a wedge-shaped piece of phenolic was mounted to the shaker armature to provide the interface between the transducer and the shaker. The position of the armature was measured using a Novotechnik T25 linear potentiometer and an appropriate signal conditioning circuit. Manufacturer's specifications indicate that the linear potentiometer repeatability is 0.002mm, and the linearity is 0.06mm. To assure that the armature displacement corresponded to the polymer displacement at the point of contact, the polymer was positioned relative to the shaker such that a preload was applied and constant contact between the polymer transducer and the phenolic was maintained.

The input used for the Figure 4.9a OC voltage over displacement plot was a 0.57mm rms, 0-20Hz random displacement. The shape of the magnitude and phase plots match the predicted sensor response (0.9 times the response shown in Figure 4.6a – because the L_d and L_t values for the two figures are different), but the experimental magnitude plot is higher than expected, by a factor of approximately 1.2. This discrepancy is attributed to the fact that the model parameter identification was performed on a differnt polymer than that used in the Figure 4.9 experiment.

For SC charge over displacement, plotted in Figure 4.9b, both the scaled charge amplifier output and a corrected (filtered) version are shown. The corrected output was calculated during post processing by multiplying the measured frequency response by minus one times the frequency response of the inverse of the charge amplifier transfer function, and the 'not-corrected' plot corresponds to -C_f times the amp output. The input for the experiment was a 0.48mm rms, 0-20Hz random displacement, and the charge-amp circuit component values were C_f=460nF and R_f=465k- , resulting in a corner frequency of 0.74Hz. Both the magnitude and the phase of the corrected response match the predicted response well; however, neither the magnitude or the phase of the 'not-corrected' match the expected response below approximately 2Hz, highlighting the importance of the charge amplifier corner frequency.

The SC current over velocity plot, shown in Figure 4.9c, should match the corrected response shown in Figure 4.9b, since current and velocity are both first (temporal) deriv-

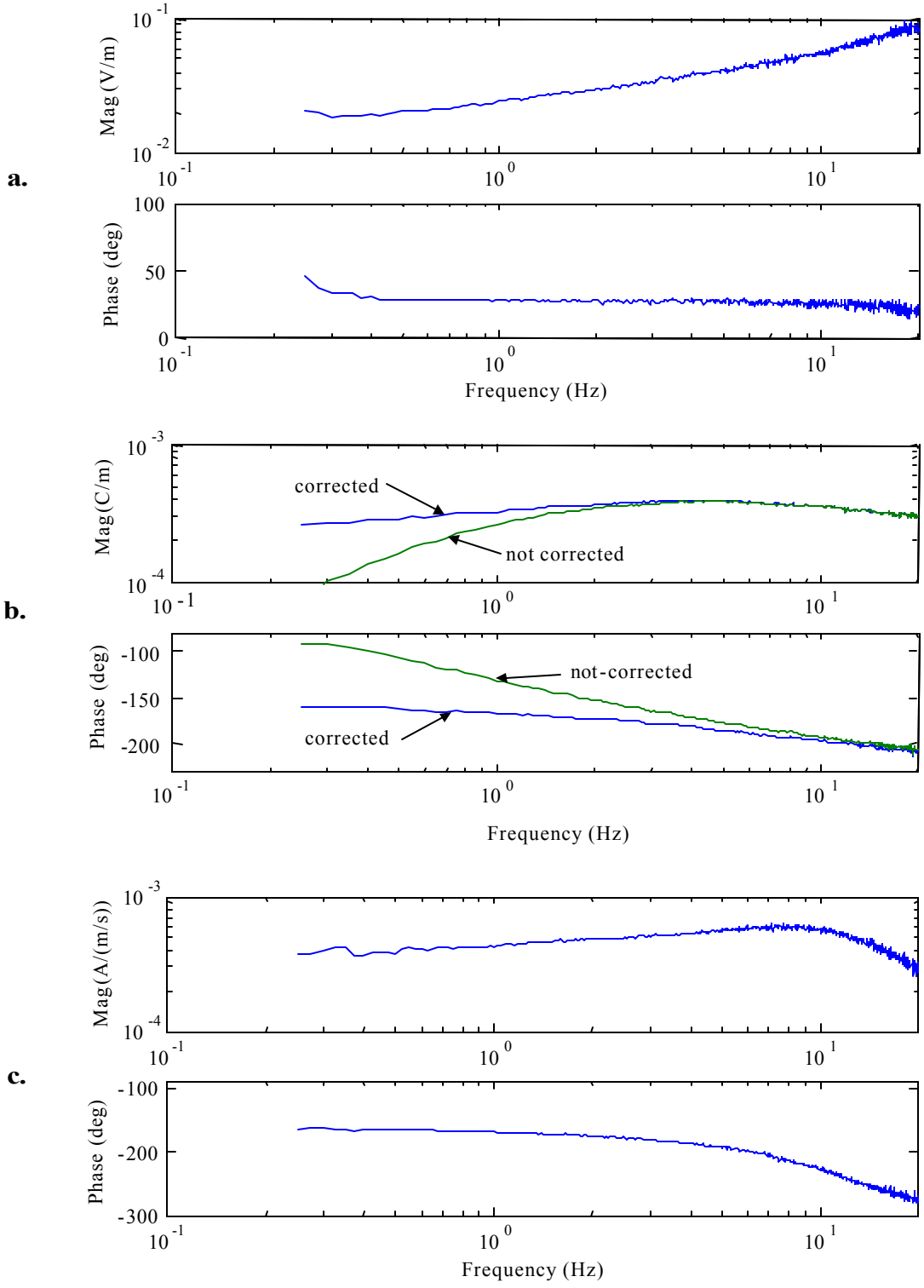

Figure 4.9: Ionic polymer sensor experiment frequency responses: a) OC voltage over displacement, b) SC charge over displacement, c) SC current over velocity.

atives of charge and displacement. The input for this experiment was an 8.6mm/sec rms, 0-20Hz random velocity, and the value of R_f (Figure 4.8b) was 100k- . Because the potentiometer measures position, not velocity, the SC current over displacement transfer function was calculated using the FFT analyzer. Time domain integration of the SC current over displacement response (to obtain SC current over velocity) was accomplished by multiplying each point of the frequency response by $\frac{1}{j2\pi f_i}$, where f_i is the frequency corresponding to a particular data point. Neither the shape of the magnitude plot nor the shape of the phase plot match well across the entire 0.1 to 20Hz frequency range. Relative to the SC charge over displacement response, the SC current over velocity plot magnitude plot has a greater maximum value, which occurs at a higher frequency. It also drops off rapidly above approximately 10Hz. The SC current over velocity phase plot exhibits excessive phase lag above 10Hz, dropping to a value of -275 degrees compared to -210 degrees for SC charge over displacement. The discrepancies between the measured SC current over velocity and SC charge over displacement frequency responses are attributed to non-ideal behavior of the SC current measurement circuit. The SC current magnitude in this experiment was only $4.5\mu A$ rms. It is possible that with signals this small, the ideal op-amp assumptions no longer apply, and the amplifier circuit is interacting with the polymer transducer in a manner not explained using the ideal op-amp assumptions.

No experiments were performed to demonstrate the use of cantilevered ionic polymer benders for force measurements; however, reason suggests that the quality of the results will be similar to the measurements taken with displacement inputs. This expectation results from the fact that, well below resonance, force and displacement are related through the stiffness of the polymer, which was demonstrated in Chapter 3 to have little to no frequency dependence in the frequency range considered in this work.

An important practical issue that surfaced in earlier sensor experiments is that care must be taken in selecting the material used for the fixture electrodes. The first ionic polymer sensor experiments attempted by the author were performed using a fixture with copper electrodes. A small current was generated at the fixture electrodes – apparently a result of the contact between the two dissimilar electrode metals, copper and gold. As a result, the open-circuit voltage measurement would slowly increase (as charge was built up on the sensor's capacitance) to a value of several millivolts, even when the sensor was at rest. Any voltage signal corresponding to a small mechanical input would be 'buried'

by the unwanted signal. Only a very large displacement or AC coupling would result in a dynamic signal large enough to be measured. This issue was addressed by using gold fixture electrodes.

4.2.5 Discussion

Ionic polymer transducers, used in the cantilevered-bender configuration, show promise as displacement and low-force dynamic sensors. They exhibit strong electromechanical coupling relative to PZT and PVDF bimorphs with identical dimensions. However, they also have much greater capacitance, resulting in low sensitivities when measuring OC voltage – despite the strong electromechanical coupling. This low OC voltage sensitivity is a consequence of the fact that a great deal of electrical charge can be stored by a large capacitor with very little electrical potential across it. To avoid the problems introduced by the high capacitance, SC charge should be measured. With the short-circuit boundary condition, the sensor's electrical impedance will not affect the measurement. An additional benefit from eliminating the effects of the polymer impedance is that the sensitivity varies less with changes in frequency relative to the OC voltage sensor quantities.

One aspect of ionic polymer sensor behavior that, unless overcome, will limit their usefulness is the frequency dependence of their sensitivity. Variations in the magnitude of the sensitivity will lead to distortion of any waveform that contains a broad range of frequencies – the shape of the sensor output waveform will not match the mechanical input waveform. Any phase shift, except for a linear phase lag, which corresponds to time delay, will also distort a broadband waveform. With these ideas in mind, inspection of the predicted sensitivities in Figure 4.6 reveals that only a narrow frequency range (approximately 0.3 to 3Hz) of the SC charge over position relation can convert mechanical inputs to electrical signals without distortion. Recall that the corner frequency of the charge amplifier must also be placed well below this frequency range for the amp output to follow the SC charge accurately. Another general observation regarding the Figure 4.6 plots is that none of the sensor relationships will produce a significant output at very low frequencies – they will not sense DC or quasi-static inputs.

4.3 Electrically Induced Permanent Strain

While performing experiments for the ionic polymer force versus deflection curve, presented in section 4.1, an unexpected phenomenon was observed. For some electrical inputs, a portion of the induced strain remains once the electric field is removed. To gain insight into this phenomenon, which will be referred to as the *permanent strain phenomenon*, a set of experiments was conducted on Nafion 117 based ionic polymer actuators. The goals of the study were to quantify the permanent strain phenomenon and to explore its relationship to the applied electrical signal, actuator dimensions, and boundary conditions. To this end, experiments were performed in which the electrical input, actuator length, and permitted initial deflection were varied.

Following is an example of the electrically induced permanent strain phenomenon. Figure 4.10 shows the path of the tip of a 0.2 x 5 x 27mm free length actuator when subjected to -2V DC for 30 seconds, then grounded again. The final position of the actuator tip is

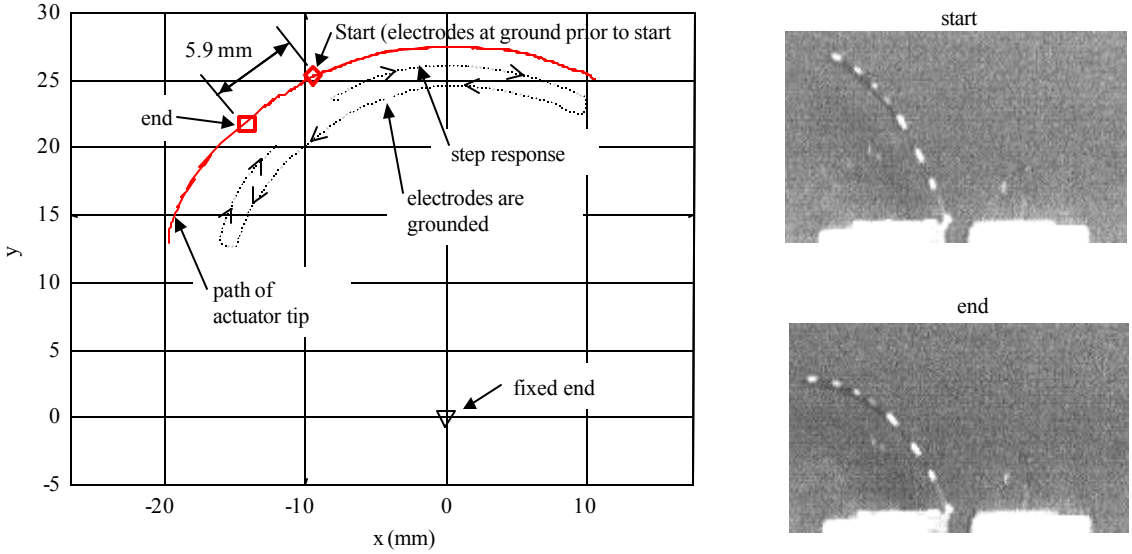

Figure 4.10: Path of 0.2 x 5 x 27mm free length actuator with -2V x 30 second pulse input

5.9mm from its position before the electrical cycle - a change in position greater than 20% of the actuator's free length. Also shown in Figure 4.10 are photos of a 29mm free length actuator at the beginning and end of an identical input. Note that the *neutral position*, the static position with zero electric field and zero external load, has moved in the direction opposite the initial deflection. This observation holds true for every experiment in which

the permanent strain phenomenon occurred. The extent to which this phenomenon occurs depends on several factors, such as actuator length, magnitude of applied voltage, and polarity of the input signal relative to initial actuator curvature.

4.3.1 Experimental Description

The permanent strain experiments were performed on 5mm wide Nafion 117 based ionic polymer actuators with Au electrodes and Li^+ cation. The actuators were provided by Dr. Mohsen Shahinpoor of the University of New Mexico and Dr. Kwang Kim of the University of Nevada-Reno. The actuators were used in the cantilevered-bender configuration. A dSPACE DS1102 DSP was used to measure the voltage applied to the actuator. Current measurement was performed by amplifying, then measuring (with the DSP) the voltage drop across a 0.1 Ohm resistor that was placed in series with the actuator. A RedLake high speed digital video camera, triggered by a signal from the DSP, and Image Express MotionTrace image analysis software were used to track actuator position. The input signals were generated using the DSP and, depending on the experiment, sent to either a power amplifier or to a transconductance amplifier. The amplifiers and current measurement circuit were connected such that one actuator electrode was tied to electrical ground at all times. As a result, any time the power amplifier output was set to zero, both electrodes were effectively grounded. To prevent the actuators from dehydrating during the experiments, deionized water was brushed on them at one to two minute intervals – frequently enough that their surface remained wet.

Most of the experiments described in this paper are based on an input consisting of a single *electrical cycle*. For the purpose of this paper, an *electrical cycle* is defined as any electrical input in which the polymer electrodes are at electrical ground at both the beginning and the end of the input. In an effort to understand the dependence of the change in neutral position on various input parameters, a series of experiments was conducted. Three types of inputs were used, a voltage pulse (constant voltage applied for a finite time) with various magnitudes and durations, a current pulse, and one cycle of a current square wave. Actuator free length was also varied.

4.3.2 Results and Discussion

To facilitate analysis of the experimental results, several quantities were calculated from the voltage, current, and position data that were collected. The current response was numerically integrated to determine the charge delivered to the actuator by the power source. The maximum value and final value of the delivered charge will be denoted by Q_{max} and Q_{final}, respectively. Note that since IPMCs are capacitive, some of the charge delivered to the actuator is 'returned' to the power source, so $|Q_{final}|$ is always less than $|Q_{max}|$. The voltage-current product was integrated to yield W_E, the electrical work done on the actuator by the power source. The magnitude of the change in neutral position (the permanent strain) Δ_{NP} is expressed in two ways, straight line distance between initial and final actuator tip position and percent strain at the actuator surface. Again, the neutral position is defined as the static position of the actuator tip with zero electric field and zero external load. The percent strain was calculated by assuming that the actuator has constant curvature at the beginning and end of the electrical cycle. Bar-Cohen and Leary (2000) showed that this constant curvature approximation is valid, and the author's observations also support its use. The radius of curvature ρ was determined using the actuator tip position (X_t, Y_t) relative to the fixed end and the zero deflection / zero slope boundary condition at the fixed end. The relationship between ρ, X_t, and Y_t is described by the equation of a circle with its center at $(-\rho, 0)$, which, solved for ρ becomes

$$\rho = \frac{1}{2X_t}(X_t^2 + Y_t^2) \tag{4.15}$$

for the case in which the straight actuator is parallel to the y-axis. The strain ϵ_s at the surface of the actuator can be determined from the radius of curvature using the relation $\epsilon_s = -t_a/2\rho$, where t_a is the actuator thickness. The strain energy in the actuator was also calculated using the constant curvature approximation. In this paper, for the sake of comparison, we will consider a straight actuator to have zero strain energy. In this case, the strain energy in the actuator is (Shigley and Mischke, 1989)

$$U = \frac{EIL_{free}}{2\rho^2}, \tag{4.16}$$

where E is the elastic modulus (0.1GPa was used in this chapter), I is the area moment of inertia of the actuator's cross section, and L_{free} is the free length of the actuator.

To verify that the changes in neutral position discussed in this paper can be considered 'permanent,' an electrical input that causes a change in neutral position was applied

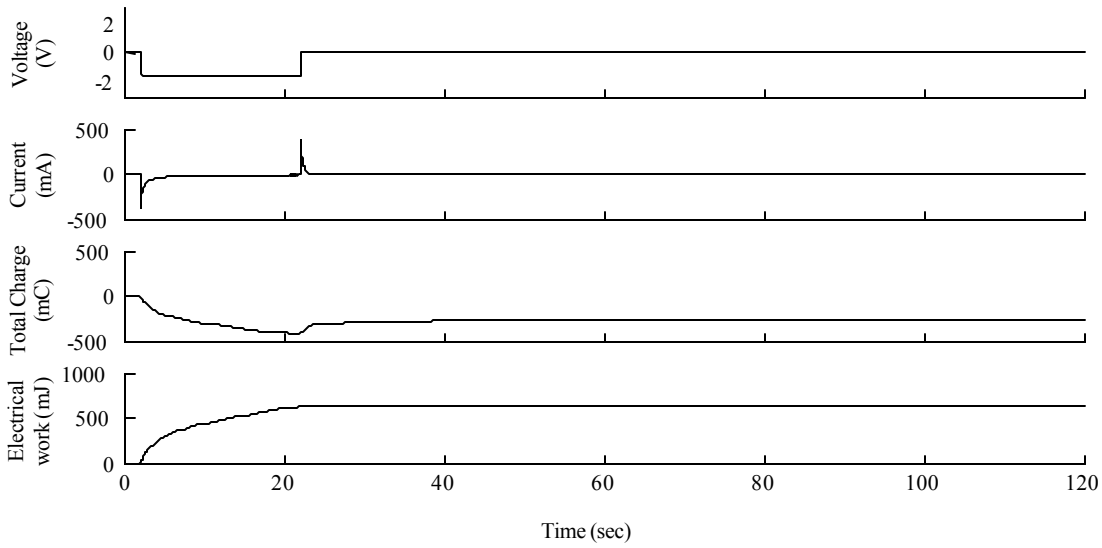

Figure 4.11: Example of a voltage pulse input.

to an IPMC actuator. The actuator was observed using a video camera for four hours after the electrical cycle. During this observation period, the electrodes were held at electrical ground, and the actuator was kept hydrated by brushing deionized water on it at approximately two minute intervals – frequently enough that the actuator surface remained wet. After the initial mechanical relaxation, which occurs within approximately 30 seconds after the electrodes are grounded, no further relaxation was observed. The absence of further relaxation indicates that the change in neutral position can be considered permanent, hence the term "electrically induced permanent strain."

4.3.3 Effect of change in actuator length

The effects of actuator length and input polarity on the permanent strain phenomenon were explored by applying 30 second long voltage pulses to three different length actuators, 18, 23, and 27mm free length. An example of the electrical input and response, as well as the charge delivered and electrical work done by the power source is shown in Figure 4.11. In most cases, the magnitude of the permanent strain increased with actuator length. This relationship held true, regardless of whether the change in neutral position was expressed in terms of percent strain at the actuator surface or as the straight line distance at the actuator tip. Figure 4.12 contains a plot of the change in neutral position for all three actuator lengths with $\pm$2V, 30 second long pulses.

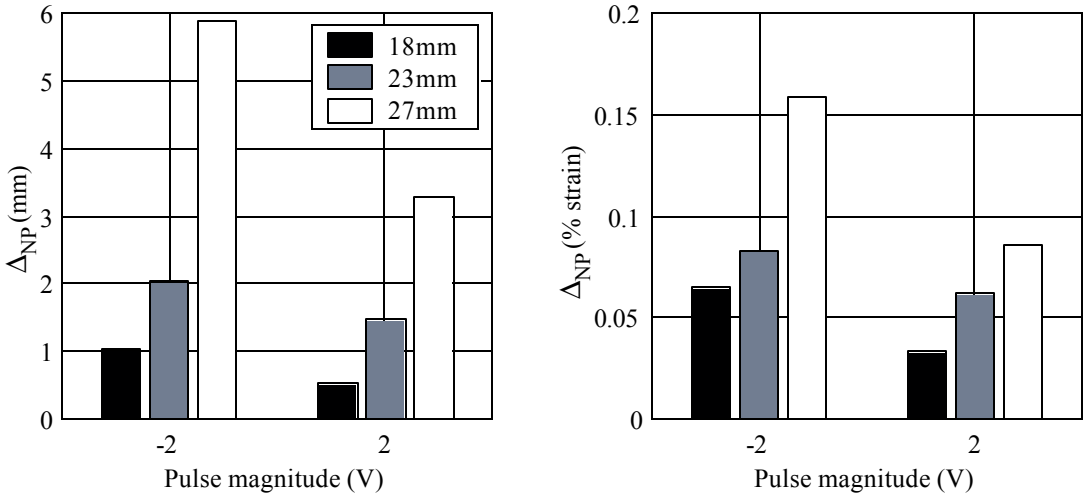

Figure 4.12: Change in neutral position for 18, 23, and 27mm free length actuators with ±2V x 30 sec pulse inputs.

4.3.4 Voltage pulse input

To investigate the effects of voltage pulse magnitude, 20 second long pulses with magnitudes ranging from ±0.5V to ±1.75V (in 0.25V increments) were applied to a 29mm free length actuator. The results are shown in Figure 4.13. In general, the change in neutral position increased as the magnitude of the voltage pulse was increased. The ±0.5V and ±0.75V data points did not follow this trend as closely as the others, but the trend did appear in other, similar experiments. Another trend that can be seen in Figures 4.12 and 4.13 is that Δ_{NP} is larger when the pulse magnitude is negative. The actuators start out with an initial curvature, which we have attributed to the manufacturing process. In the experiments presented in this paper, a negative electrical signal corresponds to an induced curvature opposite the initial curvature. In this case, "induced curvature" refers to the motion when the input is first applied, not the relaxation phase of the motion.

The next experiment was to vary the duration of ±2V pulses (15, 30, and 45 sec pulses were used) and observe the resulting changes in the neutral position. Figure 4.14 shows Δ_{NP} versus pulse length for a 29mm free length actuator. Again, the negative electrical signal resulted in a larger Δ_{NP}. Also, the largest Δ_{NP} occured with the 30 second long pulse, indicating that, if one wishes to maximize (or minimize) Δ_{NP}, input shape/duration should be considered.

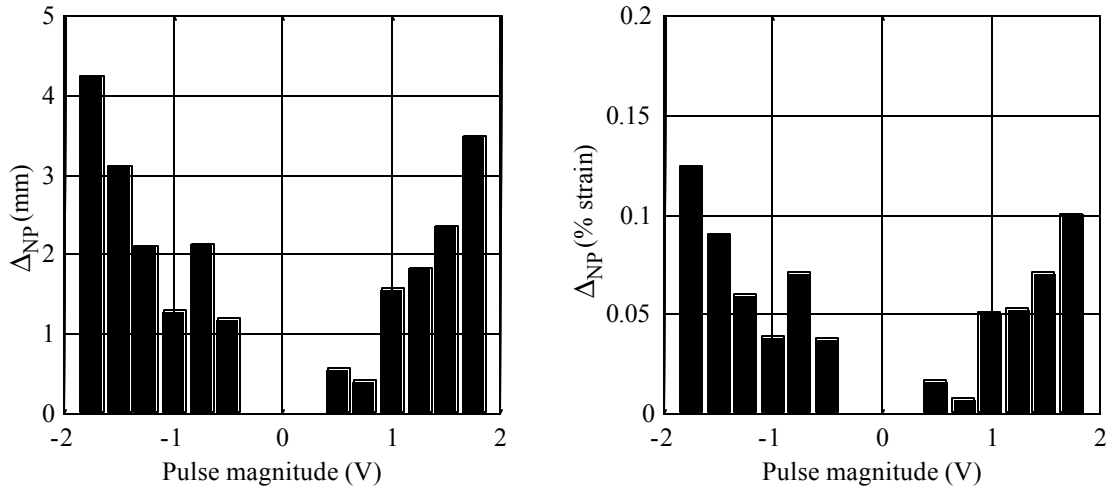

Figure 4.13: Change in neutral position for 29mm free length actuators with 20 sec voltage pulses with various magnitudes.

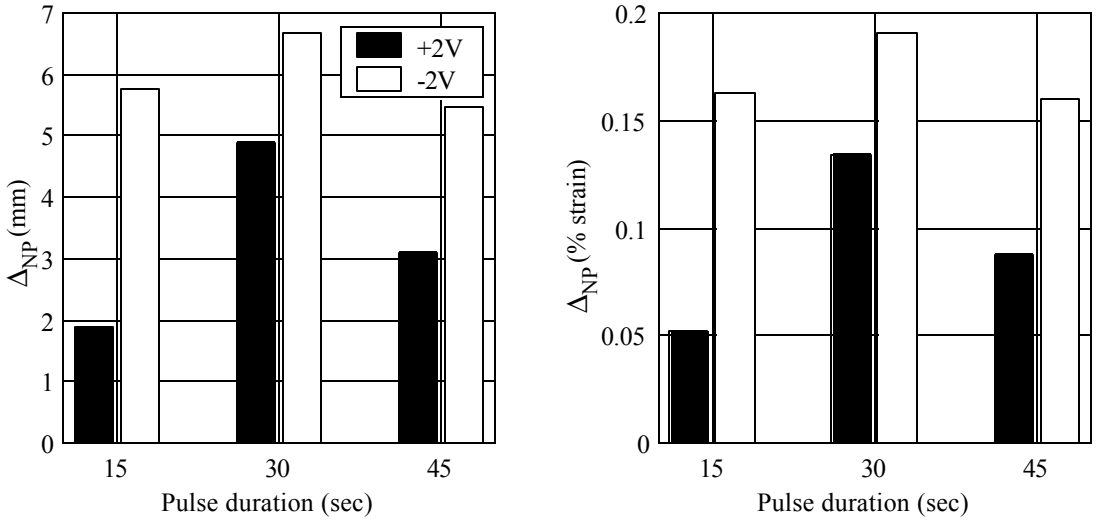

Figure 4.14: Change in neutral position for 29mm free length actuators with $\pm$2V voltage pulses with 15, 30, and 45 second durations.

Table 4.3: Electrical work, maximum charge, and change in neutral position with 20 second long ±1.5V and ±20mA pulse inputs applied to a 29mm free length actuator.

input	Q_{max} (mC)	W_E (mJ)	Δ_{NP} (mm)	Δ_{NP} (% strain)
+1.5V	380	570	2.4	0.070
-1.5V	419	630	3.1	0.091
+20mA	393	556	3.5	0.094
-20mA	394	523	4.0	0.10

4.3.5 Current pulse input

To further investigate the effects of input shape on the change in neutral position, 20 second long ±10mA and ±20mA current pulses were applied to a 29mm free length actuator. A sample electrical response is shown in Figure 4.15, and Δ_{NP} versus pulse magnitude is shown in Figure 4.16. Once again, the negative electrical input resulted in a greater Δ_{NP}, and, as expected, the ±20mA pulses resulted in greater Δ_{NP} than the ±10mA current pulses.

To compare current pulse response with voltage pulse response, we consider W_E and Q_{max} from the 29mm free length actuator experiments described in sections 4.3.4 and 4.3.5. The ±20mA x 20 second tests have values of W_E and Q_{max} that are similar to the ±1.5V x 20 second tests (see Table 4.3), so the electrical inputs can be considered, in a sense, similar. The corresponding changes in neutral position are also similar, with slightly higher values corresponding to the current pulse inputs. However, a significant difference between the responses resulting from the two types of inputs is in the peak deflection. Figure 4.17 contains plots of the tip position throughout the electrical cycle for the four inputs – the peak deflections corresponding to the current inputs are noticeably smaller.

4.3.6 Restrict initial deflection

All the experiments described so far were performed with no restriction on the motion of the actuator tip. To determine whether or not Δ_{NP} is somehow dependent on the initial actuator motion, the following test was conducted. A nylon screw was placed near the actuator tip to restrict its initial motion. The distance between the screw and the actuator tip was the permitted initial deflection. A 23mm free length actuator was given 20 second

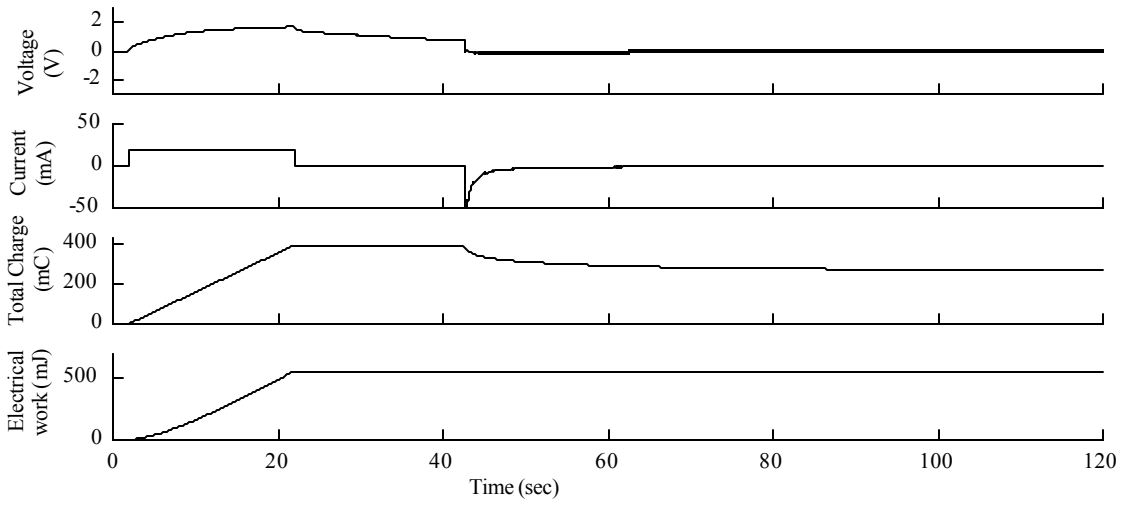

Figure 4.15: Example of a current pulse input.

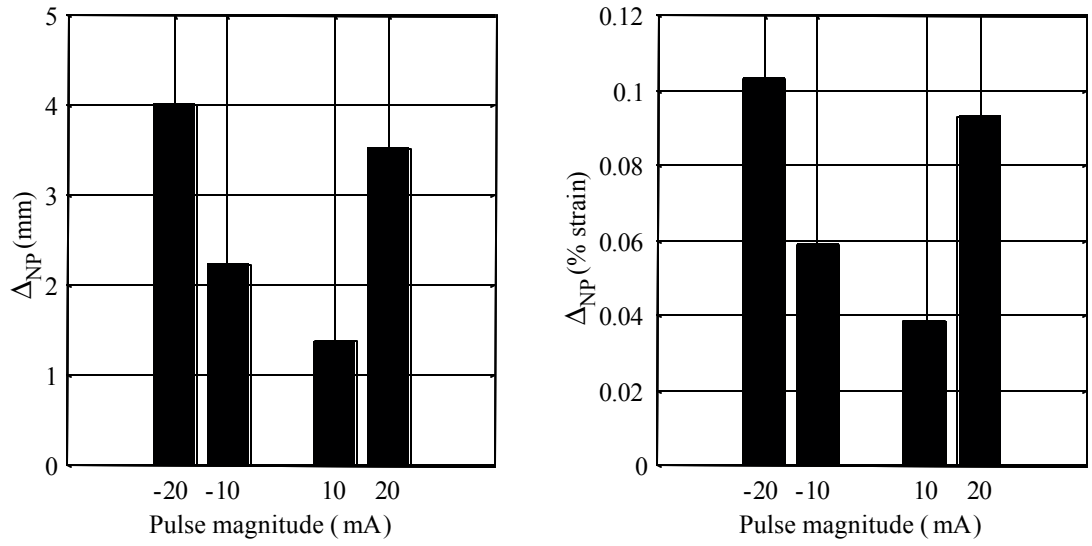

Figure 4.16: Change in neutral position for 29mm free length actuators with $\pm$10mA and $\pm$20mA x 20 sec current pulses.

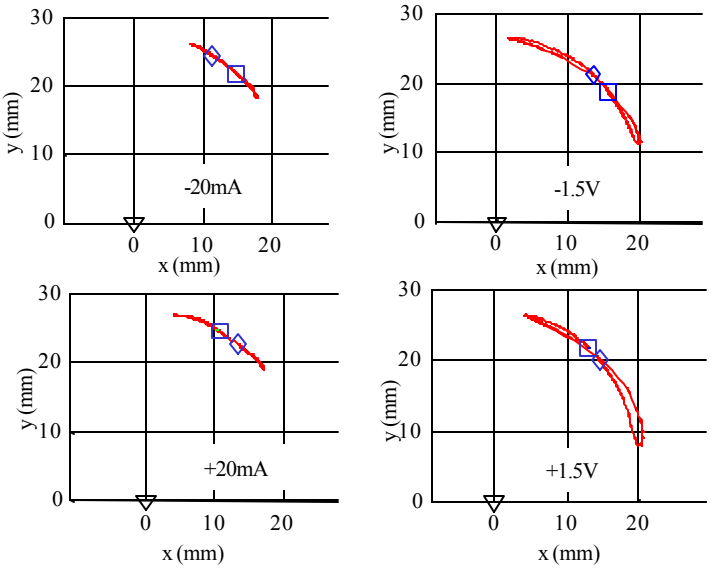

Figure 4.17: Tip trajectory of 29mm free length actuator with ±1.5V voltage pulses and ±20mA current pulses. Initial positions are marked with diamonds – final positions are marked with squares.

long 1.5V pulses, causing an initial motion (when permitted) toward the screw. This test was performed for a range of distances between screw and actuator tip, from 0mm to 10mm. At 10mm the actuator no longer touched the screw during the initial deflection. Δ_{NP} versus permitted initial deflection is plotted in Figure 4.18. Negative voltage pulses were applied before the 7.5mm and 10mm tests, because the actuator's static curvature had become rather large due to the repeated positive voltage pulses. It is interesting to note that the greatest change in neutral position occured in the tests immediately following a negative voltage pulse. This observation suggests that the actuator exhibits memory and/or initial condition dependence in its response. This issue did not surface in the previous experiments because each test was performed in an order such that each input was the opposite polarity of the previous input. Another conclusion that can be drawn from this experiment is that an initial actuator tip motion is not required for the permanent strain phenomenon to occur.

4.3.7 Electromechanical analysis

In an effort to relate the permanent strain phenomenon to the electrical response, W_E and Q_{final} are considered, along with Δ_ϵ, the change in surface strain. For solid-state actuators, it is natural to compare electrical displacement (charge) to mechanical displacement

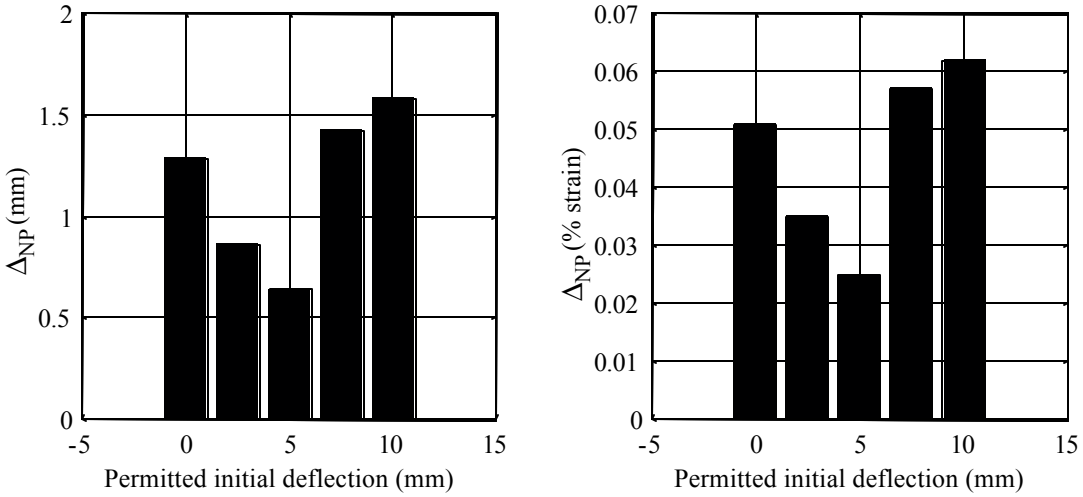

Figure 4.18: Change in neutral position for a 23mm free length actuator with 20 second long 1.5V pulse inputs and restricted initial deflection.

(strain). With piezoelectric materials, this relationship is described by the "G" constant (Piezo Systems, 1998), and is typically expressed in terms of strain developed in a particular direction divided by charge density. Applying this concept to the permanent strain phenomenon, we define the term

$$g_{ps} = \frac{\Delta_\epsilon}{(Q_{final}/L_f)}, \tag{4.17}$$

which has units of strain/(charge/length). Figure 4.19 shows g_{ps} for the 20 second long voltage pulses and 20 second long current pulses that were applied to the 29mm free length actuator. Inspection of Figure 4.19 reveals that, except for the $\pm$0.5V and $\pm$0.75V data points, the value of g_{ps} is nearly constant, even though the change in neutral position varies significantly with pulse magnitude. The fact that g_{ps} is nearly constant suggests that the permanent strain phenomenon is closely related to the total electrical charge delivered to the actuator. To further investigate this idea, a single cycle of a 0.025Hz 20mA (0-peak) current square wave was applied to a 29mm free length actuator to see if there would be a change in neutral position with zero net charge delivered to the actuator. Figure 4.20 shows the input and related electrical quantities. No change in neutral position was observed, supporting the conclusion that the permanent strain phenomenon is charge-driven. The noncomformity of the $\pm$0.5V and $\pm$0.75V data points in Figure 4.19 is partially explained by the fact that any errors introduced by the resolution of the camera / motion tracking software combination

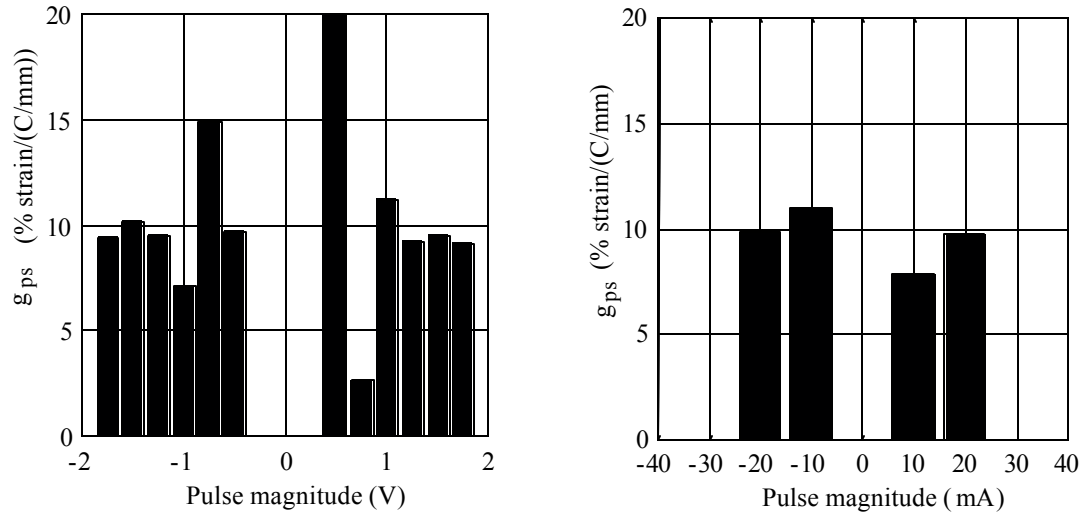

Figure 4.19: Change in neutral position divided by charge per unit length for 20 second pulses applied to a 29mm free length actuator

and by DC offsets in the electronics have a greater effect on the analysis of the experiments with small inputs.

The value of g_{ps} is plotted in Figure 4.21a for the experiment with 1.5V pulses of various durations, and its value decreases with increasing pulse duration.. A portion of Q_{final} results from the fact that ionic polymer actuators will conduct current at DC, leading to a direct dependence of Q_{final} on the pulse duration. It is reasonable to consider whether or not this DC current is the primary reason that the magnitude of g_{ps} decreases with increasing pulse duration. To investigate, the total charge from the DC current (voltage pulse duration times the estimated DC current) is subtracted from Q_{final} before calculating g_{ps}. A value of 5mA, estimated by inspecting the current time histories, is used for the DC current, and the resulting g_{ps} versus pulse duration is plotted in Figure 4.21b. The dependence of g_{ps} on pulse duration is still apparent, indicating that the relation between the permanent strain magnitude and Q_{final} is not independent of pulse duration, even when the charge related to the DC current is removed from the calculation of g_{ps}.

Another approach to analyzing the relationship between the permanent strain and the electrical response is to consider energy. For the experiments described in this paper, we examined the ratio of the change in strain energy associated with the change in neutral position to the total electrical work done on the actuator. Typical values were on the order

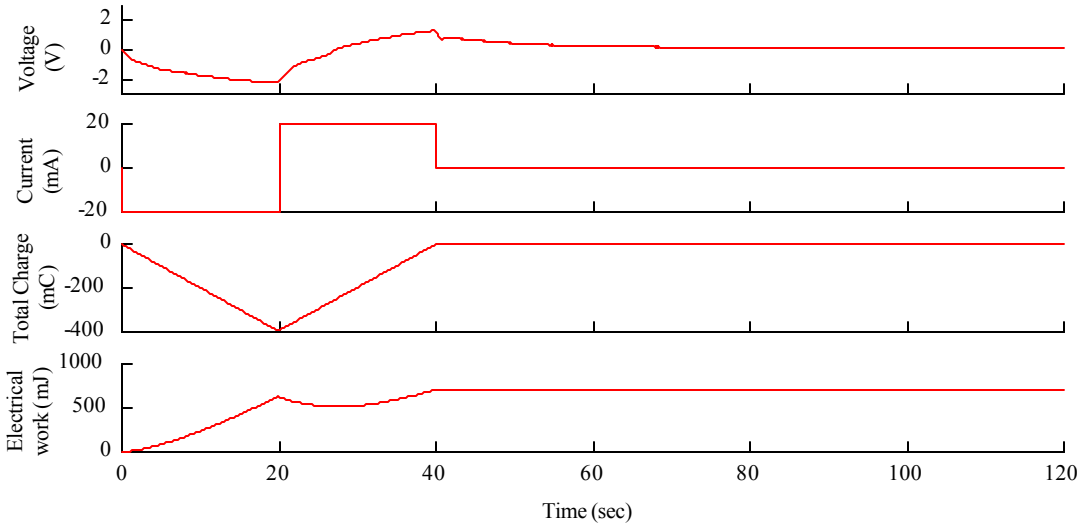

Figure 4.20: Electrical response with one cycle of a 20mA (0-peak) 0.025Hz square wave applied to a 29mm free length actuator.

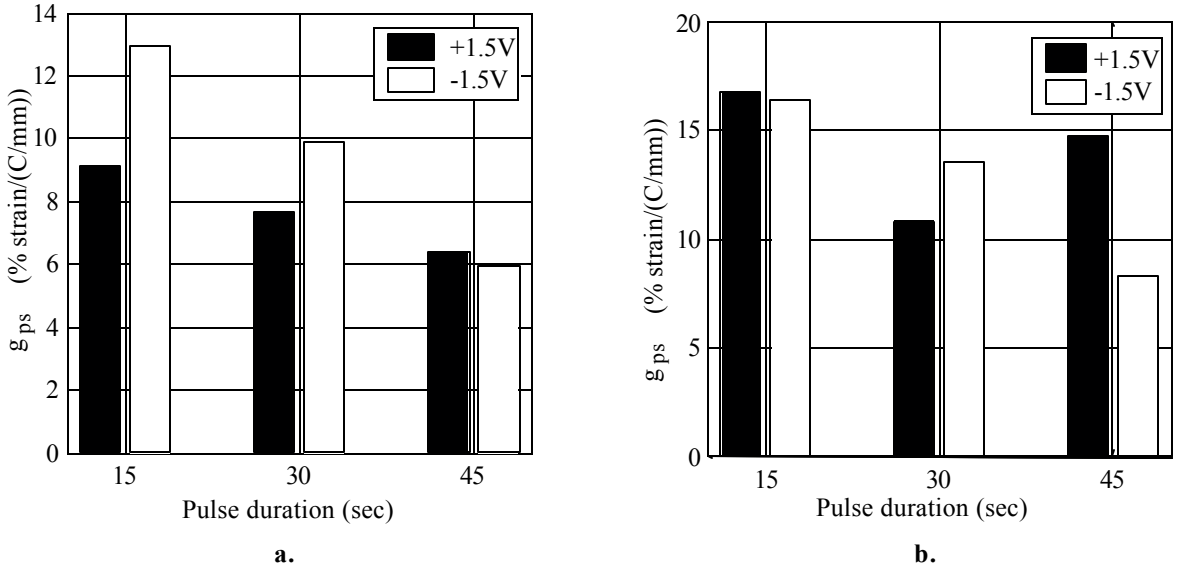

Figure 4.21: Change in neutral position divided by charge per unit length for ±1.5V pulses of various lengths applied to a 29mm free length actuator: a) DC current included in total charge, b) DC current times pulse duration subtracted from total charge.

of 5 μJ/J. Only a small portion of the electrical energy delivered to the actuator can be attributed to the permanent strain – most of the energy is dissipated, whether electrically or mechanically.

4.4 Chapter Summary

A comparison of ionic polymer transducers to piezoceramic and PVDF transducers, considering the cantilevered-bender configuration only, showed that when used as actuators, their energy densities are within an order of magnitude of one another. The primary advantages of ionic polymer transducers are that actuation requires only a small electric field and that they are better suited for use in aqueous environments. Used as sensors, ionic polymers exhibit greater charge sensitivity, three orders of magnitude greater than PVDF and two orders of magnitude greater than PZT when measuring charge with a force input. A disadvantage of ionic polymer transducers is the strong frequency dependence of the electromechanical coupling.

In the process of experimenting with ionic polymer transducers, an interesting behavior was observed. With certain inputs, ionic polymer actuators exhibit a nonlinear phenomenon that has been called 'electrically induced permanent strain.' Once the electrical terminals are returned to electrical ground, the actuator does not return to its starting position. An initial investigation suggests that the difference between the initial and final position is related to the total electrical charge delivered to the actuator between times when the electrodes are grounded.

Chapter 5

Feedback Control Using Ionic Polymer Sensors and Actuators

One of the goals of this work was to demonstrate feedback control of a system that uses ionic polymer transducers for both sensing and actuation. This chapter describes an experiment in which feedback control was applied to a rotary device that was driven by multiple ionic polymer actuators. The displacement of the device was measured using an additional ionic polymer transducer. The Chapter 2 modeling technique, along with the paramters identified in Chapter 3, were employed to model the device. After the model was reconciled against the experimental open-loop response of the system, it was used to design the compensator and predict the closed-loop response. The compensator was implemented experimentally using a DSP, and feedback control did yield some improvements in the device's ability to track sinusoidal inputs; however, these improvements were only realized in a narrow frequency range.

5.1 System Design

Initial efforts were directed towards the development of an ionic polymer sensor/actuator. Such a device would provide an elegant, convenient, and compact means by which to obtain a collocated sensor signal. Two attempts were made to fabricate a sensor/actuator, and they were both unsuccessful. Despite their lack of success, these attempts are interesting and will be briefly described. The device shown in Figure 5.1 a was fabricated from a single piece of Nafion and had two parallel pairs of electrodes. The narrow regions between

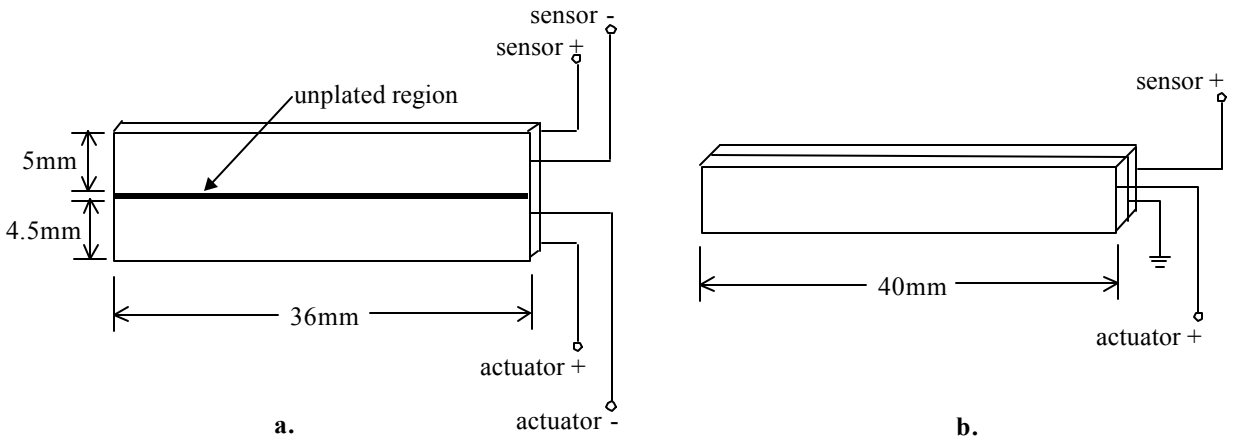

Figure 5.1: Attempted sensor actuator geometries.

adjacent electrodes were created by clamping the polymer between two glass rods during the plating process. The glass rods effectively masked these portions of the polymer surface, resulting in two separate pairs of electrodes – one for sensing and one for actuation. The device illustrated in Figure 5.1b consisted of two ionic polymer transducer strips that were attached to one another near the free end using polyester thread. At the clamped end, a piece of gold foil was clamped between the two transducers to provide electrical contact with the center electrodes. The center electrodes were connected to electrical ground, and one of the outer electrodes was used to provide an actuation signal, the other was used for sensing.

To test the two sensor/actuators, a random voltage signal, of magnitude great enough to cause visible motion of the transducer tip, was applied to the actuator electrodes. The sensor electrodes were connected to the short-circuit current measurement circuit described in Chapter 4, and the circuit output was measured. In both cases, the op-amp in the circuit saturated, indicating that the current was more than 100 μA, the maximum current the circuit could measure. The short-circuit current from a similarly sized mechanically excited polymer sensor would have been on the order of 10 μA. This result indicated that the short-circuit current from the sensor electrodes was dominated by the electrical signal applied to the actuator. To confirm the lack of 'useful' information in the signal from the sensor, the open-circuit voltage of the sensor electrodes was measured while a random voltage was applied to the actuator electrodes. The open-circuit condition was approximated by connecting the sensor electrodes to an AD620AN instrumentation amplifier, providing a

high input resistance. The frequency response between the sensor open-circuit voltage and the applied actuator voltage was measured using a Tektronix FFT analyzer with both free and blocked mechanical boundary conditions. The measured frequency responses for the configurations shown in Figures 5.1a and 5.1b are plotted in Figures 5.2a and 5.2b, respectively. The fact that the blocked and free end frequency responses for each actuator are

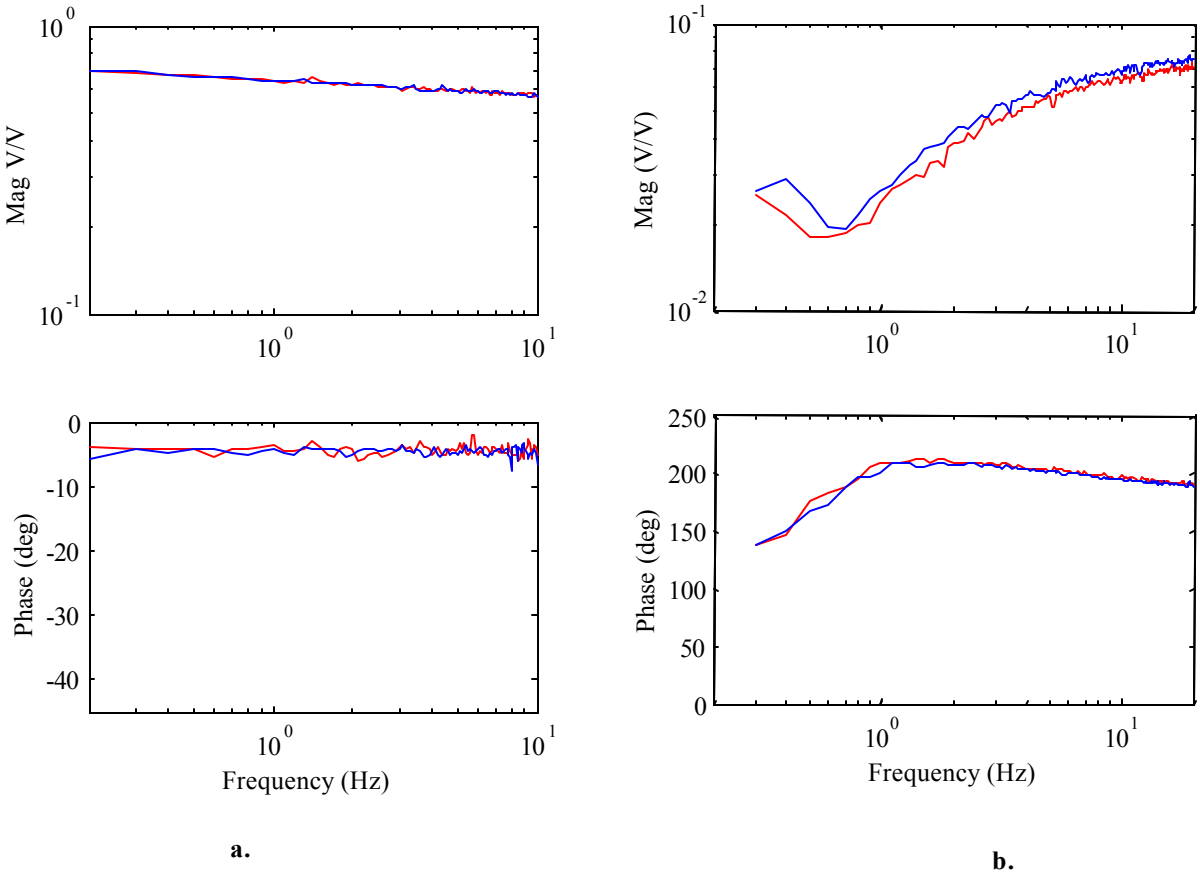

Figure 5.2: Frequency response – Open-circuit voltage over input voltage: a) Figure 5.1a device, b) Figure 5.1b device.

nearly identical confirms that the sensor signals were dominated by electrical feed through.

The failure of the attempted ionic polymer sensor/actuators compelled the author to design a device that would both mechanically couple and electrically isolate individual ionic polymer sensors and actuators. Figure 5.3 contains a photo of the resulting mechanism, which, in the remainder of this document, will be referred to as the 'polymer motor.' The outer rim of the rotating element is a laminate consisting of two 3mm wide layers of 0.05mm

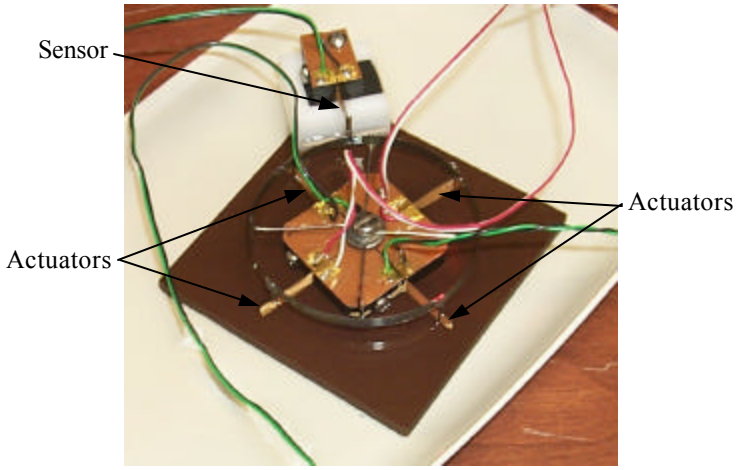

Figure 5.3: Polymer motor.

thick steel shim stock, bonded with cyanoacrylate adhesive. To provide mechanical coupling with the polymer benders, ten 1cm long pieces of 0.64mm diameter stainless steel wire were glued to the outside of the rim in pairs (tacked in place with cyanoacrylate – final bonding with epoxy), parallel to the axis of rotation. The spacing between the pieces of wire in each pair is approximately 0.3mm, just enough space that the polymer transducers can freely slide through the gap in the radial direction. For four of the pairs, one end of each piece of wire is flush with the top edge of the outer rim, so there is approximately 7mm below the rim to 'capture' the polymer actuators. The fifth pair, used for the sensor polymer, was glued with the ends of the wire flush with the bottom edge of the rim. With the layer of cyanoacrylate glue between each piece of wire and the rotor rim, each piece of stainless wire is electrically insulated from the rim. The 'spokes' of the rotating element were also made from 0.64mm diameter stainless wire and glued (with epoxy) to the both the outer rim and to the stainless steel thrust washer in the center. The thrust washer rests on a Teflon flange bearing and is guided radially by a stainless shoulder screw that is screwed to the phenolic base. The electrodes are pieces of gold foil glued to phenolic. To keep the actuators hydrated, the motor was partially submerged in deionized water. The water level was high enough to keep the actuators immersed, but below the bottom edge of the rim in order to minimize added damping. Deionized water was brushed on the sensor polymer frequently enough to keep the transducer surface wet.

The original intent was to use three of the submerged transducers as actuators and one as a sensor; however, the sensor signal was not usable. Even though the polymers were

submerged in deionized water, which has very low conductivity, this configuration exhibited enough electrical feed through that the portion of the sensor signal corresponding to the motor's motion was buried by the feed through of the actuation signal. To get around this issue, the sensor polymer was mounted above the rim (out of the water), and the remaining electrically conductive paths between the sensor and the actuation signal were eliminated.

To model the motor, the rotation inertia of the rotor was calculated from the dimensions, densities, and locations (with respect to the axis of rotation) of the individual components, yielding a value of 8.44E-7kg $\cdot$ m^2. To account for the glue, the calculated mass of the rotor (1.72g) was subtracted from the total rotor mass (2.14g), which was measured using a Mettler Toledo model AB204 precision balance. In calculating the inertia of the glue, it was assumed that all the additional mass was located at the radius of the outer rim. The total rotor inertia, including glue, was estimated as 12E-7kg $\cdot$ m^2.

Since applied voltage is used as the input to the motor, a convenient initial step in using the Chapter 2 transducer model for the polymer motor is to rearrange the mechanical and electrical variables in equation (2.30) such that current and force are the dependent variables, and voltage and velocity are the independent variables, resulting in a transducer model with the form

$$\begin{Bmatrix} i \\ \\ f \end{Bmatrix} = \begin{bmatrix} g_{11} & g_{12} \\ \\ g_{21} & g_{22} \end{bmatrix} \begin{Bmatrix} v \\ \\ \dot{u} \end{Bmatrix}. \tag{5.1}$$

In terms of equivalent-circuit elements, the matrix elements in equation (5.1) are

$$\begin{aligned} g_{11} &= \tfrac{R_{dc}+Z_p}{R_{dc}Z_p} \qquad g_{12} = -\tfrac{NZ_{m1}}{Z_p} \\ g_{21} &= \tfrac{NZ_{m1}}{Z_p} \qquad g_{22} = Z_{m1} + Z_{m2} \end{aligned} . \tag{5.2}$$

Note that the assumptions in equations (2.31) and (2.32) have been applied.

The equation of motion for the motor rotor,

$$T = I_m \ddot{\theta}, \tag{5.3}$$

with T representing the torque exerted on the rotor, I_m the mass moment of inertia of the rotor, and θ the clockwise rotation of the rotor, is used to provide a relationship between force and velocity. Figure 5.4b shows how the transducer model sign conventions defined in Chapter 2 apply to the polymer motor. Recalling that f was defined as the force acting *on*

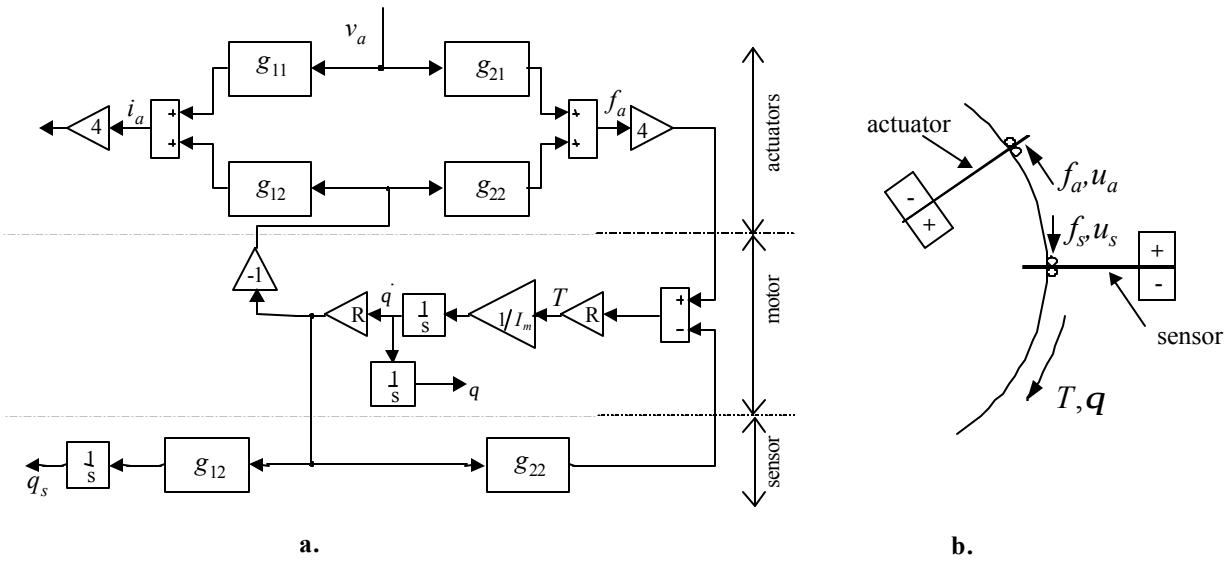

Figure 5.4: Diagram of polymer motor: a) Block diagram, b) Sign conventions and polarities.

the polymer transducer, and, combining equations (5.1) and (5.3) with the information in Figure 5.4b, one can create the block diagram of the polymer motor shown in Figure 5.4a. Transfer functions between the various quantities that appear in Figure 5.4a can be calculated using Mason's gain rule (Dorf, 1989). Two particularly important relations are the transfer function between input voltage and motor angular displacement

$$\frac{\theta}{v_a} = \frac{4Rg_{21}}{s(I_m s + 5R^2 g_{22})} \tag{5.4}$$

and the transfer function between the motor displacement and the charge from the sensor polymer

$$\frac{q_s}{\theta} = Rg_{12}. \tag{5.5}$$

The subscripts s and a have been added to the electrical variables to distinguish between sensor and actuator quantities.

5.2 Model Reconciliation

To validate the model of the polymer motor, experimental data are compared to the response simulated using equation (5.4). To facilitate measurement of the motor's displacement, a small aluminum foil tab was attached to one of the rotor spokes. A Polytec laser vibrometer was used to measure the linear displacement of the foil tab, and the linear displacement was

converted to angular displacement by dividing by the distance between the measurement point and the center of rotation. Input signals were generated using a Tektronix FFT analyzer and amplified by an HP power amplifier before being applied to the polymer motor.

Figure 5.5a contains displacement frequency responses (based on the laser vibrometer displacement measurements) with 0.4Vrms to 1.1Vrms 0-50Hz random signals applied to the motor. The input level was incremented by 0.1mVrms between each data set. Overlayed

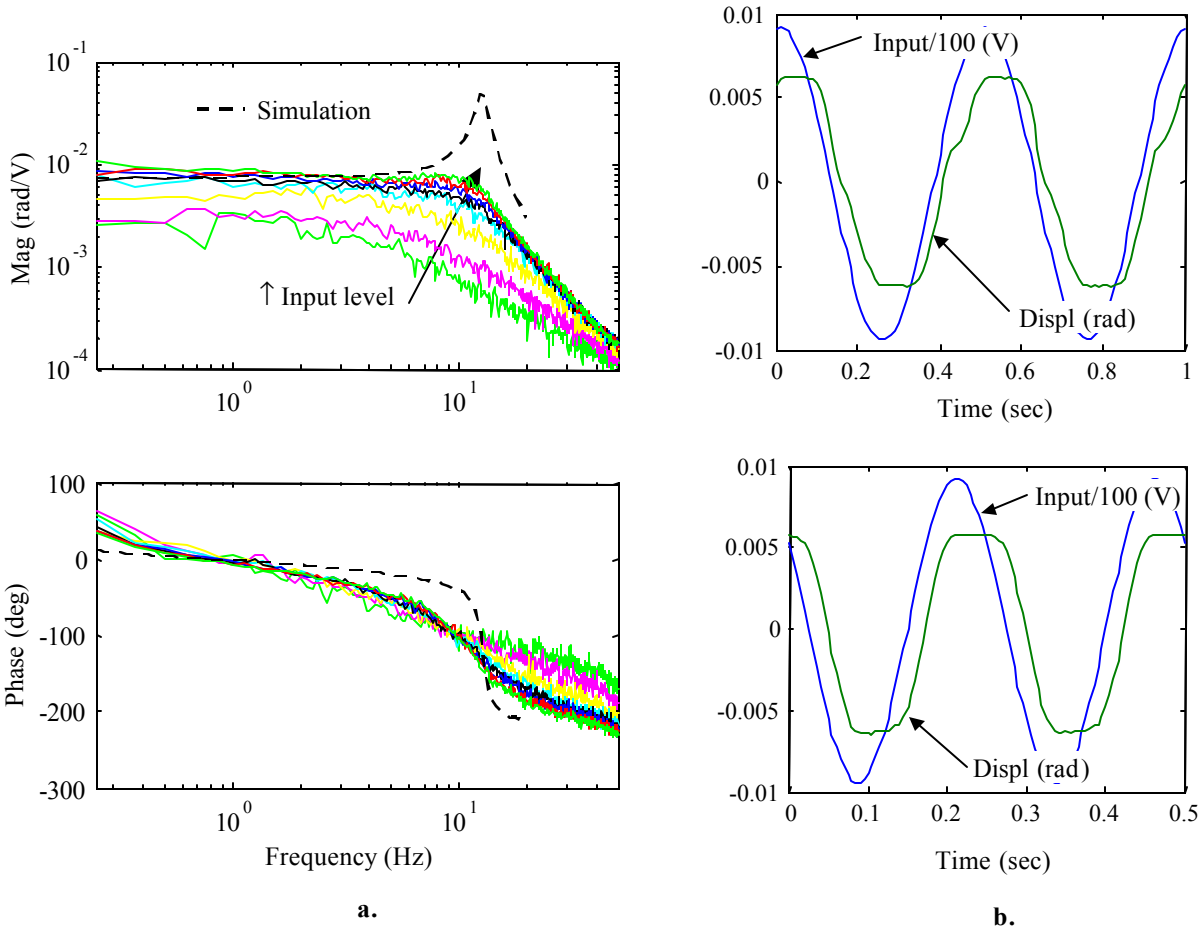

Figure 5.5: Open-loop motor response: a) Frequency domain response compared with simulated response, b) Time domain response with single frequency input (top: 2Hz input, bottom: 4Hz input).

is a plot of the simulated frequency response based on equation (5.4) and the transducer material parameters determined in Chapter 3. The polymer transducer dimensions (for sensor and actuators) were $L_{free} = 16$mm, $L_d = 12$mm, $L_t = 22$mm, and $w = 5$mm. At low frequencies, the match between the simulated and experimental response is reasonable;

however, there is significantly more damping in the experimental response. This mismatch is reasonable, considering that the motor model does not yet have a term that represents the damping added by submerging the polymers in water and by the friction in the motor pivot. Another important feature in the Figure 5.5a plot is the increase in motor response with increasing input level. This input level dependence in the motor response is attributed to Coulomb friction (commonly referred to as 'stiction') in the motor pivot. This idea is supported by the Figure 5.5b plots of the time domain response to a 2Hz and a 4Hz sinusoidal input. The flat 'tops' of the displacement plot indicate that once the velocity drops below a certain level, the motor stops, and it does not start moving again until the polymer actuators have exerted enough force to overcome the Coulomb friction. Another supporting observation is that, for input levels of 0.3mV and below, the motor displacement was insignificant (orders of magnitude lower than the plotted responses). At these low input levels, the actuators did not develop enough force to overcome the Coulomb friction.

To obtain a better match between the simulated and measured motor response, viscous damping was added to the motor model by modifying the Figure 5.4 block diagram as shown in Figure 5.6a. The resulting transfer function between input voltage and angular displacement becomes

$$\frac{\theta}{v_a} = \frac{4Rg_{21}}{s(I_m s + c_r + 5R^2 g_{22})}, \tag{5.6}$$

where c_r is the damping coefficient. The value of c_r was adjusted to obtain a good match between the simulated and experimental displacement frequency responses. These responses are plotted in Figure 5.6b with c_r=1E-4$\frac{\mathrm{N\cdot m\cdot sec}}{\mathrm{rad}}$, the value used in the remainder of this work. For the higher input levels, the agreement between the damping in the simulated and experimental frequency responses is reasonable.

The predicted natural frequency of the motor is slightly higher than the measured natural frequency. To compensate, the rotor inertia I_m was increased by 15% to a value of 13.8E-7kg $\cdot$ m^2. A likely explanation for the error in the predicted natural frequency is that the submerged polymer actuators must displace water when they are in motion, effectively increasing the mass of the actuators. Note that some discrepancy between model and experiment can also be explained by the performance variations observed in different ionic polymer transducers with identical dimensions, an issue mentioned earlier in this work. The transducer used in the parameter identification experiments described in Chapter 3 was manufactured in the same batch as those used for the polymer motor, which should reduce

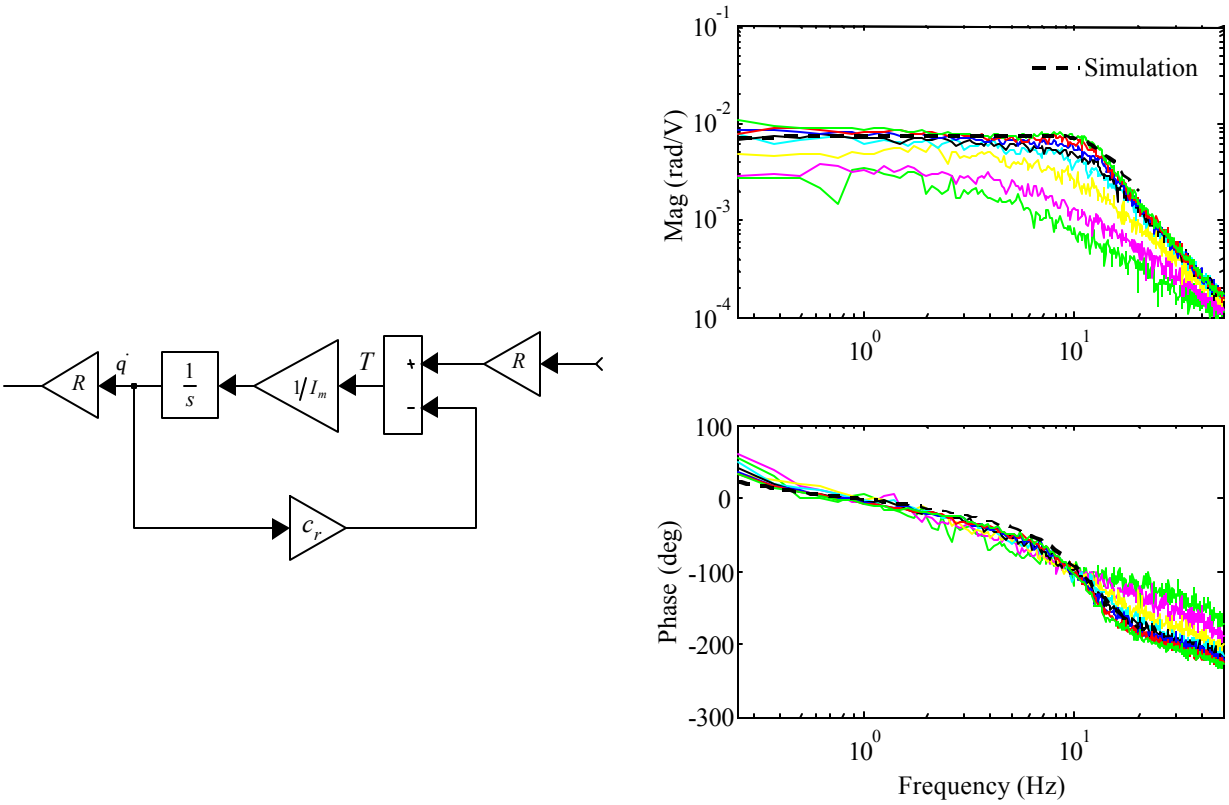

Figure 5.6: Addition of damping term to the motor model: a) block diagram, b) experimental and simulated frequency responses.

the deviations, but some variation is still expected. In addition, the identification experiments were performed in air. Although attempts were made to keep the transducer surface wet during the identification experiments, it is still possible that transducer performance is different when the transducers are fully immersed.

5.3 Compensator Design and Experimental Results

The motor output, for the purpose of the control experiments, was chosen to be -1 times the output voltage of the op-amp based charge amplifier circuit that was used to measure the short-circuit charge of the sensor polymer. In the 1 to 10Hz frequency range, this quantity follows the motor position with fairly constant magnitude and a moderate amount of phase lag. An expression for the relationship between the charge amplifier output and

the motor position is obtained by multiplying equation (5.5) by -1 times the charge amp transfer function, to obtain

$$\frac{v_o}{q_s} = \frac{sR_f}{sR_fC_f + 1}, \tag{5.7}$$

where R_f and C_f are the resistance and capacitance in the circuit's feedback loop, v_o is the charge amp output, and q_s is the charge to the positive electrode of the sensor polymer. For the experiments presented in this paper, the circuit component values were R_f=465k- and C_f=460nF, resulting in a corner frequency of 0.76Hz. The reason for multiplying the charge amplifier output by -1 becomes clear when equation (5.5) is expressed in terms of transducer material parameters and dimensions, resulting in the expression

$$\frac{q_s}{\theta} = -\frac{3RdtwY}{4L_d}. \tag{5.8}$$

The minus sign in equation (5.8) indicates that charge will be emitted *from* the positive sensor electrode with positive (clockwise) motor rotation, resulting in a negative voltage from the charge amplifier. In order for the charge amplifier output to closely correspond to motor rotation, it is multiplied by -1. Figure 5.7 contains a plot of the frequency response predicted by the model for $-\frac{v_o}{\theta}$ and comparisons of the charge amplifier output with the position measured using the laser vibrometer for 1 Hz and 5Hz 0.94V sinusoidal inputs applied to the motor. Note that, below 1Hz, the response of the polymer sensor / charge amplifier combination drops rapidly with decreasing frequency, mostly due to the fact that the charge amplifier acts as a differentiator below its corner frequency. A lower corner frequency would permit the polymer sensor to be used at frequencies below 1Hz; however, there are practical limits to how low the corner frequency can be set with 'reasonable' values for R_f and C_f. For this reason, along with those stated in the following paragraph, the experiments in this work were restricted to 1Hz and above.

Before proceeding, a brief discussion on the general nature of the observed polymer transducer response as it relates to the phase of the polymer motor frequency response is appropriate. Recall that, as mentioned in section 3.3, the sub-Hz behavior of the polymer actuators was somewhat inconsistent in that the steady-state force/displacement was often, but not always, in the opposite direction from the initial motion. In section 3.3.3, the case in which the steady-state response was in the opposite direction from the initial response was shown to correspond to a non-minimum phase system – a system with a zero in the right half of the s-plane. Because the out-of-phase portion of the actuator's response occurs

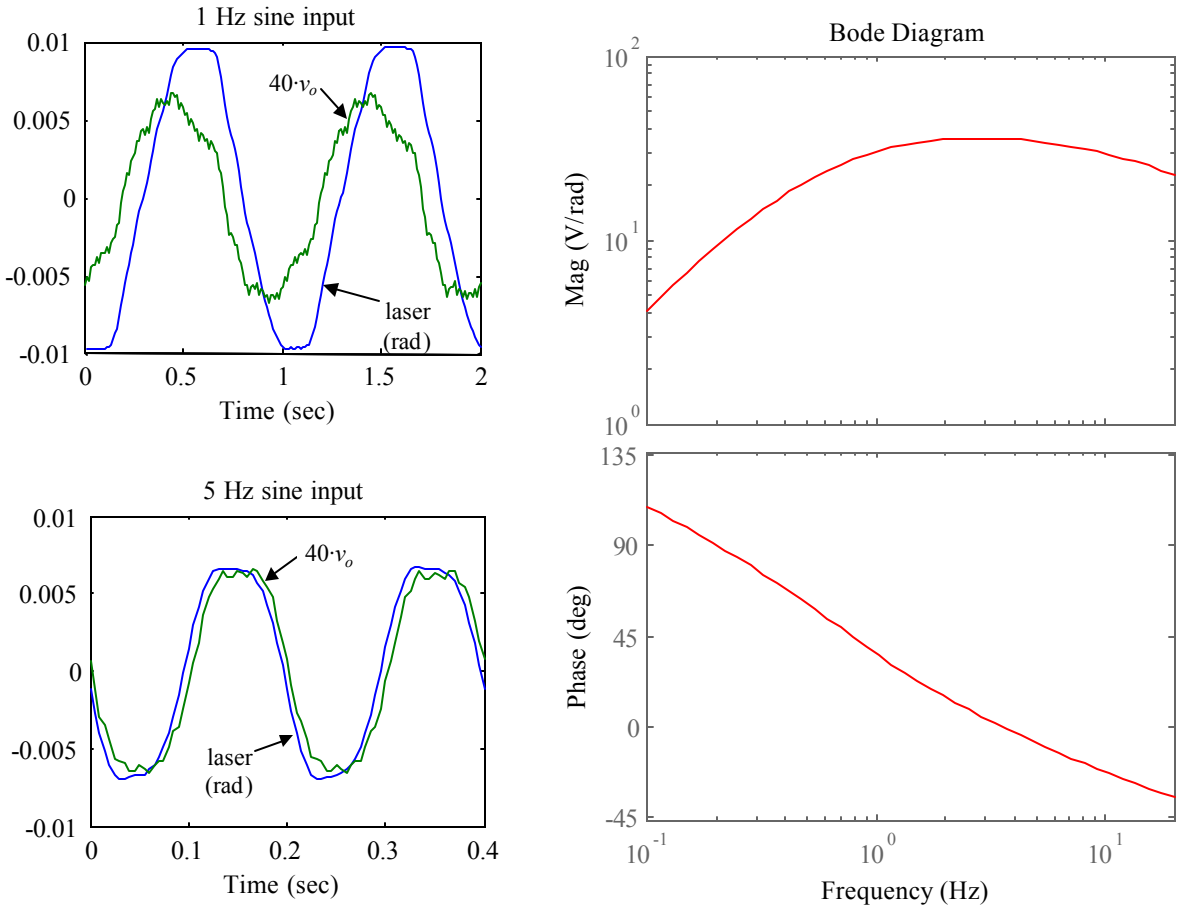

Figure 5.7: Polymer sensor with charge amplifier: predicted frequency response and time domain comparison to laser vibrometer based deflection measurement.

at very low frequencies (well into the 'relaxation' phase of the step response), this right half plane zero is at a very low frequency, 0.015Hz in the model. If this non-minimum phase behavior is considered in the control system design, the phase of the open-loop system will reach -180 degrees by 0.1Hz, limiting the achievable closed-loop bandwidth to the sub-Hz frequency range, a range in which the sensor/charge amplifier combination cannot provide an effective displacement signal. To circumvent this issue, the polymer transducer behavior is assumed to exhibit minimum phase behavior, with the caveat that the model may not accurately represent the physical system's behavior in the sub-Hz frequency range. This assumption was accommodated by fitting the transfer function used to represent the ionic polymer strain coefficient d to one of the minimum phase responses that was observed. A comparison of the predicted frequency response of $\frac{v_o}{v_a}$ for both the minimum phase and non-

minimum phase models is shown in Figure 5.8. Above approximately 0.5Hz, the response magnitudes overlay quite well, and the phase plots are 360 degrees apart, confirming that the minimum phase model can be used in cases where the sub-Hz response is unimportant. An

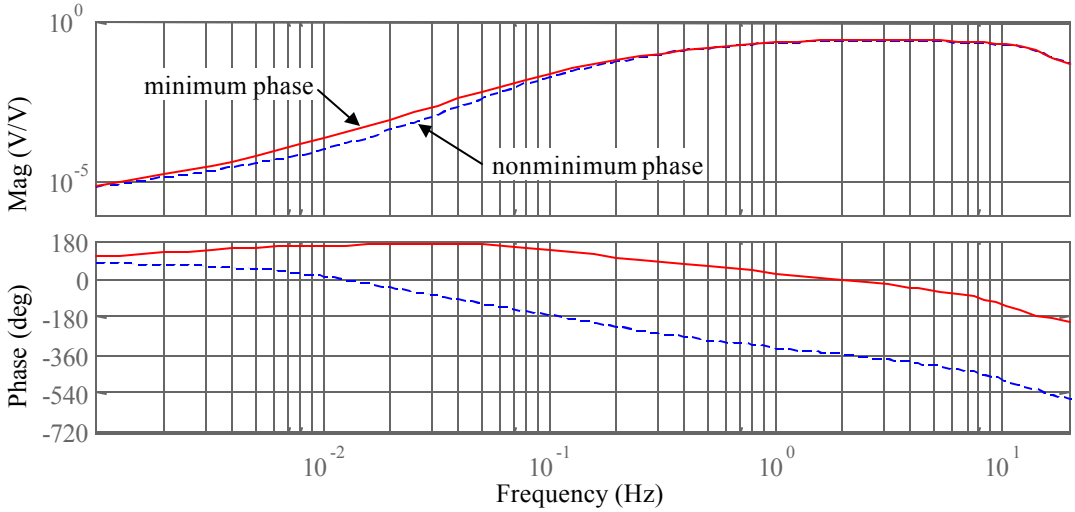

Figure 5.8: Predicted open-loop frequency response of the polymer motor/sensor/charge amp combination.

additional benefit of restricting the operation to frequencies above 1Hz is that the polymer transducers appear to behave more consistently in this frequency range, which will lead to a better match between the predicted and experimental responses.

5.3.1 Compensator Design

The compensators used in this work were formulated using a combination of classical control design techniques. One technique, commonly referred to as the frequency-response design method (Franklin et al., 1994), focuses on modifying the open-loop frequency response with the compensator in order to achieve the highest possible open-loop gain in the frequency range of interest while maintaining acceptable gain and phase margins. In this work, there are no specified stability margins, and the goal is simply to explore the performance limits of the polymer motor and sensor in terms of how well the charge amplifier output follows sinusoidal reference signals. The root-locus method (Franklin et al., 1994) is also used to gain insight into effects that various compensators will have on the closed-loop performance.

Figure 5.9 contains a block diagram showing the configuration of the closed-loop sys-

tem and the open-loop frequency response $\frac{v_o}{v_a}$ for the 0.1 to 20Hz frequency range. Because

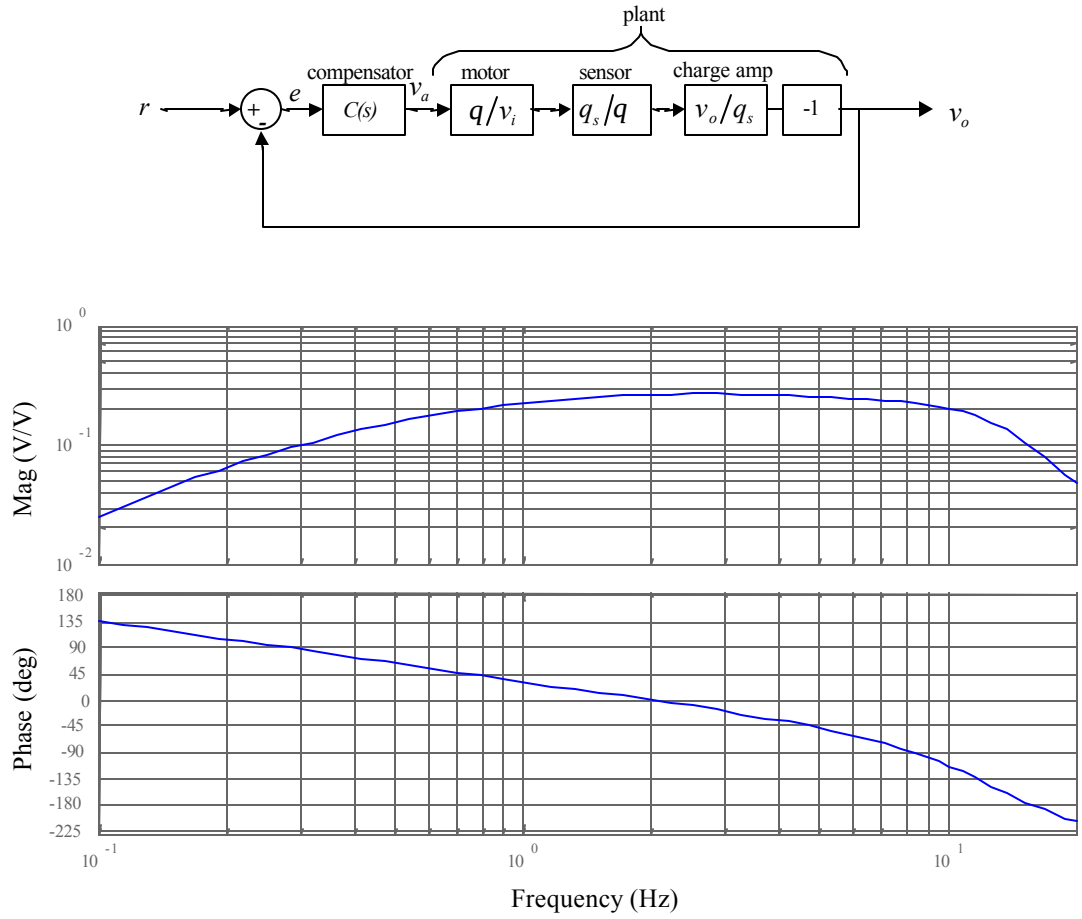

Figure 5.9: Closed-loop system block diagram and predicted open-loop frequency response $\frac{v_o}{v_a}$.

of the charge amplifier, the magnitude of $\frac{v_o}{v_a}$ is relatively low below 1Hz. If one were attempting to increase the low-frequency gain, in order to track low-frequency signals or reduce steady-state error, it would be natural to consider a lag compensator, or perhaps an integrator for $C(s)$. In this case, however, we are not interested in sub-Hz tracking or steady-state error because of the inconsistent sub-Hz polymer transducer behavior, which was discussed earlier. Also, the polymer sensor/charge amp combination is not capable of providing a reliable low-frequency signal more than a decade or so below its corner frequency. At these low frequencies, the charge amp output will be dominated by noise, and at DC, the output will be the DC offset of the op-amp circuit, neither of which will correspond to the motor position. For these reasons, lag compensation and integral control will not be

considered further. Note that Kothera and Leo (2002) successfully used integral control to improve the step response of a cantilevered ionic polymer actuator operated in air. Their success does not imply that integral control is appropriate for the control problem in this work for two reasons. First, they used a laser vibrometer as a feedback sensor. Unlike the ionic polymer sensor/charge amplifier combination used in this work, the laser vibrometer is capable of providing an accurate low-frequency position measurement, a necessity for integral control. See Figure 5.10 for a comparison of the laser vibrometer displacement measurement and the charge amplifier output when a voltage step is applied to the polymer

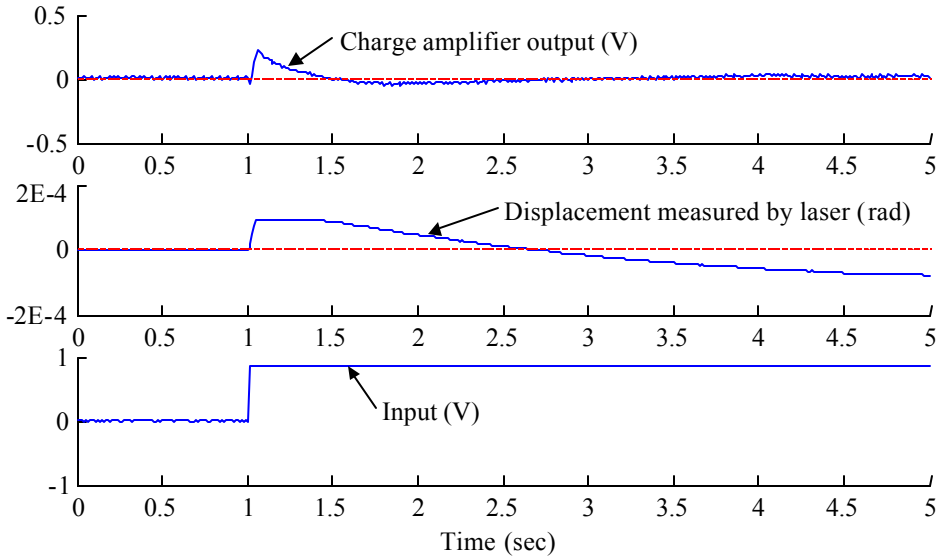

Figure 5.10: Step response of polymer motor, as measured by the laser vibrometer and by the polymer sensor and charge amplifier.

motor. Second, their experiments were performed in air. The author has observed that the nonminimum phase nature of ionic polymer transducer response appears more consistently and is often greatly exaggerated relative to the 'in air' response when the actuators are submerged in water. Because the compensator designs are based on a minimum phase model, this type of behavior will lead to instability if low-frequency signals are applied to the actuator. The motor's nonminimum phase behavior is apparent in the plot of motor displacement, as measured by the laser vibrometer, in Figure 5.10. Unlike the experiments conducted in air, the magnitude of the steady-state displacement is as approximately the same as the peak displacement, but in the opposite direction.

The most basic type of closed-loop control consists of simply using a gain for the

compensator. This option will not yield a significant improvement in tracking because a high open-loop gain cannot be achieved without the system becoming unstable. The instability occurs because the loci of closed-loop poles that originate from the pair of complex-conjugate poles corresponding the natural frequency of the motor head towards and cross the imaginary axis as the gain is increased. Also, as these closed-loop poles head towards the imaginary axis, their damping ratio decreases, resulting in a closed-loop frequency response with a large peak at the frequency of these poles. It is logical to consider a lead compensator in order to add damping to these poles; however, for a given gain crossover frequency, lead compensation will result in a lower open-loop gain below the gain crossover frequency. This decrease in open-loop gain will degrade the system's tracking performance – it will be even worse than system performance with a simple gain compensator. Another reason lead compensation is not used is that it would increase the system's sensitivity to sensor noise (because of the increase in the high frequency open-loop gain). Inspection of the plot of the charge amplifier output shown in Figure 5.7 reveals that a significant amount sensor noise is present.

A compensator that will produce the required increase in open-loop gain, though in a narrow frequency range only, consists of a pair of lightly damped complex-conjugate poles. One issue, however, is that this compensator will have a phase lag of 90 degrees at the peak in the compensator gain. This phase lag can be canceled by adding a zero at $s = 0$, giving the compensator the form

$$C(s) = K\frac{s}{s^2 + 2\zeta\omega_n s + \omega_n^2}, \tag{5.9}$$

where the gain K is a real number, and ω_n and ζ are the natural frequency and damping of the poles. This compensator will amplify signals with frequencies near the natural frequency of the poles, and it will attenuate any signals with frequencies outside this range. The compensator will introduce a total of 90 degrees of phase lag, with 0 degrees of lag at ω_n. The rate at which the phase changes in the region near the poles, as well as the magnitude and width of the magnitude peak will be determined by ζ. With lower values of ζ (lighter damping), the phase decrease will be more rapid, decreasing the system's stability margins. Also, the range of frequencies that will be amplified becomes smaller as ζ is decreased. The benefit of a lower ζ value is that the increase in the magnitude of the open-loop response is greater (at ω_n), which will lead to better tracking at or near ω_n. Figure 5.11a contains

a plot of the frequency response of the equation (5.9) compensator with ω_n=25.1 rad/sec (4Hz), ζ=0.05, and K=100. A comparison of the open-loop frequency response of the

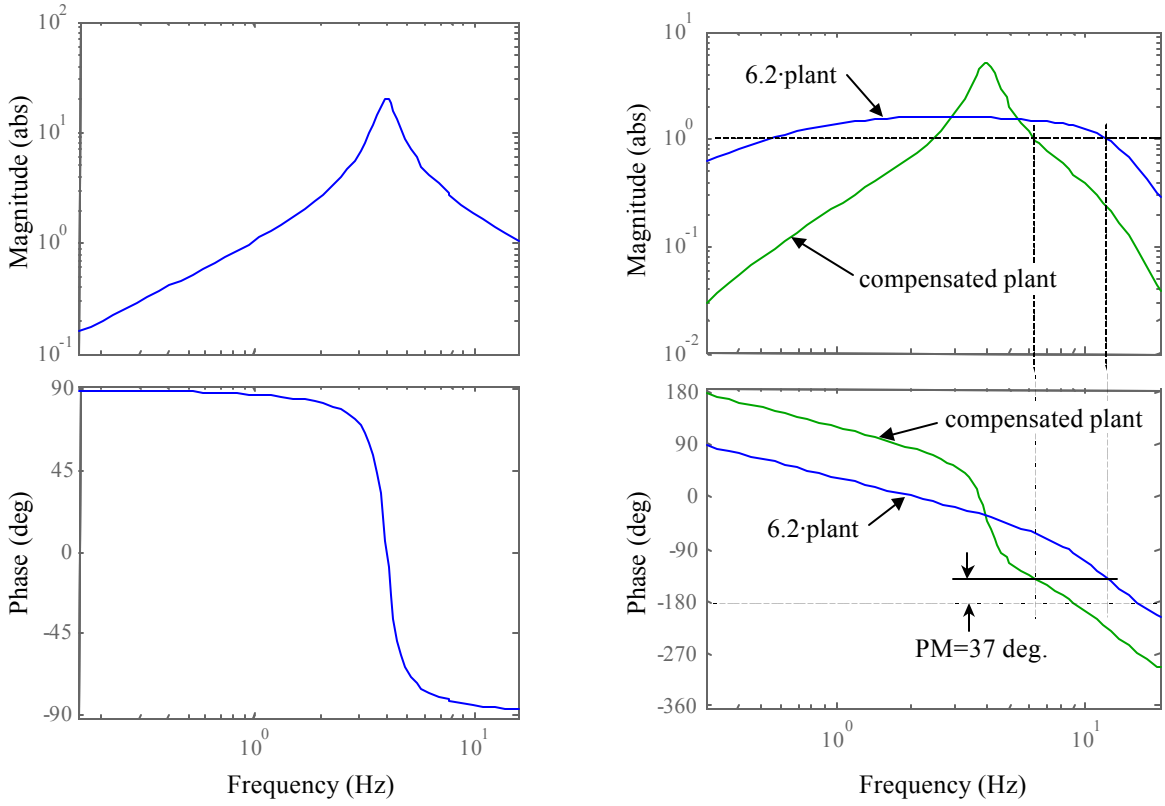

a. b.

Figure 5.11: Frequency response: a) Equation (5.9) compensator, b) Open-loop response of compensated system

compensated plant (based on the Figure 5.11a compensator) and 6.2 times the 'plant only' frequency response is shown in Figure 5.11b. Note that both open-loop responses have similar phase and gain margins: PM=37 deg, and GM=2 with Figure 5.11a compensator, PM=37 deg. and GM=1.7 with gain only.

5.3.2 Experimental Results

The compensator was implemented using a dSPACE 1102 DSP with a sampling rate of 1kHz, and the control signal was amplified using an HP power amplifier. The dSPACE was programmed using Simulink in conjunction with the Real Time Workshop. To prevent the

compensator from applying excessive voltages across the actuator electrodes, a saturation block was placed upstream of the DSP output in the Simulink block diagram, limiting the control voltage to +/-2V. The compensator was transformed to the z-domain using Tustin's method (Franklin et al., 1998).

Figure 5.12 shows a comparison of the open-loop response, based on an input level of 0.28V, with the closed-loop response for 3Hz, 4Hz, and 5Hz 0.1V sinusoidal reference signals. Plots 5.12a-c show experimental data, and plots 5.12d-f represent the responses predicted using the model. The control effort for the experimental closed-loop system is also plotted. The closed-loop system did track the sinusoidal reference signal well at 4Hz ($\frac{\omega_n}{2\pi}$ of the compensator), and, as expected, the closed-loop system's ability to track the reference signal quickly degrades as the reference frequency is shifted away from ω_n. Above ω_n, the closed-loop response magnitude was larger and exhibited a small amount of phase lag relative to the reference signal. Below ω_n, the closed-loop response magnitude was smaller than the reference signal and led it slightly. These trends are evident in both the simulated and the experimental data. Note that the simulated and experimental open-loop responses differ somewhat. The experimental open-loop response is a little noisy, has a smaller magnitude than the simulated response, and is not purely sinusoidal. The magnitude difference suggests that the plant dynamics changed slightly between the experiments used for model reconciliation and the control experiments, which were performed approximately three months apart. The motor was completely disassembled and reassembled between these two sets of experiments, so a slight change in plant performance is plausible. Also, the model is being used at a slightly lower operating point than the point about which the linear model was reconciled. According to the experimental data plotted in Figure 5.5, this shift in operating points will result in a smaller experimental response relative to to the predicted response. The fact that the open-loop response is not a pure sinusoid is a result of the Coulomb friction in the motor assembly and possibly some backlash between the polymer transducers and the rotor. With the 4Hz reference signal, the compensator was able to counteract the effects of the nonlinearities somewhat, resulting in a closed-loop response that was much closer to a pure sinusoid than the open-loop response. At this frequency, the only remaining evidence of the open-loop system nonlinearities is the presence of small 'flat spots' at the peaks of the closed-loop response.

Compensators with ζ=0.025 and ζ=0.1 and values of K that resulted in phase mar-

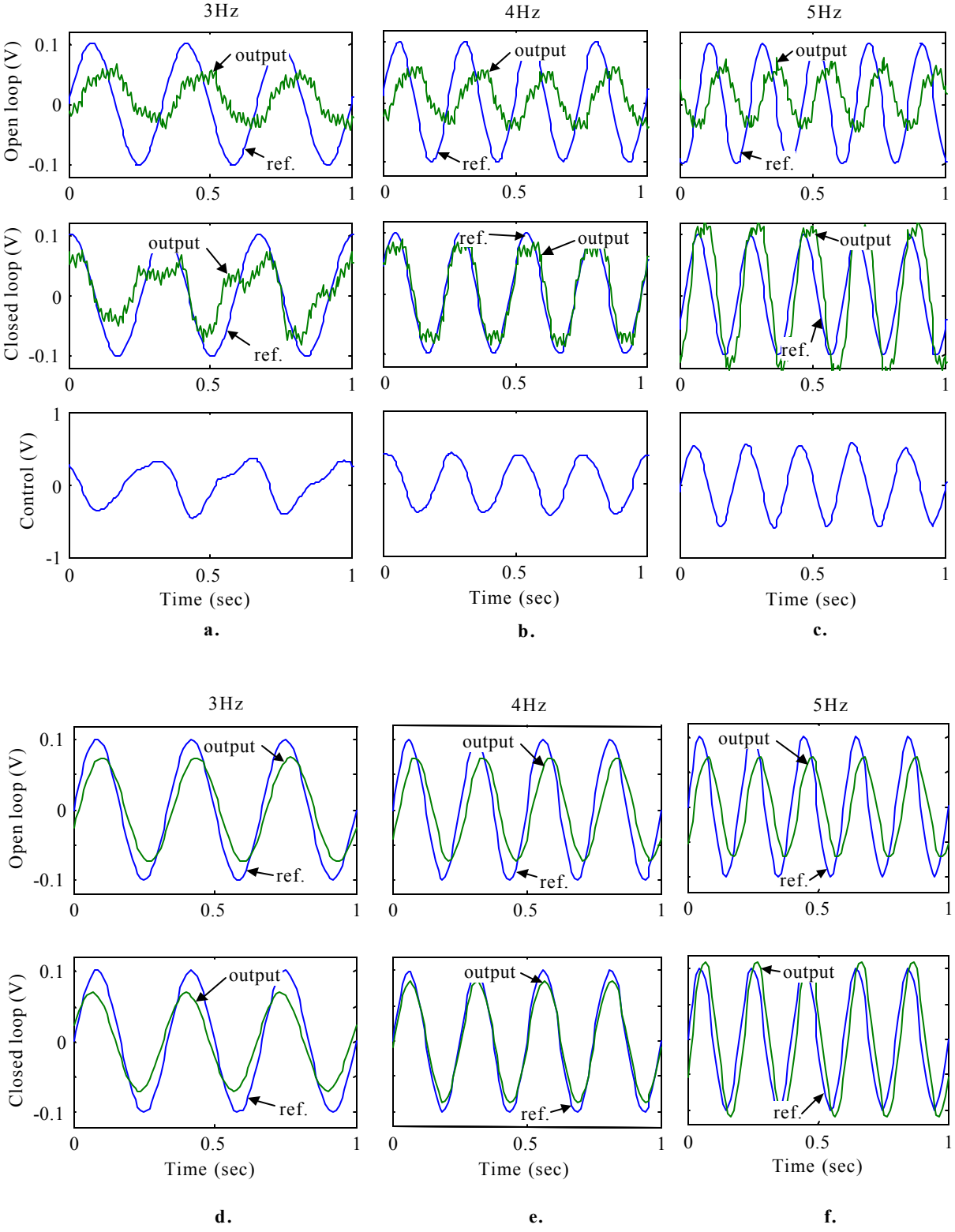

Figure 5.12: System response with 0.1V reference signal: a, b, c) 3Hz, 4Hz, 5Hz experimental open and closed-loop response, d, e, f) 3Hz, 4Hz, 5Hz simulated open and closed-loop response

gins of approximately 25 deg. were also implemented. The closed-loop system based on ζ=0.1 did not track significantly better than the open-loop system as the compensator did not provide adequate open-loop gain at ω_n. The closed-loop system based on ζ=0.025 followed the 4Hz 0.1V reference signal very well; however, tracking was very poor for 3Hz and 5Hz signals because of the narrow peak of the compensator gain at ω_n. These observations are consistent with the expected results based on the changes in the compensator response as ζ is varied.

Another benefit of the high frequency roll-off of the equation (5.9) compensator, which was illustrated in these experiments, is that the noise in the charge amplifier output does not affect the control signal. The noise, which will appear in the error signal on which the compensator operates, is filtered out by the compensator. Note, it is likely that the sensor noise level could be reduced a little by choosing a smaller feedback capacitance in the charge amplifier circuit, which would increase its gain. To maintain the same corner frequency, the feedback resistance would have to be increased by the same factor by which the capacitance was reduced, limiting the extent to which the amplifier gain can be boosted. Sensor noise reduction via changes in the charge amp circuit parameters was not explored experimentally. Another modification that would probably increase the signal to noise ratio for the sensor is to shorten the distance between the clamped end of the sensor polymer and the rim of the motor rotor. Earlier in this work, it was demonstrated that the sensor output is inversely proportional to this distance, so the sensor output would be increased for a given motor displacement. A wider sensor would also have produced a stronger signal.

5.4 Conclusions

The control experiments described in this chapter represent the first documented demonstration that an ionic polymer sensor can be used in a feedback-control system. In addition, this work shows that the model presented in Chapter 2, a linear time-invariant model, can be effectively used to design a closed-loop system involving ionic polymer transducers. The model was used to predict the open-loop response of a polymer motor, a mechanical device driven by multiple ionic polymer actuators. The same model was employed to predict the response of the ionic polymer sensor used to detect the motor's displacement. Also, the model's scalability was utilized, since the transducer dimensions were different than those of

the transducer used in the identification of the model parameters (performed in Chapter 3).

Due to the poor low-frequency response of the polymer sensor/charge amplifier combination and the inconsistent behavior of the polymer transducers at low frequencies, no attempts were made to the control sub-1Hz response of the polymer motor. The performance of the closed-loop system was limited by the significant phase lag in the motor-sensor-charge amp combination below the natural frequency of the motor. With these limitations, a compensator designed to track only a narrow frequency range of inputs was required to obtain good closed-loop tracking of single frequency inputs, the objective of the control experiments. The utility of the ionic polymer sensor/charge amplifier combination in a feedback control system would be better demonstrated if used to sense the displacement of a system that was more amicable to closed-loop control (exhibited less phase lag below the corner frequency).

Chapter 6

Conclusions and Future Work

6.1 Conclusions

The modeling effort in this work has demonstrated that ionic polymer transducers, in the cantilevered bender configuration, *can be accurately modeled using a pair of linear, symmetrically coupled equations with frequency-dependent parameters.* With the exception of the electromechanical coupling term, these parameters can be derived from well-understood physics and measurable, macroscopic, material properties. Because of the complex nature of the mechanisms responsible for the electromechanical coupling, the coupling term is identified experimentally; however, it is hoped that it will eventually be conclusively and quantitatively explained by a mathematical description of the coupling mechanisms. The fact that the transducer equations are coupled allows the same equations and parameters to be used for both sensing and actuation. A result of the symmetry in the transducer equations is that reciprocity exists between certain pairs of actuation and sensing relationships, for example, blocked force with a voltage input and short-circuit charge with a displacement input. This reciprocity was both predicted by the model and verified experimentally. The simplicity of the model allows it to be used as an engineering design tool.

In the process of experimentally identifying model parameters and validating the model, it was observed that ionic polymer transducers appear to behave more consistently above approximately 0.1Hz. At lower frequencies, their behavior sometimes varies when experiments are repeated, even when the same transducer is used. Also, at very low frequencies, they appear to perform differently when operated in water as opposed to when operated in air. This observation is based on a comparison of step responses observed dur-

ing the parameter identification process and step responses measured during the control experiments, as well as reports made by other researchers. These inconsistencies, along with the fact that the response is relatively small at low frequencies, will discourange the use of ionic polymer transducers in quasi-static applications. Another quasi-static issue is the permanent strain phenomenon which occurred with certain inputs. If this phenomenon can be understood and controlled, it may provide a means through which ionic polymer actuators can be used as DC actuators. Otherwise, it will be another issue that will dissuade designers from considering ionic polymer actuators for quasi-static applications.

A comparison of ionic polymer, piezoceramic, and PVDF cantilevered benders revealed that, above approximately 0.1Hz, their volumetric and gravimetric energy densities are within an order of magnitude of one another, with the ionic polymer having the lowest energy densities. Several factors should be taken into account when considering this comparison. For example, the cantilevered bender configuration does not make efficient use of the coupling in piezoelectric materials, so the corresponding energy density should not be interpreted as a general description of piezoelectric transducer capability – it applies to the cantilevered bender configuration only. Also, ionic polymer transducers are currently made from a base material that has been designed for other purposes. It is likely that once the electromechanical coupling mechanisms are understood, a base polymer with characteristics better suited for transducers can be designed. In addition, the choice of neutralizing ion, choice of solvent, and the electrode structure have been shown to affect ionic polymer transducer coupling. Advancements in these areas will result in ionic polymer transducers that compare more favorably to piezoelectric transducers, a mature and well-understood technology. However, unless order of magnitude improvements in ionic polymer actuator performance are made, ionic polymers will most likely be chosen for applications based only on the combination of characteristics that make them unique, such as operation at low voltages and biocompatibility – they will remain a niche technology. Another barrier that must be overcome is the frequency dependence exhibited by ionic polymer actuators.

When used as sensors, ionic polymer transducers compare more favorably to competing technologies, such as piezoelectric transducers. In the case where short-circuit charge is the measured output and force is the input, the sensitivity of an ionic polymer bender exceeds that of PVDF by over three orders of magnitude. When used to measure displacement, their sensitivity is still over an order of magnitude greater than a PVDF sensor with

the same geometry. If open-circuit voltage is used as the sensor output, ionic polymer transducer sensitivity is several orders of magnitude lower than piezoelectric sensors. This reduced sensitivity results from the relatively high capacitance, approximately eight orders of magnitude greater than PVDF. The charge generated by the electromechanical coupling is 'absorbed' by the large capacitance with little change in open-circuit voltage. When short-circuit charge (or current) is measured, the electrical impedance of the transducer becomes unimportant. Because of their relatively high sensitivity when using short-circuit charge as the output, ionic polymer sensors have the potential to replace PVDF sensors in some applications. This potential will be greatly improved if the frequency dependence of ionic polymer sensor performance can be reduced.

6.2 Recommended Future Work

The research reported in this document represents significant advancements in the areas of modeling and characterization of ionic polymer transducers. However, several matters within these areas deserve further investigation. Some examples are listed below.

Modeling and Parameter Identification

- The model presented in this work was shown to work for transducers with low voltages (approximately 0 to 1.25V) and small deflections (a few mm for a 15mm long bender); however, the limits of the linear model were not explored explicitly. A useful set of experiments would be to investigate the operating range of the linear model for both sensing and actuation. Identification of the regions in which the linear model can accurately predict ionic polymer transducer behavior is not only important to the model user, but it may also assist efforts focused on identifying the mechanisms responsible for the electromechanical coupling. In addition, it would be interesting to explore the operating regions in which the reciprocal sensing and actuation relations hold, for example blocked force over voltage and short-circuit charge over displacement.

- The current modeling approach was shown to work for cantilevered bender transducers. To further test the approach, it could be applied to other geometries that involve bending of the transducer in multiple planes, for example, a plate transducer.

- The match between the predicted and measured electrical impedances did not scale with changes in transducer geometry as well as other input/output quantities. This discrepancy suggests that the equivalent circuit used to model the ionic polymer's electrical impedance is too simple.

- The frequency range of the model was limited to approximately 20Hz by the experiment used to identify the ionic polymer modulus. The frequency range of the model could be extended by using specialized Dynamic Mechanical Analysis equipment, which is better suited to such measurements. The use of such equipment would also facilitate identification of the GHM parameters, which are used to represent the viscoelasticity of the polymer.

- The sample transducers available to the author were made from the same base material, Nafion 117, and were, therefore, all the same thickness. This fact prevented experimental verification of the variations in predicted transducer performance as thickness is changed. Such experiments would further validate the model and should be considered.

Characterization and Control

- The presented input-output expressions allow ionic polymer transducer performance to be reduced to a combination of a few material parameters and the transducers dimensions. A logical follow-up to this work would be to investigate the effects of factors such as ion choice, hydration level, plating process variations, solvent choice, etc. on the material parameters, especially the electromechanical coupling. Such investigations would hopefully lead to increases in the coupling term. Also, it is hoped that the frequency dependence in the input-output relationships can be reduced through tailoring of the material parameters.

- The output signal of the op-amp circuit used to measure the short-circuit current during sensor experiments exhibited phase lag that was attributed to an unmodeled interaction between the polymer transducer and the circuit. To obtain a high quality short-circuit current measurement, more sophisticated circuits should be considered. In the least, a more detailed model of the op-amp in the circuit used in this work

should be analyzed in order to allow correction for the spurious phase lag during post processing.

- Two researchers have demonstrated that ionic polymer sensors can be used in the dry condition, but reports in the literature indicate that the transducers must be fully hydrated in order to function as actuators. If these observations are correct, they preclude the existence, in dry ionic polymer transducers, of the reciprocity exhibited by the hydrated transducers used in this work. Experiments should be performed on the same transducers, in conditions ranging from fully hydrated to dry, in order to determine whether or not the manner in which the coupling was modeled in this work can be applied to transducers that are not fully hydrated.

- Comparisons to piezoelectric bender actuators have indicated that ionic polymer actuators do not have any clear performance benefits in terms of general metrics such as volumetric and gravimetric energy density. However, the base materials used for ionic polymer transducers were designed for other purposes and can most likely be modified such that they are be better suited for use as a transducer base material. Improvements in performance will increase the chances of ionic polymer actuators finding their way in to practical applications. Therefore, research of this nature should be performed before interest in ionic polymer actuators wanes. The model presented in this work provides a convenient means by which to quantify any improvements made in the electromechanical coupling.

- The attempted combined sensor actuator configurations reported in this work were unsuccessful; however, the exploration of this topic was by no means exhaustive. Further research in this area is recommended.

Bibliography

Bar-Cohen, Y. and Leary, S., 2000, *Electroactive Polymer (EAP) Characterization Methods*, in: **Proceedings of the SPIE**, Vol. 3987, pp. 12–16.

Bar-Cohen, Y., Sherrit, S., and Lih, S., 2001a, *Characterization of the Electromechanical Properties of EAP materials*, in: **Proceedings of the SPIE**, Vol. 4329, pp. 319–327.

Bar-Cohen, Y., Spinks, G., and Zhang, Q., 2001b, "Electroactive Polymers (EAP) Actuators and Devices, SPIE short course notes," .

Bennett, M., 2002, **Manufacture and Characterization of Ionic Polymer Transducers Employing Non-Precious Metal Electrodes**, M.S. Thesis, Virginia Tech.

Beranek, L. L., **Acoustics**, McGraw-Hill Book Company, New York, 1954.

DeGennes, P., Okumura, K., Shahinpoor, M., and Kim, K., *Mechanoelectric effects in ionic gels*, **EUROPHYSICS LETTERS**, Vol. 40, No. 4, pp. 513–518, 2000.

Dorf, R., **Modern Control Systems**, Addison-Wesley, 1989.

Ferrara, L., Shahinpoor, M., Kim, K., Schreyer, B., Keshavarzi, A., Benzel, E., and Lantz, J., 1999, *Use of ionic polymer-metal composites (IPMCs) as a pressure transducer in the human spine*, in: **Proceedings of the SPIE**, Vol. 3669, pp. 394–401.

Franklin, G., Powell, J., and Emami-Naeini, A., **Feedback Control Systems**, Addison-Wesley, 1994.

Franklin, G., Powell, J., and Workman, M., **Digital Control of Dynamic Systems**, Addison-Wesley, 1998.

Germano, C., 1972, **Technical Pulication TP-223 Ceramic Bender Bimorphs**, Morgan Matroc Electro Ceramics, Bedford, OH.

Grodzinsky, A. and Melcher, J., 1974, *Electromechanics of Deformable Charged Polyelectrolyte Membranes*, in: **Proceedings of the 27th Annual Conference of Engineering in Medicine and Biology**, Vol. 16, p. 485.

Grodzinsky, A. and Melcher, J., *Eelctromechanical Transduction with Charged Polyelectrolyte Membranes*, **IEEE Transactions on Biomedical Engineering**, Vol. 23, No. 6, pp. 421–433, 1976.

Guo, S., Fukuda, T., Oguro, K., Nakamura, T., and Aria, F., 1996, *Micro Active Guide Catheter System Characteristic Evaluation, Electrical Model and Operability Evaluation of Micro Active Catheter*, in: **Proceedings of the IEEE Internation Conference on Robotics and Automation**, pp. 2226–2231.

Halliday, D. and Resnick, R., **Physics, Parts 1 and 2**, John Wiley and Sons, 1978.

Henderson, B., Lane, S., Shahinpoor, M., Kim, K., and Leo, D., 2001, *Evaluation of Ionic Polymer-Metal Composites for Use as Near-DC Mechanical Sensors*, in: **AIAA Space 2001 - Conference and Exposition, Albuquerque, NM, AIAA paper 2001-4600**.

Ikeda, T., **Fundamental of Piezoelectricity**, Oxford Press, New York, 1996.

Inman, D. J., **Engineering Vibration**, Prentice-Hall, Englewood Cliffs, 1994.

Kanno, R., Kurata, A., Hattori, M., Tadokoro, S., Takamori, T., and Oguro, K., 1994, *Characteristics and Modeling of ICPF Actuator*, in: **Proceedings of the Japan-USA Symposium on Flexible Automation**, Vol. 2, pp. 691–698.

Kanno, R., Tadokoro, S., Takamori, T., and Hattori, M., 1996, *Linear Approximate Dynamic Model of ICPF Actuator*, in: **Proceedings of the IEEE International Conference on Robotics and Automation**, pp. 219–225.

Keshavarzi, A., Shahinpoor, M., Kim, K., and Lantz, J., 1999, *Blood pressure, pulse rate, and rythm measurement using ionic polymer-metal composite sensors*, in: **Proceedings of the SPIE**, Vol. 3669, pp. 369–376.

Konyo, M., Tadokoro, S., Takamori, T., and Oguro, K., 2001, *EAP application to artificial tactile feel display of virtual reality*, in: **Proceedings of the SPIE**, Vol. 4329, pp. 389–400.

Kothera, C. and Leo, D., 2002, *Bandwidth Characterization of Ionic Polymer-Metal Composite Actuators*, in: **To appear in Proceedings of The First World Congress on Biomimetics and Artificial Muscles**.

Mallavarapu, K., 2001, **Feedback Control of Ionic Polymer Actuators**, M.S. Thesis, Virginia Tech.

Mallavarapu, K., Newbury, K., and Leo, D., 2001, *Feedback Control of the Bending Response of Ionic Polymer-Metal Composite Actuators*, in: **Proceedings of the SPIE**, Vol. 4329, pp. 301–310.

McTavish, D. and Hughes, P., *Modeling of Linear Viscoelastic Space Structures*, **Journal of Vibration and Acoustics**, Vol. 115, pp. 102–110, 1993.

Measurement Specialties, I., 1999, **Piezo Film Sensor, Technical Manual**.

Mojarrad, M. and Shahinpoor, M., 1997a, *Ion-exchange-metal composite artificial muscle actuator load characterization and modeling*, in: **Proceedings of the SPIE**, Vol. 3040, pp. 294–301.

Mojarrad, M. and Shahinpoor, M., 1997b, *Ion-Exchange-Metal composite sensor films*, in: **Proceedings of the SPIE**, Vol. 3042, pp. 52–60.

Nemat-Nasser, S., *Micro-mechanics of Actuation of Ionic Polymer-metal Composites (IPMCs)*, **to appear in Journal of Applied Physics**, 2002.

Nemat-Nasser, S. and Li, J., *Electromechanical Response of Ionic Polymer-Metal Composites*, **Journal of Applied Physics**, Vol. 87, pp. 3321–3331, 2000.

Newbury, K. and Leo, D., *Electromechanical Modeling and Characterization of Ionic Polymer Benders*, **to appear in Journal of Intelligent Material Systems and Structures**, 2002.

Nilsson, J., **Electric Circuits**, Addison-Wesley, 1983.

Oguro, K., Kawagami, Y., and Takenaka, H., *Bending of an Ion-Conducting Polymer Film-Electrode Composite by an Electric Stimulus at Low Voltage*, **Journal of Micromachine Society**, Vol. 5, pp. 27–30, 1992.

Piezo Systems, I., 1998, **Interim Catalog 2C**.

Sadeghipour, K., Salomon, R., and Neogi, S., *Development of a novel electrochemically active membrane and 'smart' material based vibration sensor/damper*, **Smart Materials and Structures**, Vol. 1, pp. 172–179, 1992.

Segalman, D., Witkowski, W., Adolf, D., and Shahinpoor, M., *Theory of Electrically Controlled Polymeric Muscles as Active Materials in Adpative Structures*, **Smart Materials and Structures**, Vol. 1, pp. 44–54, 1992.

Shahinpoor, M., *Micro-Electro-Mechanics of Ionic Polymeric Gels as Electrically Controllable Artificial Muscles*, **Journal of Intelligent Material Systems and Structures**, Vol. 6, No. 3, pp. 307–314, 1995.

Shahinpoor, M., 1999, *Electro-mechanics of iono-elastic beams as electrically-controllable artificial muscles*, in: **Proceedings of the SPIE**, Vol. 3669, pp. 109–121.

Shahinpoor, M., Bar-Cohen, Y., Simpson, J., and Smith, J., *Ionic Polymer-Metal Composites (IPMCs) as Biomimetic Sensors, Actuators and Artificial Muscles - a Review*, **Smart Materials and Structures**, Vol. 7, No. 6, pp. R15–R30, 1998.

Shahinpoor, M. and Kim, K., 2001, *Design, Development and Testing of a Multi-Fingered Heart Compression/Assist Device Equipped with IPMC Artificial Muscles*, in: **Proceedings of the SPIE**, Vol. 4329, pp. 411–420.

Shahinpoor, M. and Kim, K. J., 2000, *Effect of Counter-ions on the Performance of IPMCs*, in: **Proceedings of the SPIE**, Vol. 3987, pp. 110–120.

Shahinpoor, M., Mojarrad, M., and Salehpoor, K., 1997, *Electrically induced large amplitide vibration and resonance characteristics of ionic polymeric membrane-metal composites artificial muscles*, in: **Proceedings of the SPIE**, Vol. 3041, pp. 829–838.

Shigley, J. and Mischke, C., **Mechanical Engineering Design**, McGraw-Hill, 1989.

Tadokoro, S., Takamori, T., and Oguro, K., 2001, *Application of the Nafion-Platinum Composite Actuator*, in: **Proceedings of the SPIE**, Vol. 4329, pp. 28–42.

Tadokoro, S., Yamagami, S., Takamori, T., and Oguro, K., 2000, *Modeling of Nafion-Pt Composite Actuators (ICPF) by Ionic Motion*, in: **Proceedings of the SPIE**, Vol. 3987, pp. 92–102.

Tiersten, H., **Linear Piezoelectric Plate Vibrations**, Plenum Press, 1969.

Wang, Q., Du, X., Xu, B., and Cross, L., *Eelctromechanical Coupling and Output Efficiency of Piezoelectric Bender Actuators*, **IEEE Transactions on Ultrasonics, Ferroelectrics, and Frequency Control**, Vol. 46, No. 3, pp. 638–646, 1999.

Ward, I. and Hadley, D., **An Introduction to the Mechanical Properties of Solid Polymers**, John Wiley and Sons, 1993.

Xiao, Y. and Bhattacharya, K., 2001, *Modeling electromechanical properties of ionic polymers*, in: **Proceedings of the SPIE**, Vol. 4329, pp. 292–300.

Appendix A

Circuits used for experiments

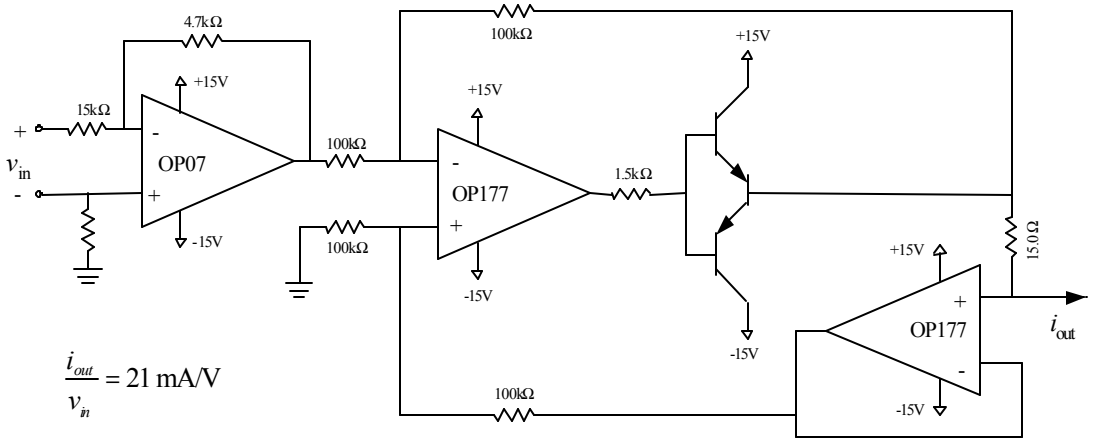

Figure A.1: Transconductance amplifier (voltage to current)

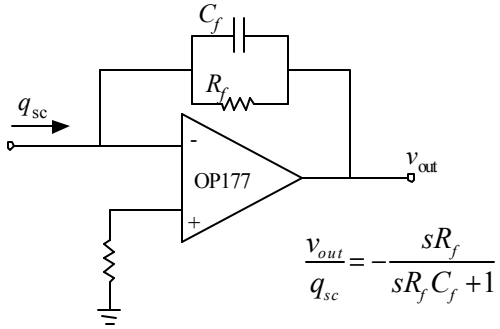

Figure A.2: Charge amplifier circuit (sensing)

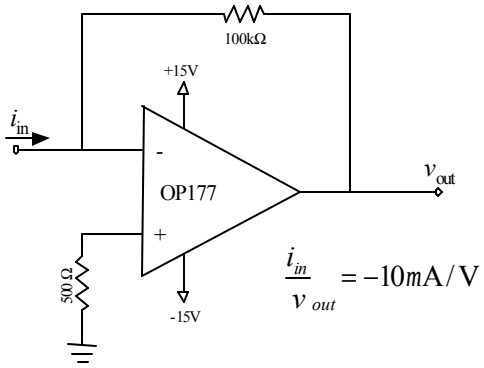

Figure A.3: Short-circuit current measurement circuit (sensing)

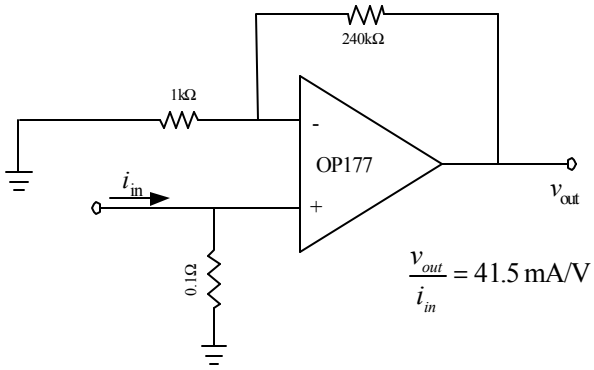

Figure A.4: Current measurement circuit (actuation)

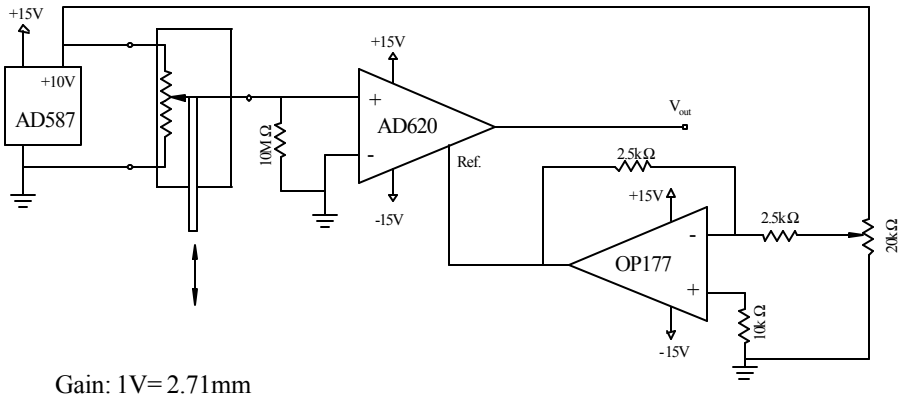

Figure A.5: Power supply and signal conditioining circuit for linear potentiometer

Vita

Kenneth Newbury was born in Painsville, OH on September 10, 1968 to William and Mary Newbury. In 1986, he graduated from Mentor High School in Mentor, OH, and in the following September, he started attending classes as a pre-med student at the University of Toledo. Kenneth graduated from the University of Toledo College of Engineering in 1991 with Bachelor of Science degrees in Mechanical and Electrical Engineering and began a career in industry as a mechanical engineer. In August of 1997, he returned to The University of Toledo to pursue Master of Science and Doctoral degrees in Mechanical Engineering. He moved to Virginia in January, 1999 to attend Virginia Tech as a graduate research assistant under Dr. D. Leo, who had been his advisor at The University of Toledo. Kenneth received his Master of Science Degree in Mechanical Engineering from The University of Toledo in August of 1999; his thesis topic involved vibration of stiffened plates with piezoceramic transducers. Several months after completing his MS degree requirements, the focus of his studies shifted to ionic polymer transducers, the topic of this dissertation.

Kenneth is currently employed as a Senior Project Engineer in the Moog, Inc. Aircraft Group in East Aurora, NY.

This dissertation was typeset with LaTeX 2_ε[1] by the author.

[1] LaTeX 2_ε is an extension of LaTeX. LaTeX is a collection of macros for TeX. TeX is a trademark of the American Mathematical Society. The macros used in formatting this dissertation were written by Greg Walker, Department of Mechanical Engineering, Virginia Tech.